



저작자표시 2.0 대한민국

이용자는 아래의 조건을 따르는 경우에 한하여 자유롭게

- 이 저작물을 복제, 배포, 전송, 전시, 공연 및 방송할 수 있습니다.
- 이차적 저작물을 작성할 수 있습니다.
- 이 저작물을 영리 목적으로 이용할 수 있습니다.

다음과 같은 조건을 따라야 합니다:



저작자표시. 귀하는 원저작자를 표시하여야 합니다.

- 귀하는, 이 저작물의 재이용이나 배포의 경우, 이 저작물에 적용된 이용허락조건을 명확하게 나타내어야 합니다.
- 저작권자로부터 별도의 허가를 받으면 이러한 조건들은 적용되지 않습니다.

저작권법에 따른 이용자의 권리는 위의 내용에 의하여 영향을 받지 않습니다.

이것은 [이용허락규약\(Legal Code\)](#)을 이해하기 쉽게 요약한 것입니다.

[Disclaimer](#) 

Ph.D. DISSERTATION

**Development of Fibriform Organic
Electrochemical Devices Based on
Stranded Assembly of Microfibers for
Smart Electronic Applications**

By

Soo Jin Kim

August 2021

DEPARTMENT OF MATERIALS SCIENCE AND ENGINEERING

COLLEGE OF ENGINEERING

SEOUL NATIONAL UNIVERSITY

Development of Fibriform Organic Electrochemical Devices Based on Stranded Assembly of Microfibers for Smart Electronic Applications

Advisor: Prof. Ho Won Jang

by

Soo Jin Kim

A thesis submitted to the Graduate Faculty of Seoul National University
in partial fulfillment of the requirements
for the Degree of Doctor of Philosophy
Department of Materials Science and Engineering

August 2021

Approved

by

Chairman of Advisory Committee: Jeong-Yun Sun

Vice-Advisory Committee: Ho Won Jang

Advisory Committee: Min Sang Kwon

Advisory Committee: Jung Ah Lim

Advisory Committee: Hyunsu Ju

Abstract

As the promising platform for wearable device, electronic textile (E-textile) have attracted considerable attention in order to achieve portability, washability and deformability and breathable properties. In the meantime, fiber-shaped electronics (fibertronics) have advanced with advantage of textile, flexibility, light weight, miniaturization and their capability of easy integration into diverse devices. The one dimensional cylindrical-fiber geometry also provides large active surface and 2D or 3D structures by fiber assemblies. Over the last decade, development in various fiber-shaped devices such as transistor, actuators, energy storage, light-emitting device and sensors has been reported. In particular, transistor is a key component for realizing integration of electronic systems in displays, sensors, memory and neuromorphic devices. However, the improvement in electrical performance of fiber-shaped transistors for practical usage is difficult due to its structure composed of multilayers and well-aligned semiconductor between source and drain on cylindrical fiber. Also the length-to-width ratio which is proportional factor for output current is limited by geometry of vacuum-deposited electrodes on a half-side of the fiber electrode.

In the thesis, a new structure of fiber-shaped organic thin film transistor with a double-stranded assembly of electrode microfibers (DSA-fiber transistor) is proposed to overcome the limitation of the previous fiber-shaped transistors. And the studies of the redox reaction between conjugated polymer and ionic species under operating transistor and strategy to improve the durability of the DSA-fiber transistor are described in detail.

In the chapter 1, the basic of organic thin film transistor is introduced.

In the chapter 2, I have designed the DSA-fiber transistors to improve electrical performance of fiber-shaped transistor for practical application to e-textile. The basic feature of the DSA-fiber transistors is twisted assembly of semiconductor-coated electrode microfibers as source and drain electrodes (S/D) to form channel. The architecture of device makes it simple to control the channel dimension of DSA-fiber transistors by varying the length of the S/D microfibers and thickness of semiconductor layer as a channel width and length, respectively. The demonstrated DSA-fiber transistors showed high electrical performance with high output current over -5 mA under -1.5 V and on/off current ratio around 105. After 1000 bending cycles and washing in water mixed with a strong detergent, the performance of the device was preserved. Application of DSA-fiber transistor was demonstrated by switching and controlling current-driven LED devices and detecting signals of electrocardiogram from human body.

In the chapter 3, I proposed multi-synapses implementable organic neuromorphic transistor based on DSA-fiber transistor (organic-neurofiber) with enhanced cyclic endurance and its application to spatiotemporal iterative learning. The architecture of the organic-neurofibers is composed of multiple gates weaved on DSA-fiber transistor to implement multiple synaptic junctions imitating dendritic network of biological neuron fibers. Especially, the neurofiber based on functionalized polymer, which could induce deprotonation, exhibits reliable memory characteristics such as cyclic endurance and retention under gate-field compared to the device based on conventional polymer with irregular cyclability and poor long-term stability. It was found that the balanced charges in functionalized polymer channel under cycling test make reversible doping and dedoping of polymer channel, resulting in stable and reliable cyclic endurance of the device. The memory states, which regulate the synaptic weight, remained stable and was operated independently under each multiple gates by a gate-field on the device based on the functionalized polymer. Finally, the speech recognition as a simulation of spatiotemporal iterative learning was demonstrated with neurofiber, showing significant recognition accuracy of around 90 %.

In the chapter 4, I have suggested the fiber-shaped electrochemical metal-iongel-semiconductor Diode (fibrous-EMIS diode) for protection of e-textile by static electricity. The EMIS has the formation of redox layer so called rectifying junction

between iongel and semiconductor by applying voltage. The directional current response is based on redox reaction therefore the critical voltage of EMIS diode depends on low oxidative potential (<3 V) of organic semiconductor. This low threshold voltage of EMIS is enable to protect low-voltage operational e-textile. As a result, the circuit of DSA-fiber transistor and fibrous-EMIS diode weaved into textile shows enhanced durability under static electricity compared to without fibrous-EMIM diode.

Keyword: Fiber-Shaped Electronic Device, Organic Electrochemical Transistor, Electronic Textile, Neuromorphic Device, Polythiophene, Redox Mechanism

Student Number: 2017-38767

Soo Jin Kim

Table of Contents

Abstract	1
Table of Contents	5
List of Tables	7
Chapter 1 Basics of Ion-gel-Gated Organic Thin-Film Transistor	22
1.1 References.....	27
Chapter 2 Fiber-Shaped Ion-gel-Gated Organic Transistor Composed of Double-Stranded Assembly of Microfiber Electrodes for E-textile Application	28
2.1 Introduction	29
2.2 Experimental Method.....	34
2.3 Results and Discussion	38
2.4 Summary	61
2.4 References.....	62
Chapter 3 Fiber-Shaped Multi-Synapses Implementable Organic Electrochemical Transistor for Neuromorphic device.....	66
3.1 Introduction	67
3.2 Experimental Method.....	73

3.3 Results and Discussion	75
3.4 Summary	124
3.5 References	125
Chapter 4 Fibrous TVS Diode for Antistatic E-textile	129
4.1 Introduction	130
4.2 Experimental Method	133
4.3 Result and Discussion	135
4.4 Summary	149
4.5 References	150
Abstract (in Korean)	153

List of Tables

Table 1 Electrical characteristics of DSA-fiber TFTs based on P3HT nanostructure.

List of Figures

Figure 1. Schematics of thin-film transistor with bottom-gate, (a) bottom-contact and (b) top- contact and top-gate, (c) bottom-contact and (d) top-contact.

Figure 2. Schematics of an electrolyte-gated organic thin film transistor.

Figure 3. Scheme of the structures of thin-film TFT based on (a) planar substrate and (b) previous reported fiber-shaped TFT.

Figure 4. Schematic of fibrous thin-film transistor based on double-stranded assembly.

Figure 5. Scheme of die-coating system for coating P3HT layer on microfiber.

Figure 6. Scheme of process to twist microfibers covered with semiconductor layer and utilize iongel on twisted microfibers.

Figure 7. Scheme of holistic fabrication for DSA-fiber TFT.

Figure 8. (a) Controlled thickness of thin-film coated P3HT-NR on microfibers by changing the drawing speed. (b) SEM images of cross-sectional P3HT NR film covered on microfibers.

Figure 9. (a) Image of P3HT film coated on Au-microfiber captured by cross-sectional SEM and optical microscope. (b) Top SEM image for double-stranded assembly of microfibers with coated P3HT film.

Figure 10. Top-view SEM images for investigation of homogeneity in twist assembled P3HT-coated electrode microfibers with 3.8 cm-length. (a)-(d) The enlarged images with interval of 7.5 mm confirmed connection between two electrode microfibers along the 3.8-cm of twisted assembly.

Figure 11. Final fabricated DSA-fiber TFT captured by (a) photography and (b) Cross-sectional SEM.

Figure 12. UV-vis spectra of P3HT solution in various stirring time from 1 hour to 10 days.

Figure 13. AFM topography images for (a)(c) P3HT-NG and (b)(d) P3HT-NR films prepared with different concentration : (a)(b) 7 wt% and (c)(d)

0.0025 wt%. Insets in (c)(d) present height profiles of cross-sectional AFM extracted from the each colored dash lines.

Figure 14. AFM topography images for nanostructure of P3HT films prepared with a 0.0002 wt % in solvent mixture under different aging times from 0 min to 7 days.

Figure 15. Two-dimensional GIXD images of the (a) P3HT-NG and (b) P3HT-NR film

Figure 16. (a) Out-of-plane and (b) in-plane GIXD plot to compare the P3HT-NG and P3HT-NR films.

Figure 17. Schematics of preferred and expected charge transport paths with double-stranded assembly.

Figure 18. Hardness of P3HT, P3HT-NG and P3HT-NR analyzed by nano-indentation measurement.

Figure 19. Transfer and output characteristics of the DSA-fiber TFT based on P3HT-NR film.

Figure 20. Plot of drain current (I_{DS}) versus (a) channel length, which accords with thickness of semiconductor film coated on microfiber electrode (left) and (b) channel width, which is corresponds on length of DSA-fiber TFT (left). The transfer characteristics (V_{GS} - I_{DS}) of the device with various (a) channel length (right) and (b) channel width (right).

Figure 21. Photograph and transfer characteristics of the embedded DSA-fiber TFT in the textile.

Figure 22. (a) Variation of transconductance (left) and shift of threshold voltage (right) under each bending condition. (b) Variation of transconductance (left) and shift of threshold voltage (right) versus number of bending cycles (bending diameter : 7 mm).

Figure 23. Transfer curves of the device for comparison in various condition ; Before (Black) and after (Blue) washing in distilled water with passivation layer, after immersing in water without passivation layer (Green), after washing in detergent dissolved water with passivation layer (Red).

Figure 24. (a) Diagram for controlling luminescence of conventional LED by DSA-fiber TFT. (b) The luminescence efficiency of red LED versus output current controlled by embedded-DSA-fiber TFT in fabrics (c) Photography of LED connected with DSA-fiber TFT embedded in textile.

Figure 25. Plot of drain current (top) under output voltage (bottom) under applying 0.5V and -3V (left) and photograph of RGB-LED connected with textile-embedded DSA-fiber TFT for controlling on/off switching (right).

Figure 26. (a) Drain current of DSA-fiber TFT (blue and red line) occurred by potential change of ECG (black line). (b) Photograph of electrode contacts on skin for monitoring ECG signal. (c) Plot of drain current (black line) and potentiometric recoding (blue line) during measuring a single cardiac cycle of ECG with DSA-fiber TFT.

Figure 27. Schematic of biological synapse(inset), presynaptic neuron and postsynaptic neuron.

Figure 28. Schematic of the device structure for neurofiber-OECT and the doping interaction in channel by ions (inset) and photograph of OECT-neurofiber.

Figure 29. Schematics of fabrication of neurofiber-OECT.

Figure 30. Molecular structures of poly(3-hexylthiophene-2,5-diyl) (P3HT), poly[3-(6-carboxyhexyl)thiophene-2,5-diyl] (P3CT) and 1-ethyl-3-methylimidazolium bis(trifluoromethylsulfonyl)imide ([EMIM][TFSI]).

Figure 31. Comparison of postsynaptic current between the planer P3HT-OECTs and P3HT-neurofiber with a length (L) of 2 μm and a width (W) of 1cm when the gate-bias was applied ($V_{\text{GS}} = -0.7 \text{ V}$, 100 ms)

Figure 32. Schematics of channel dimension of a (a) planar device and (b) neurofiber-OECTs.

Figure 33. (a) Transfer graph of P3HT-neurofiber at $V_{\text{DS}} = -0.2 \text{ V}$. (b) Drain current as postsynaptic current (PSC) induced by various V_{GS} from -0.7 V to -1.5 V as a presynaptic stimulation in P3HT-neurofiber.

Figure 34. (a) Transfer curves at $V_{\text{DS}} = -0.2 \text{ V}$ and (b) 50 W-R-E-R cycles of planar P3HT-OECT using $V_{\text{GS}} = -1.5 \text{ V}$, 10 s duration for programmed pulse and $V_{\text{GS}} = 1.5 \text{ V}$, 5 s duration for the erased pulse. After applying each pulses, drain current (I_{DS}) was recorded at $V_{\text{GS}} = 2 \text{ mV}$ with 2 s intervals. (c)

Illustration of the planar OECT and optical microscope image of the channel dimension of the device.

Figure 35. (a) 50 W-R-E-R cycles of P3HT-neurofiber by using $V_{GS} = -1.5$ V with 10 s duration for the programming pulse (V_{PGM} and T_{PGM}) and $V_{GS} = 1.8$ V with 5 s duration for the erasing pulse (V_{ER} and T_{ER}). After applying pulses for programming or erasing, drain current was recorded under $V_{GS} = 2$ mV with 2 s intervals. (b) Retention characteristics of the P3HT-neurofiber.

Figure 36. Cyclic voltammetry curves of (a) P3CT and (b) P3HT in [EMIM][TFSI], as recorded with a scan rate of 50 mV/s. (c) Cyclic voltammogram to confirm the electrochemical window of [EMIM][TFSI].

Figure 37. (a) Transfer graph of P3CT-neurofiber at $V_{DS} = -0.2$ V. (b) Drain current as postsynaptic current induced by various V_{GS} from -0.7 V to -1.5 V as a presynaptic stimulation in P3CT-neurofiber.

Figure 38. (a) 50 W-R-E-R cycles of P3CT-neurofiber by using $V_{GS} = -1.5$ V with 10 s duration for the programming pulse (V_{PGM} and T_{PGM}) and $V_{GS} = 1.8$ V with 5 s duration for the erasing pulse (V_{ER} and T_{ER}). After applying

pulses for programming or erasing, drain current was recorded under $V_{GS} = 2$ mV with 2 s intervals. (b) Retention characteristics of the P3HT-neurofiber.

Figure 39. Retention characteristics of P3CT-neurofibers under (a) different programmed voltages with constant duration or (b) various number of pulses at the same programmed voltage. After applying each pulses, drain current was recorded at $V_{DS} = -0.2$ V and $V_{GS} = 0$ mV with 5 s intervals.

Figure 40. Cyclic voltammetry curves of P3HT in [EMIM][TFSI] ionic liquid at 50 mV/s.

Figure 41. Raman spectra of P3HT upon condition for oxidation and reduction during cyclic voltammetric cycles.

Figure 42. Changes in the FT-IR spectra of P3HT films and [EMIM][TFSI] ions under doping and dedoping process.

Figure 43. The structures of TFSI with (a) cisnoid and (b) transoid.

Figure 44. Illustration of the interaction between P3HT and [TFSI][EMIM] under electrochemical doping and dedoping process.

Figure 45. Cyclic voltammetry curves of P3CT in [EMIM][TFSI] ionic liquid at 50 mV/s.

Figure 46. Changes in the FT-IR spectra of P3CT films and [EMIM][TFSI] ions under redox process.

Figure 47. FT-IR spectra for analyzing to hydrogen bond in carboxylic acid of P3CT films after oxidation process.

Figure 48. The C1s peaks in the X-ray photoelectron spectroscopy (XPS) spectra of the pristine P3CT, doped P3CT, dedoped P3CT films and [TFSI][EMIM].

Figure 49. Raman spectra of P3CT films after doping and dedoping upon cyclic voltammetric cycles.

Figure 50. Illustration of the interaction between P3CT and [TFSI][EMIM] under electrochemical doping and dedoping process.

Figure 51. AFM topography images of pristine P3HT, doped P3HT and dedoped P3HT.

Figure 52. 2D grazing-incidence X-ray diffraction (GIXD) profiles of pristine, doped and dedoped P3HT films.

Figure 53. Out-of-plane and in-plane grazing incidence X-ray diffraction (GIXD) plots of P3HT upon electrochemical doping and dedoping process.

Figure 54. Schematics presenting the change of the polymer structure under doping/dedoping process by penetration of ions in P3HT.

Figure 55. AFM topography images for pristine P3CT, doped P3CT, and dedoped P3CT films.

Figure 56. Out-of-plane and in-plane grazing incidence X-ray diffraction (GIXD) plots of P3CT upon electrochemical doping and dedoping process.

Figure 57. 2D grazing-incidence X-ray diffraction (GIXD) profiles of pristine, doped and dedoped P3CT films.

Figure 58. Schematics presenting the change of the polymer structure under doping/dedoping process by penetration of ions in P3CT.

Figure 59. Raman spectra analyzed for (a) pristine P3CT (black line), doped P3CT (red line) and dedoped P3CT (green line) films. Compared to the backbone planarity of P3CT and dedoped P3CT, (b) the (C=C) peak shifted higher and (c) the (C-C) peak shifted lower after dedoping process.

Figure 60. Illustrated diagrams of single class neural network on the basis of Tempotron learning method and operation of neurofiber. (g_i : conductance of each channel)

Figure 61. Postsynaptic current (PSC) of a P3CT-neurofiber according to function of the time difference (Δt) between spikes ($V_{GS} = -0.7$ V, 100 ms) as a presynaptic stimulus.

Figure 62. Postsynaptic current (PSC) of a P3HT-neurofiber depending on function of the time difference (Δt) between spikes ($V_{GS} = -0.7$ V, 100 ms).

Figure 63. Postsynaptic current induced by applied voltage pulses ($V_{GS} = -5$ mV, 50 ms).

Figure 64. Long-term potentiation at $V_{DS} = -0.2$ V and $V_{PGM} = -1.5$ V with $T_{PGM} = 1$ s and long-term depression at $V_{DS} = -0.2$ V and $V_{ER} = 1.8$ V with $T_{ER} = 0.5$ s of the P3CT- and P3HT-neurofibers.

Figure 65. Cycle test of P3CT- and P3HT-neurofiber for recording long-term potentiation and long-term depression over 45 cycles.

Figure 66. Reproducible and distinct channel conductance of the P3CT-neurofiber defined by each gate under programmed/erased (P/E) pulses ($V_{DS} = -0.2$ V, $V_{PGM} = -1.5$ V, $T_{PGM} = 1$ s, $V_{ER} = 1.8$ V, $T_{ER} = 0.1$ s). Red, green, and blue sections are distinguished by the channel controlled by gate1, gate2, and gate3, respectively; the number of each gate pulse and conductance of the devices are shown in the graph.

Figure 67. Integration of the pulses during operating device and value comparison for response spikes according to gates and program combinations in the P3CT-neurofiber.

Figure 68. Illustration of biological neural network and artificial neural network demonstrated by array of neurofiber (right) and photography of a 10x10 array composed of P3CT-neurofibers.

Figure 69. Plotted transfer characteristics for the devices marked with red circle in the 10x10 array.

Figure 70. Plotted transfer characteristics for the all devices in the 10x10 array.

Figure 71. (a) Process of speech recognition by the tempotron using the P3CT-neurofiber. (b) 2D map of the classification test for accuracy of 10 digits. (c) Comparison of the accuracy in iterative learning for speech recognition between P3HT- and P3CT-neurofibers.

Figure 72. Schematic of fibrous TVS diode based on electrical rectification and composed of metal-iongel-semiconductor.

Figure 73. The I-V curves of various components sandwiched between gold electrodes.

Figure 74. Illustration of the ion migration and redox reaction under forward and backward electric field.

Figure 75. The I-V curves of fibrous TVS diode based on P3HT, P3CT and BBL.

Figure 76. Cyclic voltammograms of P3HT, P3CT and BBL in [TFSI][EMIM] and only [EMIM][TFSI] with Au electrode.

Figure 77. Raman spectra of pristine P3HT and P3CT and after each applying 1V bias for 10 s.

Figure 78. TOF-SIMS depth profile of a pristine P3HT and P3HT films after applying different bias (P3HT/Au/Si).

Figure 79. The I-V curves of fibrous TVS diode according to thickness of P3HT.

Figure 80. (a) TOF-SIMS depth profile and (b) FT-IR spectra of a P3HT films after applying different voltages (P3HT/Au/Si).

Figure 81. (a) I-V curves of fibrous TVS diode and (b) current rectification ratio with iongel prepared from different ionic liquid ratio at 50 mV/s.

Figure 82. (a) I-V curves of fibrous TVS diode with various thickness of iongel at 50 mV/s.

Figure 83. (a) Cyclic voltammograms of P3HT in [TFSI][EMIM] according to different scan rate from 50 mV/s to 1000 mV/s. (b) Plotted curve of oxidation potential and current under cyclic voltammetry.

Figure 84. Time dependence plot of current and rectification ratio of fibrous TVS diode under constant voltage bias.

Figure 85. Current response of a fibrous TVS diode under 2 V field for 1 s.

Figure 86. (a) Transfer characteristic of DSA-fiber TFT before (black line) and after (red line) applying ± 10 V pulses. (b) Photography of DSA-fiber TFT before and after degradation.

Figure 87. (a) Photography of integrated circuit with fibrous TVS diode and DSA-fiber TFT in the textile. (b) Current response of a DSA fiber TFT without (right) and with (left) TVS diode under -2 V and -5 V field for 0.5 s.

Figure 88. Plot of drain current of DSA-fiber TFT during the measurement of ECG.

Chapter 1

Basics of Ion-Gated Organic Thin-Film Transistor

—

A thin-film transistor consists of three electrodes, thin semiconductor layer and an insulating layer. Two of electrodes, which are source and drain respectively, are separated with a short distance on or under semiconductor layer. The last gate electrode is separated from the semiconductor layer by inserting the insulating layer between them (as shown in **Figure 1**).

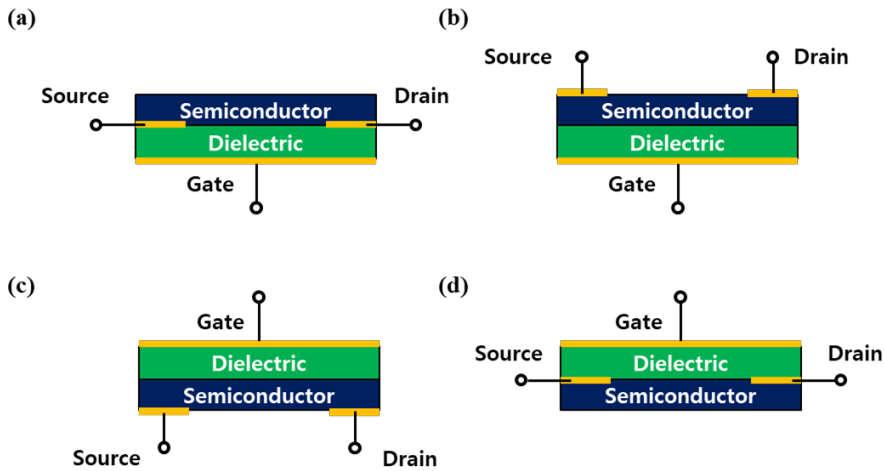


Figure 1. Schematics of thin-film transistor with bottom-gate, (a) bottom-contact and (b) top-contact and top-gate, (c) bottom-contact and (d) top-contact.

Basically, when the voltage applied to gate (V_{GS}), the charge carriers are injected from source to semiconductor and driven from source to drain with applying voltage between source and drain electrodes (V_{DS}), leading to a source-drain

current (I_{DS}). The conductance of semiconductor, which formed by charge carriers, is proportional to gate-voltage. The basic equations for describing drain current are given in below :

Equation (1) at linear regime:

$$I_{DS} = \left(\frac{W}{L}\right) \mu_{lin} C_i \left[(V_{GS} - V_{TH}) V_{DS} - \frac{1}{2} (V_{DS})^2 \right]$$

Equation (2) at saturation regime:

$$I_{DS} = \frac{W}{2L} \mu_{sat} C_i (V_{GS} - V_{TH})^2$$

The parameter of mobility (μ) is the average drift velocity of carrier per unit electric field, where W and L are channel width and channel length, respectively. Threshold voltage (V_{TH}) is known as the minimum gate voltage for accumulating charge carriers at the interface of semiconductor and insulator. Over the V_{TH} , a conducting path from source to drain is formed and it regulates the switching property of the transistor under proper condition of operating device. While V_{DS} is lower than $(V_{GS} - V_{TH})$, I_{DS} is linearly increase followed by V_{DS} . If V_{DS} is higher than $(V_{GS} - V_{TH})$, the density of free charge carriers saturates to approximately zero then I_{DS} becomes ideally saturated. With ability to control current driving and signal processing, the thin-film transistor is an essential component for realizing integration of electronic circuit.

Organic thin-film transistors (OTFTs) based on organic semiconductor as an active layer have demonstrated with several advantages such as low-cost and low-temperature processing, easy modification for adjusting their properties compared to inorganic transistors.^[1] Organic semiconductors are categorized according to polymeric semiconductors (conjugated polymers) and small molecules. Although the OTFT based on small molecular exhibits high mobility and good chemical stability, it is not compatible to low-cost process such as printing due to its poor solubility. Compared to small molecular semiconductor, polymeric semiconductor shows lower mobility. However, good solubility of polymers in a various organic solvent enable to fabricate device by solution process. Among the polymeric semiconductors, poly(3-substituted thiophene) is the most studied and used in various applications with its good processability and solubility.^[2] The strategy to improve performance of the OTFTs based on poly(3-substituted thiophene) is increase π -conjugation lengths. Following the requirement, regioregular poly(3-hexylthiophene) (P3HT) which is substituted with hexyl chain enhances electrical properties with microstructural ordering and improvement in crystallinity.^[3]

Insulator is another critical component in OTFTs for an effective charge injection, transport and electrical characteristics of devices. The basic equations determines capacitance of insulator is given in below :

Equation (3) :

$$C = \frac{k\epsilon_0 A}{d}$$

The parameter of k is the dielectric constant, where A and d are area and thickness of insulator, respectively. A large capacitance of insulator is required to operate device and increase output current under low applied voltage. General method to attain a high capacitance are reducing its thickness by using self-assembly monolayer film or ultrathin crosslinked polymer as an insulator with value of $1 \mu\text{F}/\text{cm}^2$.^[4] Also solid polymer electrolytes composed of polymer matrix including salts are used and provide outstanding capacitance value of $10\text{-}100 \mu\text{F}/\text{cm}^2$.^[5] The movement of cation and anion controlled by gate-voltage results electrical double layer with nanometer thickness as an insulator which leading to high capacitance. However, the low ionic conductivity in polymer electrolytes induce slow polarization which cause low switching speed. In order to enhance ionic conductivity, OTFTs based on iongels as an insulator prepared with ionic liquid in polymer matrix have been demonstrated.^[6] As shown in **Figure 2**, the ions in iongel also form electrical double layer (left) and penetrate into the permeable organic channel layer (right). The infiltrated ions create charge carriers by redox reaction under low voltage ($< 1 \text{ V}$). The two mechanisms enable the iongel gated organic electrochemical transistors based on P3HT exhibit high performance with over 1 mA output current and mobility of $1.7 \text{ cm}^2/\text{Vs}$ under low-voltage operation.

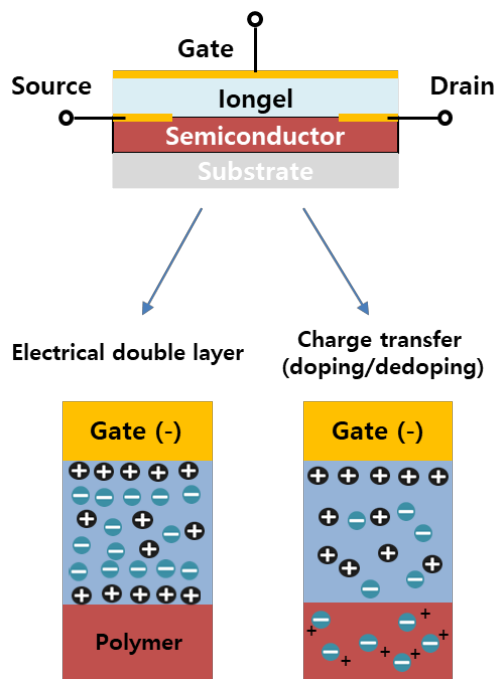


Figure 2. Schematics of an electrolyte-gated organic thin film transistor.

1.1 References

- [1] K. Hagen, *Chem. Soc. Rev.* **2010**, 39, 2643-2666.
- [2] B.S. Ong, Y. Wu, Y. Li, P. Liu, H. Pan, *Chem. Eur. J.* **2008**, 14, 4766-4778.
- [3] B.S. Ong, Y. Wu, P. Liu, S. Gardner, *Adv. Mater.* **2005**, 17, 1141-1144.
- [4] B. Kumar, B.K. Kaushik, Y.S. Negi, *Polymer Rev.* **2014**, 54, 33-111.
- [5] H. Du, X. Lin, Z. Xu, D. Chu, *J. Mater. Sci.* **2015**, 50, 5641-5673.
- [6] S.H. Kim, K. Hong, W. Xie, K.H. Lee, S. Zhang, *Adv. Mater.* **2013**, 25, 1822-1846.

Chapter 2

Fiber-Shaped Ion-gel-Gated Organic Transistor Composed of Double-Stranded Assembly of Microfiber Electrodes for E-textile Application

2.1 Introduction

Integrating computational system into daily costumes of people is an attractive method in wearable technologies which require portability, light weight, deformability and comfort to wear. Electronic textiles (e-textiles) are a promising platforms to satisfy the requirements of wearable devices and fabricate various electronic device such as energy storage, sensors and displays on fabrics.^[1] Web-like structure of textiles and fabric is based on weaved or knitted fibers and enables to bend or stretch freely.^[2] Due to the presence of roughness and pores on textiles, it is delicate to fabricate devices composed of multi-layered thin-films compared to typical flexible substrates. Therefore, to retain the advantages of the textile platform, one-dimensional (1D) fiber-based electronic devices with electrical functionalities have been developed. The ideal 1D fiber-shaped electronic devices enable to realize integrating electronic circuit into a fabric with typical threads and implementing their electrical functionalities. To prove feasibility of the 1D fiber-shaped electronic devices including energy harvesting,^[3,4] storage devices,^[5-7] sensors,^[8-10] light-emitting diodes (LEDs) ^[11,12] and transistors^[13-16] have been demonstrated by many research groups.

In recent years, inclusive review papers on fibrous electronic devices have been released.^[1,2,17,18] Among the fiber-shaped devices, the thin-film transistor based on

fiber (fibrous TFT) is one of the essential components, which enables to control the functionality of e-textiles. As mentioned in basics of thin-film transistor, **Figure 3a** shows the structure of a representative transistor on planar substrate.

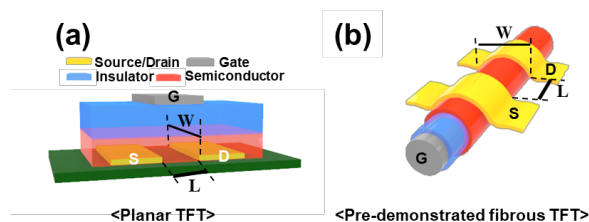


Figure 3. Scheme of the structures of thin-film TFT based on (a) planar substrate and (b) previous reported fiber-shaped TFT. ^[40]

To fabricate fibrous TFT based on a microfiber, implementation of delicate and fine adjusted microstructures should be accompanied on the surface. Only several groups have reported fibrous TFTs fabricated by typical deposition of films or patterning methods.^[15,16,19] In a previous research, Heo et al. demonstrated reel-processable complementary metal-oxide-semiconductor (CMOS) logic circuit with transistor based on selective doped single-walled carbon nanotubes.^[14] The resulted fibrous CMOS inverters based on p- and n-type SWNT transistors fabricated on metal fiber showed high-performance. However, it is not practical method to commercialize the device due to the requirement of vacuum-assisted process such

as thermal evaporation or sputtering and atomic layer deposition (ALD) for metal electrode and insulator layer, respectively. In terms of simple fabrication of the fibrous TFT, organic thin-film transistors (OTFTs) consisting of organic or polymeric materials is perfect solution for TFTs based on 1D fiber. By using a solution process, each multilayer of the TFT can be easily coated on fibers. Recently, the fiber-shaped OTFTs have been reported based on coaxial fibrous structure of metal-insulator-semiconductor (MIS) by coating a solution including semiconductor:insulating polymer blend on metal microfiber. The demonstrated OTFTs composed of MIS coaxial microfibers showed good mobility value of $0.2 \text{ cm}^2\text{V}^{-1}\text{s}^{-1}$ and an on/off current ratio of 10^4 . The possibility of integrating and weaving the fibrous OTFTs into fabric was also confirmed. However, the daily use of e-textiles has been limited by a high operating voltage, low drain current (I_{DS}), unstable contact between electrodes and semiconductor, durability against deformation and wash-resistance.

To further enhance the performance of fibrous TFTs, structural limitations of fiber-shaped TFTs should be also addressed. **Figure 3b** present a typical fiber-shaped TFT which has the limited channel length (L) and width (W) of the device by the dimension of the microfiber. The dimension of channel width was restricted by the half circumference of the microfiber. As following equation 1, the limited width of the device exhibits a low drain current which is difficult to control the

circuits such as current-driven LED. In spite of these limitations, up to date, no alternative has been suggested.

In this chapter, I introduce a new structure of a fiber-shaped organic transistor composed of a double-stranded assembly of electrode microfibers (DSA-fiber TFT).

^[13] **Figure 4** shows the basic architecture of the proposed DSA-fiber TFT. As effective strategies to overcome limitations mentioned above, firstly, microfibers used as the source and drain electrodes covered by polymer semiconductor layer was twisted to form semiconductor channel of the fiber TFT. This architecture facilitates controlling the channel width and length easily by handling the length of twisted two electrode microfibers and thickness of the semiconductor coated on them, respectively. It is not required of sophisticated vacuum-assisted patterning process to determine a channel dimension with S/D electrode contact for the overall fabrication process of DSA-fiber TFT. Furthermore, sub-micrometer short length of the channel, which is not easy for the previous structure of fiber TFT, can be realized by coating thin-film on the electrode microfibers. Secondly, an iongel was employed as an insulator to accomplish low-voltage operational fibrous TFT. As mentioned in basics of chapter 1, by a large amount of electron transfer between iongel and organic semiconductor channel and formation of a nanometer electric double layer at low applied voltages, iongel can induce a high electrical performance and capacitance.^[20,21] The iongel capable of solution processing is

optimized for the fabrication of fiber-shaped devices.^[22] In addition, the long-range polarizability of iongel enable to inaccurate alignment of gate electrode on channel between S/D electrodes.^[23] By taking advantage of this aspect, implementation of gate electrode by winding a conductive fiber followed around iongel, which covers on twisted electrodes, is possible. It is worth noting that structure of the DSA-fiber TFT enables to interconnect easily with other electrical components even after coating passivation layer on surface of the completed devices.

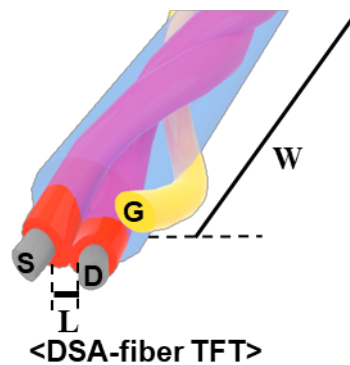


Figure 4. Schematic of fibrous thin-film transistor based on double-stranded assembly.

While the realization of a DSA-fiber TFT, it was found that modifying the crystallinity of semiconductor nanostructure for channel has critical role to prevent electrical failure between S/D electrodes and make the charge carrier transport of the device improved. The demonstrated DSA-fiber TFTs showed high electrical

performances with an output current of over -10 mA under -1.3 V of gate bias and an on/off ratio of 10^5 . By varying the length of twisted electrodes and the thickness of the coated semiconductor, the expected current was observed as followed by equation 1. The DSA-fiber TFT showed outstanding durability and almost maintained its initial electrical properties even after repeated bending and a harsh washing process using a strong detergent solution. The demonstrated DSA-fiber TFT facilitates controlling intensity and on/off switching of current-driven LED devices and signal amplification from human body as proof of practical fibrous TFTs.

2.2 Experimental Method

Materials: Gold microfibers with 0.1 mm diameter (purity: 99.95%) were purchased from Alfa Aesar. 1-ethyl-3-methylimidazolium bis(trifluoromethylsulfonyl)amide ([EMIM][TFSI]), poly(vinylidene fluoride-co-hexafluoropropylene) (P(VDF-HFP), $M_n=130 \text{ kgmol}^{-1}$ and $M_w=400 \text{ kgmol}^{-1}$), cyclohexanone, chlorobenzene, and dopamine hydrochloride were purchased from Sigma-Aldrich. Poly(3-hexylthiophene-2,5-diyl) (P3HT) (91–94% regioregularity, M_w 50–70 kgmol^{-1} , 4002-EE) and Ecoflex 00-30 were purchased from Rieke Metals and Smooth-On Inc. (<http://www.smooth-on.com>), respectively.

Device fabrication: Dissolving P3HT in chlorobenzene with a concentration of 70 mg/ml and this solution was called P3HT solution. For P3HT-nanorod (P3HT-NR) in the solution, 0.3 ml of cyclohexane was slowly added to 70 mg/0.7 ml of P3HT dissolved in chlorobenzene. Before coating of the semiconductor layer, modification with utilizing Au microfibers in an aqueous tris-HCl buffer solution (pH=8.5) mixed with dopamine (2 mg of dopamine per ml of 10 mM tris-HCl) for 1 h and then rinsing with deionized water was utilized. The modified Au microfiber was coated with the semiconductor solution by using a home-built die-coating system composed of two moving stages and a T-shaped glass tube as a reservoir (**Figure 5**).^[13] The tube with a diameter of 3 mm was full with the solution of P3HT NR or P3HT. By the moving stages, the microfiber was moved through the tube with a constant speed in the horizontal direction. After P3HT-coated microfibers were dried in a vacuum oven at 70 °C overnight to remove the residual solvent, each end of the two microfibers was fixed to two slide glasses placed parallel to each other with a distance of 50 mm and then entwisted by rotating one side to fabricate a double-strand assembly of the P3HT-coated electrode microfibers, as shown in **Figure 6**. P(VDF-HFP) and [EMIM][TFSI] were dissolved in acetone with the polymer, ionic liquid, and solvent mixed in the ratio of 1:4:8 by weight to prepare the iongel. After dropping prepared mixture along the twisted assembly of the double-stranded microfibers fixed vertically to the ground, the Au microfiber

(100 μm) was wound around the surface of iongel to form a gate electrode. Ecoflex mixed with equal volumes of pre-polymer A and pre-polymer B was coated to prepare a passivation layer on the fabricated device.

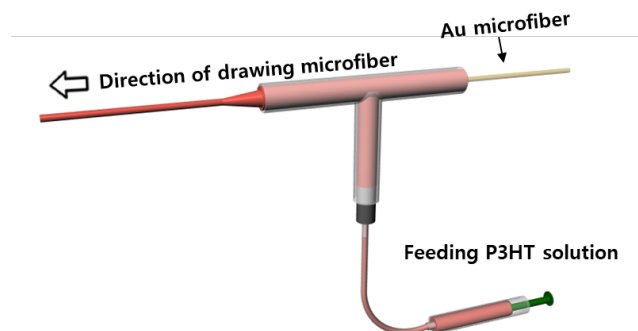


Figure 5. Scheme of die-coating system for coating P3HT layer on microfiber.

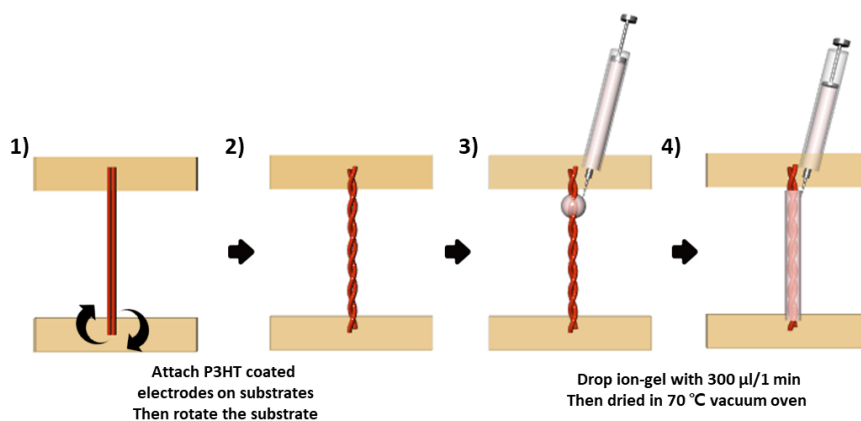


Figure 6. Scheme of process to twist microfibers covered with semiconductor layer and utilize iongel on twisted microfibers.

Characterization: The morphology of the crystalline structure of P3HT films on the Au microfiber was observed by optical microscopy (Nikon LV100N). To determine the thickness of the P3HT films, cross-sectional images were captured using a scanning electron microscope (SEM) with focus ion beam (FIB) milling (Helios NanoLab 600). The SEM images of the twisted microfiber electrodes were obtained using a SEM with a field-effect gun (Inspect F). The UV-vis absorption spectra of the P3HT solution were measured on a UV/VIS/NIR spectrometer (Lambda 750, PerkinElmer). The 2D grazing incident X-ray diffraction (GIXD) measurements were performed at the 3C-SAXS beamline in the Pohang Accelerator Laboratory. The X-ray beam ($\lambda = 1.2296$ nm) was incident at a grazing angle ranging from 0.05° to 0.09° for 5 s. Atomic force microscopy (AFM, Multimode 8, Bruker) measurements were performed for analyzing P3HT films spin-coated with a thickness of 2 μm or drop-cast with a 0.0025 wt% solution on a silicon substrate. The hardness of the 2 μm -thick P3HT films was measured by the nano-indentation method (Ultra precision surface Mechanical Analyzer, Anton Paar). The electrical properties of the DSA-fiber organic TFT devices and ECG recording were measured using an Agilent 4155B semiconductor device analyzer under ambient conditions. The luminescence of the LED controlled by the fiber TFT was measured with a spectra scan spectroradiometer (PR-670) and a source

measure unit (Keithley-2601). The ECG was recorded by connecting the ground to the chest and the gate to the wrist. The baseline of the resulting current trace according to time was subtracted to obtain the signal clearly.

2.3 Results and Discussion

Figure 7 shows a whole process for fabricating DSA-fiber TFTs. It was started from surface modification of Au microfiber due to its poor surface wettability and interfacial adhesion with the polymer materials.^[13] As a surface modifier and surface-adherent polymer for Au microfibers, Polydopamine (pDA), which is deposited on Au microfibers with very thin layer (<10 nm) and effectively modified the surface characteristics of Au and changed it hydrophilic, was used.^[24] After that, a representative poly(3-hexylthiophene) as a semiconductor was coated with die-coating method. Compared to conventional dip-coating method, the die-coating method can systemically control a thickness of thin-film coated on microfibers.^[13] By varying the movement speed of microfibers, the thickness of thin film in the range from 60 nm to 260 nm coated on microfiber was controlled. (**Figure 8**). **Figure 9a** shows the surface of a uniform P3HT film coated on microfiber captured by optical microscopy and cross-sectional SEM image. As S/D electrodes, Au microfibers coated with P3HT were twisted and connected to form a channel as shown in **Figure 9b**. The 3.8 cm-long homogeneous connected P3HT

channel based on twisted microfibers was captured by SEM, as shown in **Figure 10**. Next, an iongel, which prevent the structure of double-stranded assembly from loosening, is composed of P(VDF-HFP) and [EMIM][TFSA] was drop-coated on the twisted electrode microfibers. [10,21] The Au microfiber as a gate electrode was put around the surface of iongel layer. Lastly, the eco-flex as a passivation layer was drop-coated on the DSA-fiber TFT for the stability of the device against external oxygen, moisture and chemicals and fitting gate microfibers on iongel.

The final configuration of the DSA-fiber TFT, which has a fiber-shaped with a diameter of 600 μm , is presented in **Figure 11a**. At the end of the device, the three electrodes (i.e. source, drain and gate electrode) of DSA-fiber TFT are exposed for interconnection with other electronic devices. As shown in **Figure 11b**, the cross-sectional SEM image of the DSA-fiber TFT indicates that the channel between source and drain electrodes is formed based on P3HT film and the thickness of the iongel and passivation layer were 200 μm -thick and 100 μm -thick, respectively.

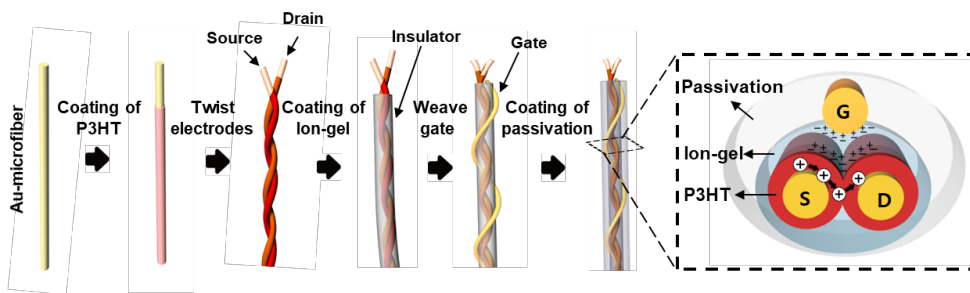


Figure 7. Scheme of holistic fabrication for DSA-fiber TFT.

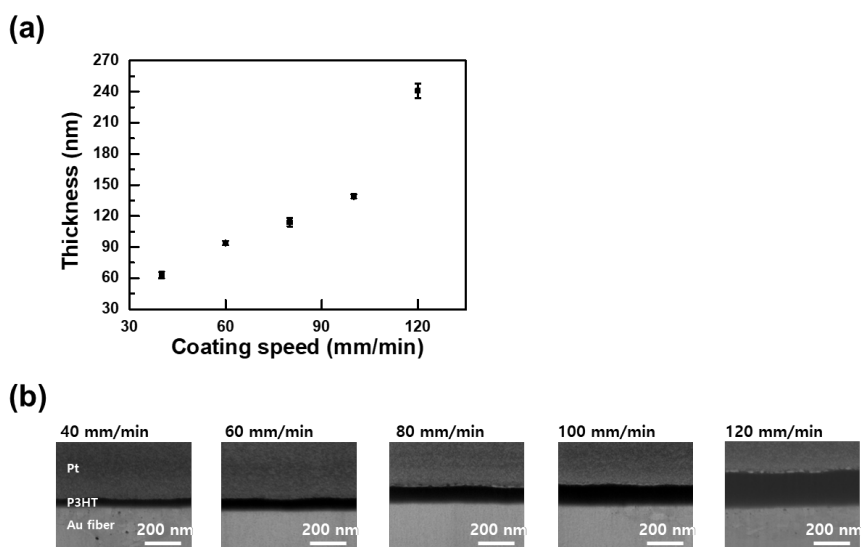


Figure 8. (a) Controlled thickness of thin-film coated P3HT-NR on microfibers by changing the drawing speed. (b) SEM images of cross-sectional P3HT NR film covered on microfibers.

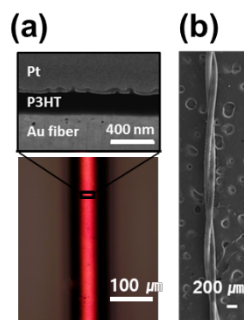


Figure 9. (a) Image of P3HT film coated on Au-microfiber captured by cross-sectional SEM and optical microscope. (b) Top SEM image for double-stranded assembly of microfibers with coated P3HT film.

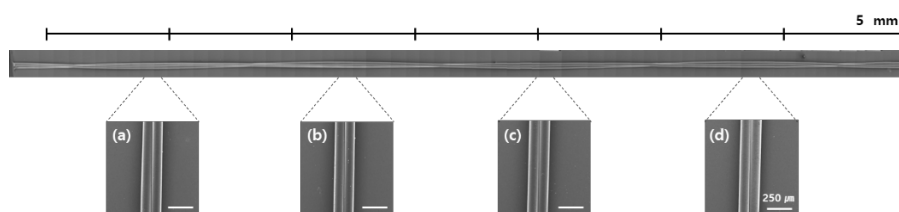


Figure 10. Top-view SEM images for investigation of homogeneity in twist assembled P3HT-coated electrode microfibers with 3.8 cm-length. (a)-(d) The enlarged images with interval of 7.5 mm confirmed connection between two electrode microfibers along the 3.8-cm of twisted assembly.

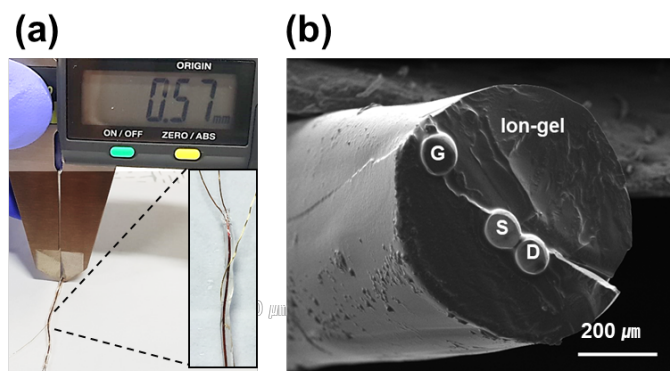


Figure 11. Final fabricated DSA-fiber TFT captured by (a) photography and (b) Cross-sectional SEM.

For the torsion of electrode microfibers coated by P3HT, tearing or exfoliation of the P3HT thin film coated on the Au microfibers should be considered, due to device failure and electrical breakdown between source and drain electrodes. In fact, only 10% of the fabricated devices shows normal operation, when the DSA-fiber TFTs using electrodes coated by featureless P3HT films (220 nm thick). In addition, controlling molecular orientation of P3HT film is also considered for realization of high-performance fibrous OTFTs due to the charge carrier transport in the polymer semiconductor, which highly depends on the molecular stacking of the polymer. [25] These issues were addressed by a high crystallinity of P3HT based on nanostructure. It is known that P3HT normally tends to form one-dimensional

nanowires via stacking of hydrophobic aliphatic chains and π - π interactions, which has highly crystallinity. By increasing the crystalline phase of P3HT film and utilizing a highly ordered polymer, P3HT film showed robust film as well as improvement in field-effect mobility of the OTFTs.^[25-29]

To coat P3HT solution on electrode microfibers by die-coating process, formation of self-assembled P3HT chains based on crystalline aggregates should be finished in the solution phase. In general, self-organized P3HT nanowires were induced in dilute solution by changing solubility of polymer in a chlorobenzene solution adding cyclohexanone which is well miscible with chlorobenzene but non-solvent for P3HT. However, a highly concentrated self-organized P3HT solution with a concentration of 7.0 wt% is needed to coat P3HT on electrode microfibers.^[27] So, I investigated the self-organized P3HT in highly concentrated mixed solution by UV-vis spectroscopy with various stirring time of the solution (i.e., aging time at RT) (**Figure 12**). It is found that absorption shoulder shifted from 475 nm to 550 nm, which indicates change in the inter-planar stacking of P3HT, and saturated after the solution was stirred (aged) for 7 days. This indicated that the formation of self-organized P3HT chains with high concentration was almost complete after a week. When P3HT films was prepared from a highly concentrated mixed solution, a unique feature consists of 60 nm-sized nanogranules (P3HT-NG) was observed, as shown in **Figure 13a**. The

nanostructures from high concentration has significantly different feature compared to the nanowire or nanofibril as typical structures of P3HT. [30-33] Interestingly, the formation of nanorod structure (P3HT-NR), which is based on one-dimensionally interconnection between P3HT-NG, was observed after stirring over 7 days (**Figure 13b**). **Figure 13c, d** show the morphology of P3HT-NG and -NR films prepared from the 0.0025 wt% of P3HT in mixed solutions using a chlorobenzene and cyclohexanone (7:3) solvent. Both nanofibrils (approximately 2 nm in height and 30 nm in width) and nanorods (approximately 6 nm in height and 60 nm in width) co-exist are observed in the P3HT-NG films prepared from the 1 h-aged mixed solution and widely distributed on the substrate surface (**Figure 13c**). This implies that nanorods composed of one-dimensionally interconnected nanogranules start to develop at the early state of the self-organization while the residual P3HT chains not involved in the formation of nanogranule become the nanofibrils on the substrate surface during film-forming step. In contrast, nanofibrils were not formed and only nanorod structures can be observed after aging solution in 7-day which is enough time to form P3HT-NR as shown in **Figure 13d**. This indicates that almost all of the P3HT chains in the solution get involved in formation of the nanorod aggregates. Interestingly, it is found that there is no independently isolated nanogranules in both films. This implies that nanorod are not formed by connection of the formerly aggregated nanogranules but created along with generation of

nanogranules. The AFM images show more clear trend depend on aging time (**Figure 14**). As far as I know, P3HT nanorods consisting of distinguished and interconnected nanogranules have been rarely observed.^[34,35] The formation of nanogranules structure in P3HT thin films aggregated under a solvent-vapor pressure is reported.^[34] In a thin P3HT film, nanowires are composed of ordered rod-like aggregates. In a previous research based on bridging-chain model and high molecular weight P3HT (>10 kDa), it is supposed that the self-assembled P3HT chain in crystalline structure (lamellae) is enable to spread out in the amorphous region or fold back to the original lamellae.^[36] Even though further studies on the orientations of the nanorod structure is still required, P3HT nanorods consisting of interconnected nanogranules may be described by this bridging-chain model. In a high concentration of P3HT, the distance between each P3HT molecules is short and it causes many chance to extent P3HT chains into another crystalline nanogranule structure. So this is can lead to the formation of nanorod structure consisting of one-dimensionally interconnected nanogranules.

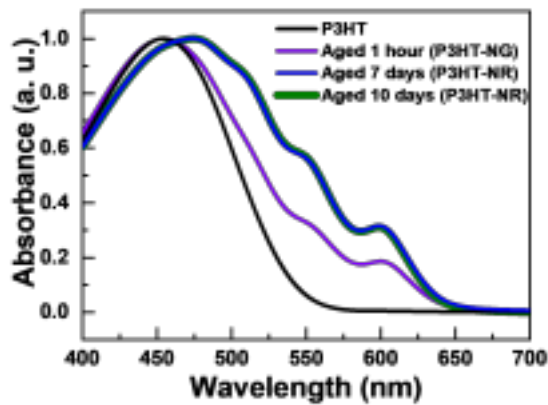


Figure 12. UV-vis spectra of P3HT solution in various stirring time from 1 hour to 10 days.

present height profiles of cross-sectional AFM extracted from the each colored dash lines.

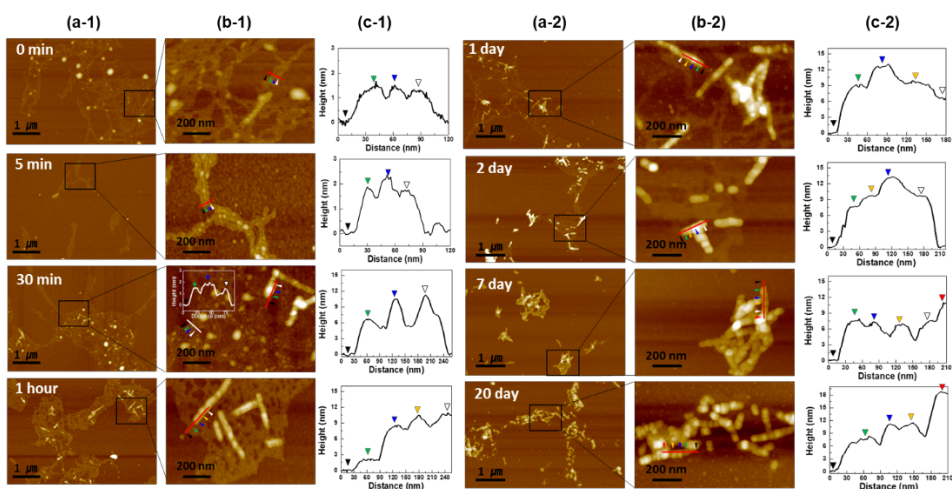


Figure 14. AFM topography images for nanostructure of P3HT films prepared with a 0.0002 wt % in solvent mixture under different aging times from 0 min to 7 days.

The grazing incidence X-ray diffraction (GIXD) reveals the molecular orientation of crystalline P3HT with various aging time. **Figure 15a** shows the ordered P3HT chains with lamellar stacking and edge-on orientation in P3HT-NG films. Compared to P3HT-NG films, a slightly shifted (100) reflection to a lower angle was observed. Also P3HT-NR films show decreased the full width half maximum which indicates that aging of the solution enable to improve crystal perfection of P3HT films (**Figure 16a**). Especially, in-plane direction, the (100) reflection was observed in P3HT-NR films. This indicates enhancement of face-on

stacking of P3HT chains by aging of the solution (**Figure 15b**). Extracted GIXD plots the q_z and q_{xy} axis were analyzed to identify the increase in the face-on stacking in the P3HT-NR film. (**Figure 16a and 16b**). In general, P3HT molecule prefers edge-on orientation in P3HT thin film during the surface-mediated crystallization.^[37, 38] In this work, however, self-organization of P3HT during aging the solution was almost complete before the casting of the films and it might restrict surface-mediated crystallization. Therefore, it is assumed that the formation of increased face-on stacking in P3HT-NR films is induced by multiple crystalline domains in a nanorod structure which is already crystallized in highly concentrated solution. In addition, it is well-known that charge carrier transport passing through π - π stacking direction in the P3HT films is more beneficial than the transport along alkyl side chain stacking direction. As shown in **Figure 17**, it is inferred that face-on stacking in P3HT-NR film on the fiber electrodes provides more efficient charge carrier transport through π - π stacking in the DSA-fiber TFTs.

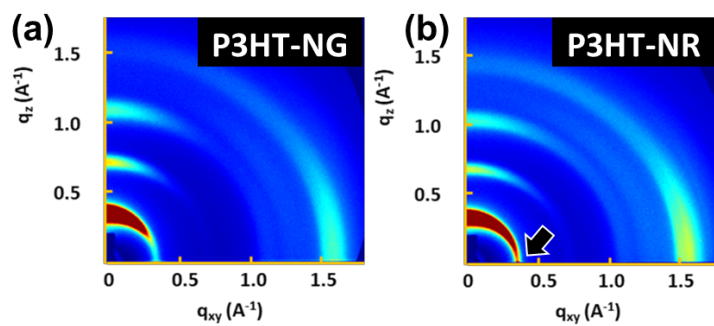


Figure 15. Two-dimensional GIXD images of the (a) P3HT-NG and (b) P3HT-NR film

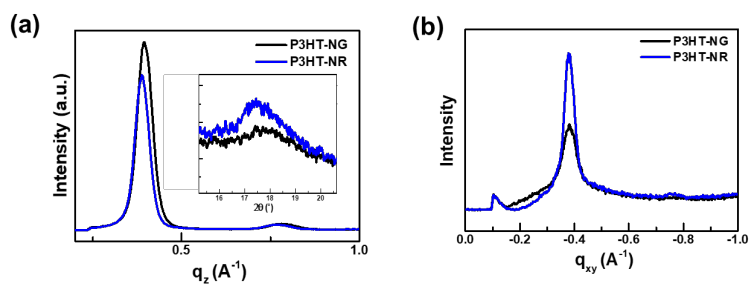


Figure 16. (a) Out-of-plane and (b) in-plane GIXD plot to compare the P3HT-NG and P3HT-NR films.

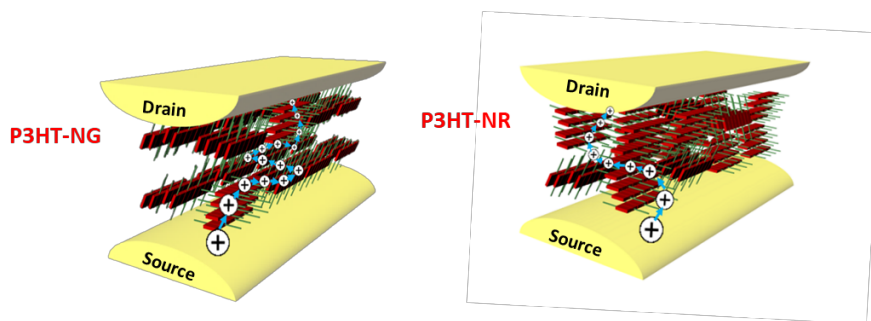


Figure 17. Schematics of preferred and expected charge transport paths with double-stranded assembly.

The hardness of pristine P3HT and nanostructured P3HT films were investigated by the nano-indentation measurement. The average hardness of P3HT-NR film (86 MPa) shows a 17.8% higher value than that of the P3HT-NG film (73 MPa) as shown in **Figure 18**. While the production yield of the device with pristine P3HT films only was 10 %, the device yield of the DSA-fiber TFTs based on the improved hardness of the P3HT-NG and P3HT-NR films considerably increased 40% and 76%, respectively (Table 1). The enhanced crystalline perfection attributes to the increased hardness of P3HT-NR film compared to that of the P3HT-NG film. In addition, the increased face-on orientation in the P3HT-NR film, which has the π - π staking direction against the external force of nano-indentation, also contribute to enhanced hardness of P3HT-NR film because the molecular

interaction based on π - π stacking is much stronger than the interactions between the alkyl side chains.^[39]

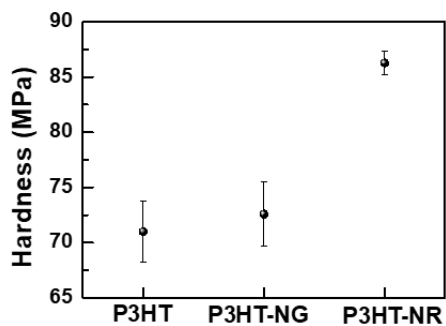


Figure 18. Hardness of P3HT, P3HT-NG and P3HT-NR analyzed by nano-indentation measurement.

Table 1. Electrical characteristics of DSA-fiber TFTs based on P3HT nanostructure.

Semiconductor	Electrical parameters				
	Yield (%)	Transconductance ^{avg} ($\mu\text{S}/\text{mm}$)	$I_{\text{on}}/I_{\text{off}}^{\text{avg}}$	$V_{\text{th}}^{\text{avg}}$ (V)	SS (Vdec ⁻¹)
P3HT NG_260nm	40	84.0 (± 1.2)	8.43×10^4 ($\pm 2.92 \times 10^4$)	-0.87 (± 0.257)	0.26 (± 0.11)
P3HT NR_260nm	76	111.8 (± 2.2)	1.46×10^5 ($\pm 0.84 \times 10^5$)	-1.01 (± 0.075)	0.20 (± 0.09)

Figure 19 presents the transfer and output characteristics of the device with the P3HT-NR films. The DSA-fiber TFTs showed a general behavior of field-effect transistor and good on/off current ratio over 10^5 at voltages below -1.5 V. As

increasing drain voltage, the drain current shows a transition from linear regime to saturation regime, which represents the device with a low contact resistance. Furthermore, it is indicated that the hole carriers from the source electrode inject into the P3HT layer and successfully transport to the drain electrode even though the two P3HT layers on microfiber electrodes were contacted physically. Due to the electrical double layer inducing high capacitance of the iongel insulator and the electrochemical doping which increase charge carriers in P3HT, as anticipated, the DSA-fiber TFT shows a high output drain current over -5 mA at low applied bias of $V_{GS} = -1.3$ V and $V_{DS} = -0.5$ V.^[20] In **table 1**, the summarized electrical performance of the devices based on P3HT-NG and P3HT-NR films are presented. Compared to the DSA-fiber TFT based on P3HT-NG, the device based on P3HT-NR showed higher transconductance. This result supports that the face-on stacking of P3HT film on microfiber electrodes provides more efficient path for charge carrier transport in DSA-fiber TFTs.

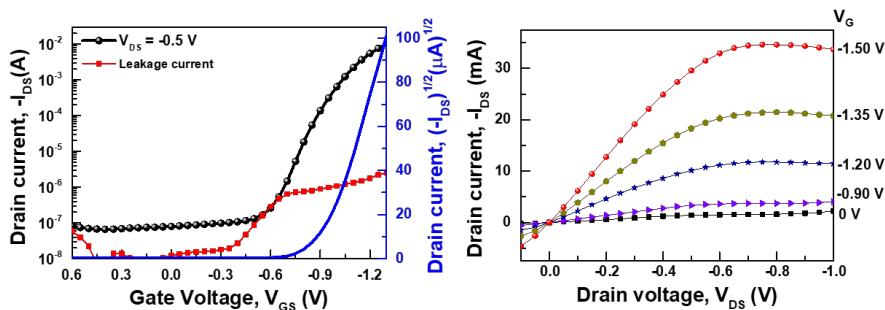


Figure 19. Transfer and output characteristics of the DSA-fiber TFT based on P3HT-NR film.

As mentioned above, the important advantage of the DSA-fiber TFTs is that the dimension of the semiconductor channel can be easily controlled without a patterning process based on vacuum-deposition. The drain currents of the DSA-fiber TFT according to the thicknesses of the P3HT-NR film on Au-microfiber are shown in **Figure 20a**. As a typical current variation along with the channel length, the inverse proportion between drain current of the device and the thickness of the P3HT film is identified. For controlling channel width, the change of drain current in the linear regime ($V_{DS} = -0.5$ V) with increasing length of the DSA-fiber TFT is confirmed, as shown in **Figure 20b**. At a constant $V_{GS} = -1.3$ V to $V_{DS} = -0.5$ V, the drain current was controlled from -0.23 to -9.6 mA by varying the length of double-stranded assembled microfibers from 1 cm to 4 cm. Based on this result, it is confirmed that the architecture of DSA-fiber TFT provide the simple method to

control channel dimension of the DSA-fiber TFTs by varying the length of the microfiber electrodes and the thickness of the semiconductor.

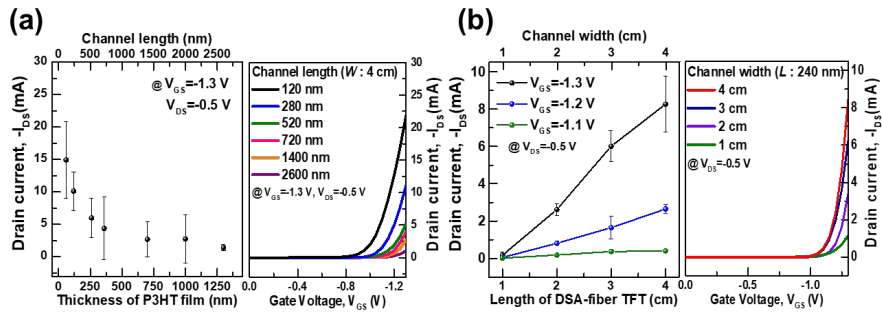


Figure 20 . Plot of drain current (I_{DS}) versus (a) channel length, which accords with thickness of semiconductor film coated on microfiber electrode (left) and (b) channel width, which is corresponds on length of DSA-fiber TFT (left). The transfer characteristics (V_{GS} - I_{DS}) of the device with various (a) channel length (right) and (b) channel width (right).

The directly embedded DSA-fiber TFTs in the textile woven from common woolen yarns showed the excellent electrical performance of the device and were retained with no significant changes under the weaving process for integration (**Figure 21**). The iongel and passivation layers coated on the double-stranded assembly of the microfibers allowed the device to bear specific bending deformations. **Figure 22a** shows the variation of the transconductance and difference of threshold voltage of DSA-fiber TFTs at each bending radius. Even

after the device was deformed with a bending radius of 2.0 mm, the change of transconductance and threshold voltage of the device were remained up to 80% of each initial values. In addition, as shown in **Figure 22b**, the durability of the embedded DSA-fiber TFT in textile against an repeated bending motion (bending radius : 7.0 mm) was evaluated. Even after bending device over 1000 times, the electrical performance of the DSA-fiber TFT was retained. This result indicates that the DSA-fiber TFT based on the new architecture with assembly of microfiber electrodes has substantial durability and potential for application to practical wearable devices.

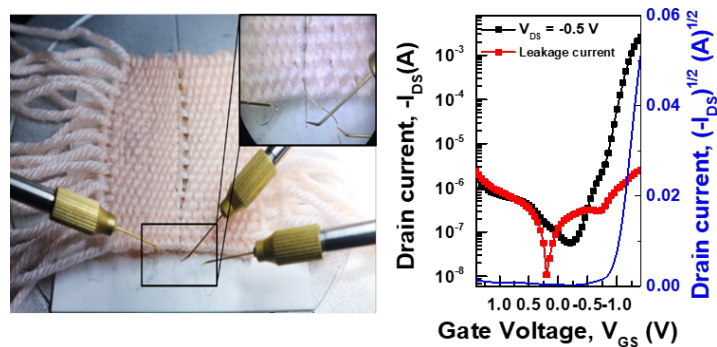


Figure 21. Photograph and transfer characteristics of the embedded DSA-fiber TFT in the textile.

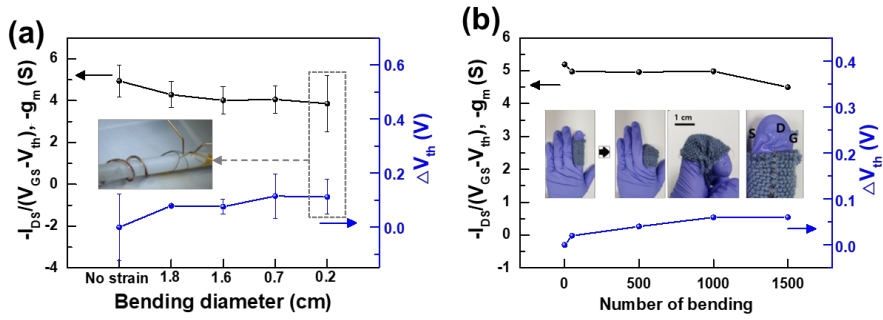


Figure 22. (a) Variation of transconductance (left) and shift of threshold voltage (right) under each bending condition. (b) Variation of transconductance (left) and shift of threshold voltage (right) versus number of bending cycles (bending diameter : 7 mm).

Even though the washability of the fiber-shaped devices is mentioned as an important issue for daily wearable e-textile, the previously reported fibrous TFTs have been limited to coat passivation layer for wash resistance due to problem in integration with other devices. In contrast, the demonstrated DSA-fiber TFT is able to be directly passivated by coating the passivation layer on the device with simple connections to other components. To evaluate the wash resistance of the DSA-fiber TFTs passivated by ecoflex, the demonstrated devices were immersed for an hour and stirred at 550 rpm in a detergent solution with a strong bleaching agent. Even when the device without a passivation layer was dipped in a distilled water, the electrical performance of the device showed serious degradation and did not

exhibit switching with an on/off current ratio (**Figure 23**). On the other hand, even after the DSA-fiber TFT passivated by ecoflex layer was immersed in detergent solution, the device showed the almost same electrical characteristics as performance of initial device. As far as I know, this is the first demonstrated fiber-shaped transistor with wash-resistance.

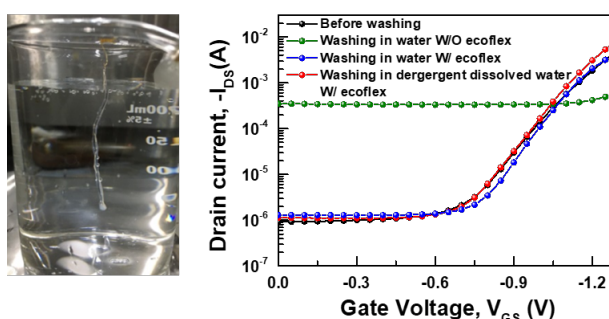


Figure 23. Transfer curves of the device for comparison in various condition ; Before (Black) and after (Blue) washing in distilled water with passivation layer, after immersing in water without passivation layer (Green), after washing in detergent dissolved water with passivation layer (Red).

After all, output devices including LEDs and sensors should be integrated into a textile platform for communicating the outside world or human body. Operating a

LED with the DSA-fiber TFTs as a proof of concept was tested. As shown in **Figure 24**, the DSA-fiber TFTs embedded in fabrics was directly integrated with conventional red-LED. A 150 μA level drain output current from DSA-fiber TFTs with changing drain voltage ranging from -3.5 V to -5.0 V is enable to actively control the luminescence and the on/off switching of LED. **Figure 25** shows a simple demonstration of electronic circuit with the red (R), green (G), and blue (B) LEDs-embedded in textile and connected to each DSA-fiber TFTs. This prototype identified that the demonstrated DSA-fiber TFTs stably controlled on/off switching of the LEDs.

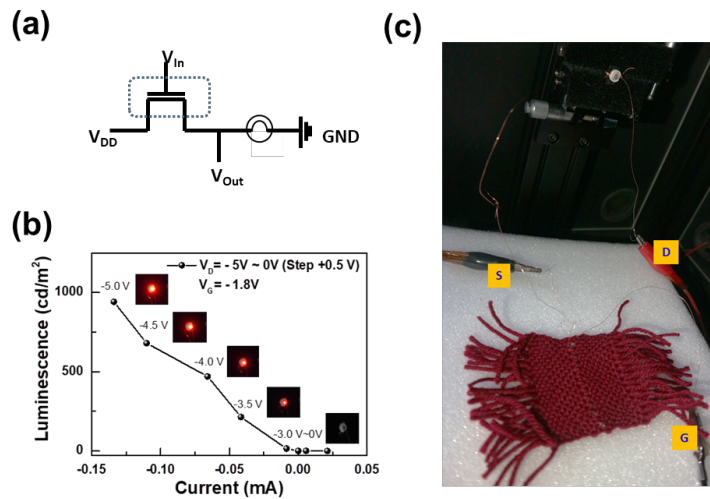


Figure 24. (a) Diagram for controlling luminescence of conventional LED by DSA-fiber TFT. (b) The luminescence efficiency of red LED versus output current controlled by

embedded-DSA-fiber TFT in fabrics (c) Photography of LED connected with DSA-fiber TFT embedded in textile.

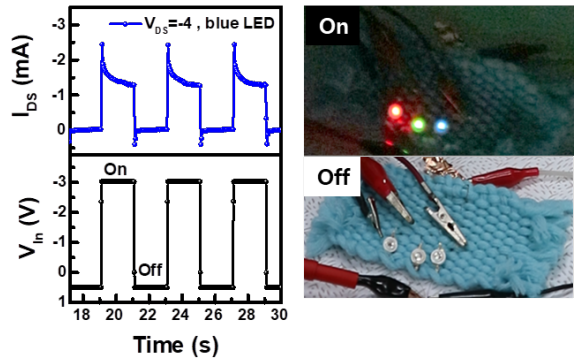


Figure 25. Plot of drain current (top) under output voltage (bottom) under applying 0.5V and -3V (left) and photograph of RGB-LED connected with textile-embedded DSA-fiber TFT for controlling on/off switching (right).

Monitoring human body signals in real time is mentioned as one of the most appropriate application of e-textile. To confirm the potential of DSA-fiber TFTs for monitoring health of human-body, I recorded electrocardiogram (ECG). As shown in **Figure 26b**, the gate and source microfiber electrodes of the device were connected to the wrist and chest of the human body and the drain current was recorded at $V_{DS} = -0.1$ V. Few hundred microvolt differences in ECG signals

derived from contraction and relaxation of muscle cells can be amplified by considering sub-threshold which depends on gate voltage applied to transistors. At the off-state ($V_{GS} < V_{th}$), the change of drain current was ~ 25 nA along characteristic spikes of the heartbeat monitored by potentiometric recorder (**Figure 26a**). Interestingly, when the sub-threshold swing regime ($V_{GS} > V_{th}$) was applied to the DSA-fiber TFTs, the spike of drain current was amplified to ~ 40 nA, as shown in **Figure 26a**. P-Q-R-S-T sub-waves, which are related to the depolarization of arteries and ventricles, was observed in the enlarged spike of one signal (**Figure 26c**). This result clearly shows the sufficient resolution for detecting ECT signal and high applicability of DSA-fiber TFT to adjust wearable healthcare monitoring devices based on e-textile.

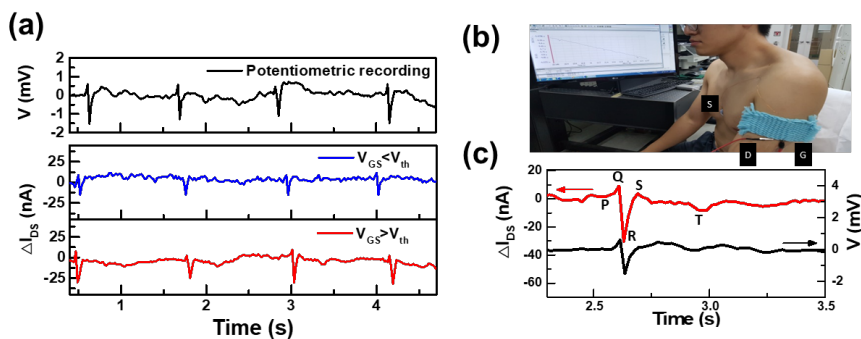


Figure 26. (a) Drain current of DSA-fiber TFT (blue and red line) occurred by potential change of ECG (black line). (b) Photograph of electrode contacts on skin for monitoring ECG signal. (c) Plot of drain current (black line) and potentiometric recording (blue line) during measuring a single cardiac cycle of ECG with DSA-fiber TFT.

2.4 Summary

A new architecture of a fiber-shaped organic transistor based on a double-stranded assembly of microfiber electrodes as a promising breakthrough for overcome low output current of reported fibrous transistor technology has been successfully demonstrated. The key aspect of the designed fibrous transistor is controlling semiconductor channel of the transistor by twisting source and drain electrode microfibers coated by semiconductor layer which is referred as double-stranded assembly. This structure provides simple method to control the

channel length and width of the fibrous transistor by varying the thickness of the semiconductor layer coated on microfibers and the length of twisted microfibers, respectively. To enhance the mechanical hardness of the polymer film for prevention of electrical failure by shorting between drain and source microfiber electrodes and achieve an increased transconductance by deriving beneficial molecular orientation for effective transport of charge carrier, it should be noted that controlling crystalline structure of the polymer is a crucial factor. In addition, to attain low voltage operational devices exhibit high output current, an iongel as an insulator with a high capacitance based on electrical double layer and a solution processibility. As a result, fiber-shaped transistor showing a good on/off ratio of 10^5 at low voltages under -1.3 V and high output current over 5 mA were demonstrated. The electrical performance of demonstrated fibrous transistors were almost retained even after integration into the textile by weaving the device and repeated bending test. The suggested architecture of the device is enable to coat a passivation layer along outermost surface of the fibrous transistor without any connection problem, and the good wash resistance was realized by the passivated device. At last, operating LED devices and detecting ECG signals from a human body was successfully achieved with the fiber organic transistor. was successfully applied to actively operate LED devices and in the detection of ECG of a human body. This work may provide a prospective strategy for developing and utilizing

practical fiber-shaped electronic devices in e-textile applications.

2.4 References

- [1] A. K. Yetisen, H. Qu, A. Manbachi, H. Butt, M. R. Dokmeci, J. P. Hinestroza, M. Skorobogatiy, A. Khademhosseini, S. H. Yun, *ACS Nano* 2016, 10, 3042.
- [2] W. Zeng, L. Shu, Q. Li, S. Chen, F. Wang, X. M. Tao, *Adv. Mater.* 2014, 26, 5310.
- [3] M. R. Lee, R. D. Eckert, K. Forberich, G. Dennler, C. J. Brabec, R. A. Gaudiana, 2009, 324, 232.
- [4] Z. Wen, M.-H. Yeh, H. Guo, J. Wang, Y. Zi, W. Xu, J. Deng, L. Zhu, X. Wang, C. Hu, L. Zhu, X. Sun, Z. L. Wang, *Sci. Adv.* 2016, 2, 1600097.
- [5] Y. Huang, H. Hu, Y. Huang, M. Zhu, W. Meng, C. Liu, Z. Pei, C. Hao, Z. Wang, C. Zhi, *ACS Nano* 2015, 9, 4766.
- [6] S. H. Ha, S. J. Kim, H. Kim, C. W. Lee, K. H. Shin, H. W. Park, S. Kim, Y. Lim, H. Yi, J. A. J. J. o. M. C. A. Lim, *J. Mater. Chem. A* 2018, 6, 6633.
- [7] Y. Zhang, Y. Zhao, J. Ren, W. Weng, H. Peng, *Adv. Mater.* 2016, 28, 4524.
- [8] K. Cherenack, C. Zysset, T. Kinkeldei, N. Münzenrieder, G. Tröster, *Adv. Mater.* 2010, 22, 5178.
- [9] T. Q. Trung, H. S. Le, T. M. L. Dang, S. Ju, S. Y. Park, N. E. Lee, *Adv. Hhealthcare mater.* 2018, 1800074.
- [10] J. Lee, H. Kwon, J. Seo, S. Shin, J. H. Koo, C. Pang, S. Son, J. H. Kim, Y. H. Jang, D. E. Kim, *Adv. Mater.* 2015, 27, 2433.
- [11] Z. Zhang, K. Guo, Y. Li, X. Li, G. Guan, H. Li, Y. Luo, F. Zhao, Q. Zhang, B. Wei, *Nat. Photonics* 2015, 9, 233.
- [12] S. Kwon, H. Kim, S. Choi, E. G. Jeong, D. Kim, S. Lee, H. S. Lee, Y. C. Seo, K. C. Choi, *Nano lett.* 2017, 18, 347.

- [13] H. M. Kim, H. W. Kang, D. K. Hwang, H. S. Lim, B. K. Ju, J. A. Lim, *Adv. Funct. Mater.* 2016, 26, 2706.
- [14] J. S. Heo, T. Kim, S. G. Ban, D. Kim, J. H. Lee, J. S. Jur, M. G. Kim, Y. H. Kim, Y. Hong, S. K. Park, *Adv. Mater.* 2017, 29, 1701822.
- [15] J. B. Lee, V. Subramanian, presented at Electron Devices Meeting, 2003. IEDM'03 Technical Digest. IEEE International 2003.
- [16] M. Maccioni, E. Orgiu, P. Cosseddu, S. Locci, A. Bonfiglio, *Appl. Phys. Lett.* 2006, 89, 143515.
- [17] M. Stoppa, A. Chiolerio, *Sensors* 2014, 14.
- [18] K. Cherenack, L. van Pieterse, *J. Appl. Phys.* 2012, 112, 091301.
- [19] N. Münzenrieder, C. Vogt, L. Petti, A. G. Salvatore, G. Cantarella, L. Büthe, G. Tröster, *Technol.* 2017, 5.
- [20] M. J. Panzer, C. D. Frisbie, *J. Am. Chem. Soc.* 2007, 129, 6599.
- [21] K. H. Lee, M. S. Kang, S. Zhang, Y. Gu, T. P. Lodge, C. D. Frisbie, *Adv. Mater.* 2012, 24, 4457.
- [22] M. Hamed, L. Herlogsson, X. Crispin, R. Marcilla, M. Berggren, O. Inganäs, *Adv. Mater.* 2009, 21, 573.
- [23] J. H. Cho, J. Lee, Y. Xia, B. Kim, Y. He, M. J. Renn, T. P. Lodge, C. D. Frisbie, *Nat. Mater.* 2008, 7, 900.
- [24] B. H. Kim, D. H. Lee, J. Y. Kim, D. O. Shin, H. Y. Jeong, S. Hong, J. M. Yun, C. M. Koo, H. Lee, S. O. Kim, *Adv. Mater.* 2011, 23, 5618.
- [25] J. A. Lim, F. Liu, S. Ferdous, M. Muthukumar, A. L. Briseno, *Mater. Today* 2010, 13, 14.
- [26] K. Tremel, S. Ludwigs, in *P3HT Revisited – From Molecular Scale to Solar Cell Devices*, DOI: 10.1007/12_2014_288 (Ed: S. Ludwigs), Springer Berlin Heidelberg, Berlin, Heidelberg 2014, p. 39.

- [27] J. A. Lim, J. H. Kim, L. Qiu, W. H. Lee, H. S. Lee, D. Kwak, K. Cho, *Adv. Funct. Mater.* 2010, 20, 3292.
- [28] G. Zhang, H. Liao, M. Cherigui, J. Paulo Davim, C. Coddet, *Eur. Polym. J.* 2007, 43, 1077.
- [29] F. J. B. Calleja, J. M. Salazar, H. Čačković, J. Loboda-Čačković, *J. Mater. Sci.* 1981, 16, 739.
- [30] J. Liu, M. Arif, J. Zou, S. I. Khondaker, L. Zhai, *Macromolecules* 2009, 42, 9390.
- [31] M. Chang, J. Lee, N. Kleinhenz, B. Fu, E. Reichmanis, *Adv. Funct. Mater.* 2014, 24, 4457.
- [32] Y. D. Park, H. S. Lee, Y. J. Choi, D. Kwak, J. H. Cho, S. Lee, K. Cho, *Adv. Funct. Mater.* 2009, 19, 1200.
- [33] D. Choi, M. Chang, E. Reichmanis, *Adv. Funct. Mater.* 2015, 25, 920.
- [34] D. H. Kim, Y. D. Park, Y. Jang, S. Kim, K. Cho, *Macromol. Rapid Commun.* 2005, 26, 834.
- [35] M. Lee, H. Jeon, M. Jang, H. Yang, *ACS Appl. Mater. Interfaces* 2016, 8, 4819.
- [36] Y.-K. Lan, C.-I. Huang, *J. Phys. Chem. B* **2009**, 113, 14555.

- [37] H. Sirringhaus, P. J. Brown, R. H. Friend, M. M. Nielsen, K. Bechgaard, B. M. W. Langeveld-Voss, A. J. H. Spiering, R. A. J. Janssen, E. W. Meijer, P. Herwig, D. M. de Leeuw, *Nature* **1999**, 401, 685.
- [38] H. Wang, Y. Xu, X. Yu, R. Xing, J. Liu, Y. Han, *Polym.* **2013**, 5.
- [39] B. O'Connor, E. P. Chan, C. Chan, B. R. Conrad, L. J. Richter, R. J. Kline, M. Heeney, I. McCulloch, C. L. Soles, D. M. DeLongchamp, *ACS Nano* **2010**, 4, 7538.
- [40] S.J. Kim, H. Kim, J. Ahn, D.K. Hwang, H. Ju, M.-C. Park, H. Yang, S. H. Kim, H. W. Jang, J. A. Lim, *Adv. Mater.* **2019**, 31, 1900564.

Chapter 3

**Fiber-Shaped Multi-Synapses Implementable
Organic Electrochemical Transistor for
Neuromorphic device**

3.1 Introduction

As requirement of big data and artificial intelligence increases, neuromorphic computing enable to process massively parallel information has gathered a great deal of interest as the most promising breakthrough for overcoming the limitation of the current von Neumann architecture.^[1] For realization of neuromorphic device, one of the keys is the function to reliably emulate synaptic plasticity, which signifies memorizing and regulating the amplitude or strength (i.e., synaptic weight) of synapses existed between two neurons. In biology, synaptic weight corresponds to the factor that influences the signal firing of one neuron to another neuron.^[2] According to biological mechanism of the synaptic transmission, the general understanding is that signaling between the neurons is associated to the migration of the ions at the end of the cell through electrolyte medium and the changes of membrane potential in the neuron cell.^[3] For instance, when the action potential attains axon terminal then induces depolarization of the membrane, calcium ion (Ca^{2+}) channel controlled by voltage is activated in the cell membrane and influx of the Ca^{2+} makes synaptic vesicles to release neurotransmitter molecules at the end of the presynaptic neuron called dendritic, as shown in **Figure 27**. The neurotransmitters from presynaptic neuron bind the receptors on the postsynaptic then they newly induce the localized membrane potential. In this postsynaptic

neuron, the continuous changes of the potential driven at different timings or synapses are integrated in an inhibitory or excitatory manner and lead to determine whether neuron emits an action potential (i.e., fire). Structurally consists of neurons, cell bodies, dendrites and long slender axons are in the form of a fibrous appearance with many branches. In several channels called synapses between end of the dendrites and next neurons, synaptic communication occurs. Given the biological mechanisms of synaptic communication and fibriform dendrites of a neuron, a neuromorphic device should possess the synaptic-weight controllability for multichannel communications and functionality of a neuron for spatiotemporal signal summation.'

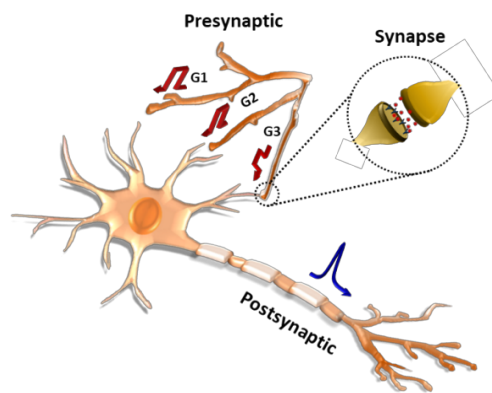


Figure 27 . Schematic of biological synapse(inset), presynaptic neuron and postsynaptic neuron.

As the most promising platform for neuromorphic device that best emulates biological synaptic plasticity induced by a voltage-gated ionic channel, recently, organic electrochemical transistors (OECTs) based on electrochemical interactions of ions in an insulator and conjugated polymer as a semiconductor have gathered remarkable attention.^[1] The intrinsic advantages of OECT devices including excellent tunability, good biocompatibility, simple implementation of multiple channels, low power consumption and low-cost fabrication are irresistibly merits for neuromorphic applications.^[1, 4-6] Depending on the strength of a pulsed gate bias, the active channel conductance as synaptic weight function can be modulated. In accordance of the gate-bias pulses which mimic the presynaptic stimulations, an electrical double layer (EDL) is formed at the interface of the conjugated polymer/iongel insulating layer or ions penetrate into the conjugated polymer as an active channel. The occurred phenomenon lead to the drain-current characteristics to persist differently for short- or long-periods of time.^[4, 7] Based on this principle, several research groups have reported various neuromorphic OECT devices with synaptic functionalities such as short- or long-term plasticity including excitatory postsynaptic current (EPSC), inhibitory postsynaptic current (IPSC) and paired-pulse facilitation (PPF).^[8-15] Basic circuit simulations using synaptic functions of OECTs such as Pavlov associative and handwritten(MNIST) classification for

learning have demonstrated OECT used as a neuromorphic devices and showed preliminary feasibility.^[12, 16] Although such neuromorphic devices based on OECTs have been already developed considerably, the mechanism of electrochemical doping between conjugated polymer and ions in an OECT. How ionic species interact with the conjugated polymer at polymer/electrolyte interfaces under gate-bias pulse as synaptic functional conditions is not fully understood. To further improve the performance of the OECT as a neuromorphic device, identifying this mechanism is essential.

For realizing application of neuromorphic OECT to artificial intelligence (AI) technologies such as machine learning, one of the most important keys is the cyclability of the devices which means the ability of the devices showing reliable performance under extensive and numerous repetitive write–read–erase–read (W–R–E–R) cycles. In general, learning process based on a spiking neural network (SNN) following a Hebbian rule requires the repetitive correction of the synaptic weights depending on the incoming stimuli. The conductance of the synaptic device corresponding to synaptic weight should be repeatedly and reliably increased or decreased for the correction of synaptic weight.^[17] As an example, the synaptic weight (W_{ij}) is typically determined by $W_{ij}=(g_{ij}-g_{min})/(g_{max}-g_{min})$, where g_{max} and g_{min} are the maximal and the minimal conductance states of the device and g_{ij} is the conductance of the device between the i_{th} and j_{th} neurons, respectively.

During the learning process, the relative change of the synaptic weight is iteratively updated and calculated. When the programmed and/or erased conductance states vary under every repeated cycle, change of each conductance levels at every operation, g_{ij} , is induced. Additionally, the memory window, $g_{\max} - g_{\min}$, is also fluctuating, leading to a distorted normalization factor. Therefore, the difference of synaptic weight, ΔW , from the previous state is inevitably incorrectly updated. Eventually, the deterioration of the learning itself through updating the synaptic weight is disabled by unreliable updating. However, cyclic endurance of neuromorphic OECT devices, which is an essential element for learning based on stable updates, has been rarely studied. Only a few studies have reported the cycling properties of organic neuromorphic devices.^[7,9]

Here, I suggest dendritic network implementable fiber-shaped neuromorphic OECTs with improved cyclic endurance for spatiotemporal iterative learning.^[44] As a new approach to the architecture of neuromorphic devices that imitates nerve fiber structure, a fibriform OECT consist of a double-stranded assembly of electrode microfibers (DSA-microfibers) with an iongel insulator, called a neurofiber-OECT, is demonstrated. The suggested neurofiber-OECT easily implements the dendritic network via simple and physical contact of the microfibers as a gate-electrode on the DSA-microfiber construction and exhibits a higher output current for responding gate-bias stimuli compared to that of the

planar devices. From the technological point of view, it is worth to point out that fiber electronic device is a key component due to free deformation and integration to smart wearable devices such as electronic textiles.^[18,19] For further improvement in future wearable technologies capable of computing and learning like human senses such as robotic application, fiber-shaped textile neuromorphic devices could be required and developed.^[20,21]

In the previous work, carboxylic acid-functionalized polythiophene-poly[(3-(6-carboxyhexyl)thiophene)-2,5-diyl] (P3CT) is particularly suggested for neuromorphic devices based on OECTs to enhance cyclic endurance characteristics and memory retention. Unlike poly(3-hexylthiophene) (P3HT), which has been commonly used as a conjugated polymeric semiconductor for neuromorphic OECTs that show unstable cyclic endurance and a short retention time under repeatedly applied potentiation and depression processes, the neurofiber-OECT composed of P3CT exhibits highly reliable cycling stability. Based on fundamental studies of the electrochemical interaction between the P3CT and ionic species under cycling processes, it was found that the balanced state of charge involving the carboxylic acid group in the side chain of P3CT facilitates the reversible redox reactions in the P3CT as an active channel, resulting in the stable and reliable long-term potentiation (LTP) and long-term depression (LTD) cyclic characteristics of the device. Compared to neurofiber-OECT based on P3CT, the doped state of

P3HT-neurofiber cannot be reversibly returned to the initial state due to the existed anions that penetrated into the film, which induce the unstable retention and cyclic endurance of the device based on P3HT. Eventually, a neurofiber-OECT device based on P3CT executing a dendritic network with numerous gates as presynaptic neurons and one drain as a postsynaptic neuron implement the unit neural network to be composed more effectively for complicated computation based on the successful imitation of synaptic behavior and leaky integrate-and-fire behavior. As a proof of concept, I confirmed that the neurofiber based on P3CT device with enhanced cyclic endurance can be successfully used to speech recognition of the TI-46 speech corpus,^[22] with a significant recognition accuracy of 88.9%, through tempotron based on iterative SNN learning.^[23]

3.2 Experimental Method

Materials: Gold microfibers with a 0.1 mm diameter (purity 99.95%) were purchased from Alfa Aesar. Poly(vinylidene fluoride-co-hexafluoropropylene), P(VDF-HFP) with $M_n = 130 \text{ kg mol}^{-1}$ and $M_w = 400 \text{ kg mol}^{-1}$, [EMIM][TFSI], silver trifluoromethanesulfonate (AgTf), 1-butyl-1-methyl-pyrrolidinium bis(trifluoromethanesulfonyl)imide (P_{14} TFSI), ferrocene, dopamine hydrochloride, chlorobenzene, and N,N-dimethylformamide (DMF) were purchased from Sigma-Aldrich. P3HT (91–94% regioregularity, M_w 50-70 kg mol^{-1} , 4002-EE), and P3CT

(82–94% regioregularity, Mw 50-60 kg mol⁻¹, 4033) were purchased from Rieke Metals.

Device fabrication: P3HT and P3CT solutions were prepared by dissolving P3HT in chlorobenzene and P3CT in DMF with a concentration of 100 mg/mL. After Au microfibers were treated in a dopamine (2 mg of dopamine per mL of 10 mM tris-HCl) aqueous tris-HCl buffer solution (pH = 8.5) for 1 h. P3HT and P3CT semiconductor thin films with a thickness of 1 μm were homogeneously coated onto polydopamine (pDA) treated Au microfibers (diameter: 100 μm) by a die-coating method. The P3HT- and P3CT-coated electrodes were dried in a vacuum oven at 70 °C overnight. To form a channel in the OEET based on a double-strand assembly of electrode microfibers, two semiconductor-coated electrodes were fixed onto two parallel slide glasses that were then rotate one side of the slide glass. The mixed solution of P(VDF-HFP) and [EMIM][TFSI] dissolved in acetone at a weight ratio of 1:4:8 for the iongel was vertically dropped along the double-stranded assembled microfibers. After the iongel was coated, the Au microfibers (100 μm) as multiple gates were wound over the iongel layer.

Characterization: The electrical properties of the neurofiber-OEETs were determined using an Agilent 4156C semiconductor device analyzer under ambient conditions. To determine the thickness of the P3HT and P3CT films, scanning

electron microscopy (SEM) with focused ion beam (FIB) milling (Helios NanoLab 600) was used to acquire cross-sectional images of the films. Cyclic voltammetry (CV) was performed on a VersaSTAT 3 potentiostat (Ametek). Cyclic voltammograms of P3HT and P3CT films deposited on Au electrode in [EMIM][TFSI] ionic liquid were recorded using [10 mM silver trifluoromethanesulfonate (AgTf), 1-butyl-1-methyl-pyrrolidinium bis(trifluoromethanesulfonyl)imide (P₁₄TFSI)] and Pt as a reference and counter electrode, respectively. The relative energy level of the reference electrode was corrected by valuating the voltammetric responses for 5 mM ferrocene in [EMIM][TFSI]. The 1 μm-thick P3HT and P3CT films for FT-IR analysis were fabricated by spin-casting of the P3HT and P3CT solutions on the Au substrate. The electrochemical doping and de-doping process of P3HT and P3CT films in [EMIM][TFSI] ionic liquid were performed by using cyclic voltammetry setup. Then, the doped and de-doped films were analyzed by the ATR-IR (Spectrum 100, PerkinElmer) with detection region from 450-4000 cm⁻¹ and resolution of 4 cm⁻¹. Raman spectra (In Via Raman Microscope, Renishaw) was recorded with 785 nm excitation wavelength. XPS (Nexsa, Thermofisher Scientific) was carried out with microfocus monochromatic X-ray source (Al-K_α at 1486.6 eV). AFM (Multimode 8, Bruker) measurements were performed on the P3HT and P3CT films with a thickness of 1 μm. The 2D-GIXRD measurements were performed at the PAL-6D

beamline at the Pohang Accelerator Laboratory. The X-ray beam ($\lambda = 1.0721$ nm) was incident at a grazing angle 0.10° for 120 s.

3.3 Results and Discussion

Figure 28 shows the architecture of the neurofiber-OECT device composed of DSA-microfibers. In previous work, I reported the performance and characteristics of the fiber-shaped organic transistor based on the double-stranded assembled microfibers. This device showed a high output current at low operational bias via utilization of an iongel as a gate insulator with high capacitance and a short length of channel.^[24] It was also shown that the electrical performance of the transistor based on DSA-microfibers was almost retained even after weaving devices into the textile and repeated bending deformation. **Figure 29** describes a holistic process and a detailed fabrication of the neurofiber-OECT. This construction facilitates implementations of multiple synaptic junctions via simple physical contact of microfibers as gate-electrodes, similar to the dendrite architecture of biological neurons, on the surface of the coated iongel without additional interconnect junctions. The cross-sectional illustration of the neurofiber-OECT is shown in **Figure 28**. As a general, applying negative bias to the gate electrode of the neurofiber-OECT induces electrochemical doping at the source electrode through interaction between of polythiophene and the bis(trifluoromethane)sulfonimide

(TFSI) anions in the iongel; the generated charge carriers in the active channel based on thiophene can be transported to the drain electrode or trapped depending on the applied electric-field conditions.^[4] Molecular structures of the main components (P3HT, P3CT, (TFSI) anion and 1-ethyl-3-methylimidazolium (EMIM) cation) are shown in **Figure 30**. The neurofiber-OECT devices based on P3HT and P3CT are hereafter referred to as P3HT-neurofiber and P3CT-neurofiber devices, respectively.

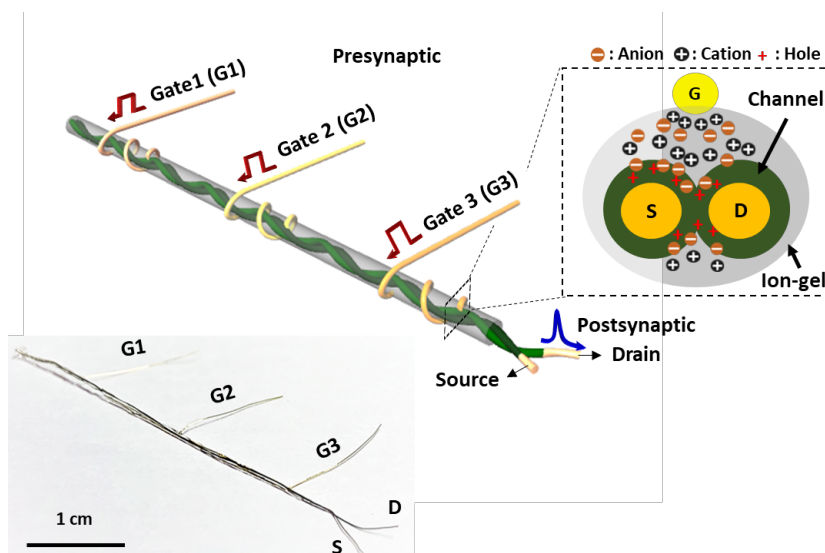


Figure 28. Schematic of the device structure for neurofiber-OECT and the doping interaction in channel by ions (inset) and photograph of OECT-neurofiber.

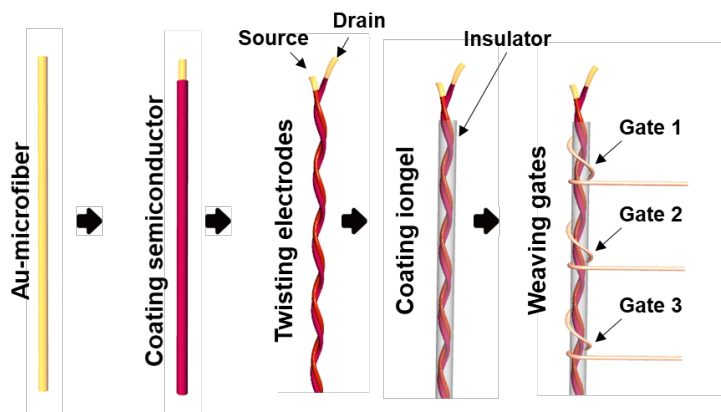


Figure 29. Schematics of fabrication of neurofiber-OECT.

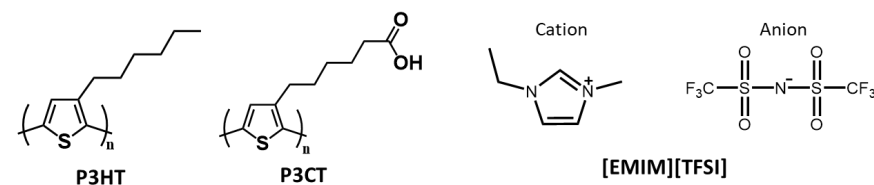


Figure 30 . Molecular structures of poly(3-hexylthiophene-2,5-diyl) (P3HT), poly[3-(6-carboxyhexyl)thiophene-2,5-diyl] (P3CT) and 1-ethyl-3-methylimidazolium bis(trifluoromethylsulfonyl)imide ([EMIM][TFSI]).

Compared to typical planar P3HT-OECT device, the P3HT-neurofiber device shows a 1.94-fold greater postsynaptic current under the same presynaptic gate pulse (-0.7 V, 100 ms) with the same channel length ($2\ \mu\text{m}$) and channel width (1 cm), as shown in **Figure 31**. The enlarged active channel of the P3HT-neurofiber

which can interact with the ions from iongel might induce this greater current. As shown in **Figure 32**, an electrochemical interaction between ions and active channel at both sides of the neurofiber-OECTs can be occurred by easy migration of the ion species under the applied electric field. This possibility intimates that the geometry of the device based on DSA-microfibers may forward an enhanced signal-to-noise ratio of the neuromorphic device for such weak stimulus from presynaptic.

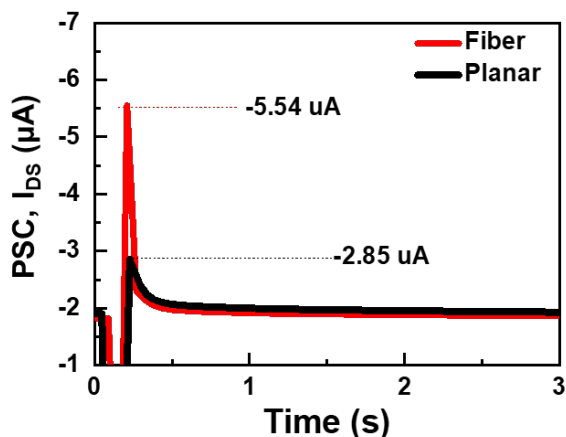


Figure 31. Comparison of postsynaptic current between the planer P3HT-OECTs and P3HT-neurofiber with a length (L) of $2 \mu m$ and a width (W) of $1cm$ when the gate-bias was applied ($V_{GS} = -0.7 V, 100 ms$)

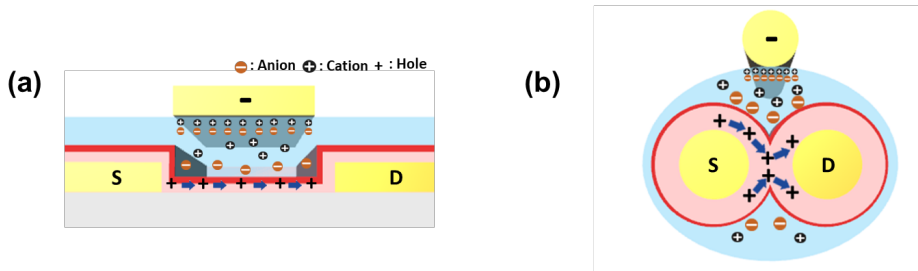


Figure 32. Schematics of channel dimension of a (a) planar device and (b) neurofiber-OECTs.

Figure 33a shows the transfer curves (I_{DS} - V_{GS}) of the P3HT-neurofiber device under a repeated sweep of gate-bias (V_{GS}). The range of sweep V_{GS} was gradually increased from (+1.8 to -0.7 V) to (+1.8 to -1.8 V) while six repeated forward/reverse cycles were proceeded. Applying more negative V_{GS} leads to an increased ON-state drain current (I_{on}) and a magnification of the current ratio, implying that the P3HT-neurofiber OECT has gate-field-dependent memory properties. When applying the negative V_{GS} was below -0.7 V, bi-stable current state was not confirmed. At applied V_{GS} biases more negative than -1.0 V, a current ratio associated with I_{on}/I_{off} current ratio greater than 10^1 started to appear then, at the $V_{GS} = -1.5$ V, the maximum value of $\sim 10^2$ was observed. This phenomenon implies that transition between the short-term plasticity and long-term plasticity properties can be induced by changing the applied gate bias. In fact, **Figure 33b** indicates the change of the synaptic plasticity between short-term and

long-term memory depending on presynaptic V_{GS} bias. This result is similar with the previously demonstrated planar OECT based on P3HT as neuromorphic devices.^[16] Especially, an increase of the OFF-current (I_{off}) state under repeat operating cycles was unexpectedly shown. During cyclic operation, this increase of I_{off} was also confirmed in the conventional planar P3HT-OECT devices (**Figure 34**), which implies that this behavior is not associated to the architecture of neurofiber-OECT device.^[25] Consequently, the OECT device based on P3HT shows unstable cyclic endurance. Also, the long-term potentiation state of the device did not recover to its initial state. **Figure 35a** shows the endurance of the P3HT-neurofiber device for 50 repeated W–R–E–R switching cycles. In fact, the programmed ON-state current was degraded by more than 55% from the initial current and the erased OFF current level gradually increased, leading to substantial degradation of the I_{on}/I_{off} memory ratio after 50 operation cycles. The retention graph of the P3HT-neurofiber, as presented in **Figure 35b**, also shows a 3.6-fold increase in the OFF-state current during the initial 250 s, even applying the intense erasing pulse of $V_{GS} = +2.5$ V, which is the maximum voltage enabled to apply without electrochemical degradation of the EMIM and TFSI ions (**Figure 36**).^[26] A possible mechanism that induce this unstable cyclic endurance of the P3HT devices will be discussed later.

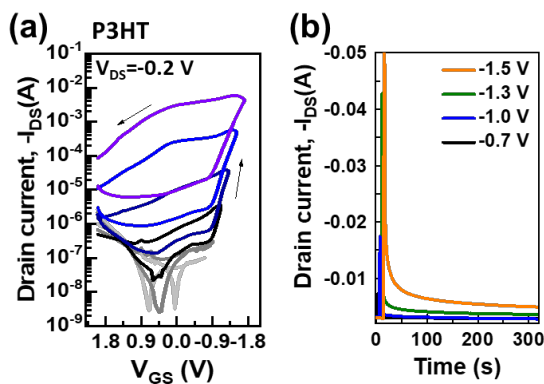


Figure 33. (a) Transfer graph of P3HT-neurofiber at $V_{DS} = -0.2$ V. (b) Drain current as postsynaptic current (PSC) induced by various V_{GS} from -0.7 V to -1.5 V as a presynaptic stimulation in P3HT-neurofiber.

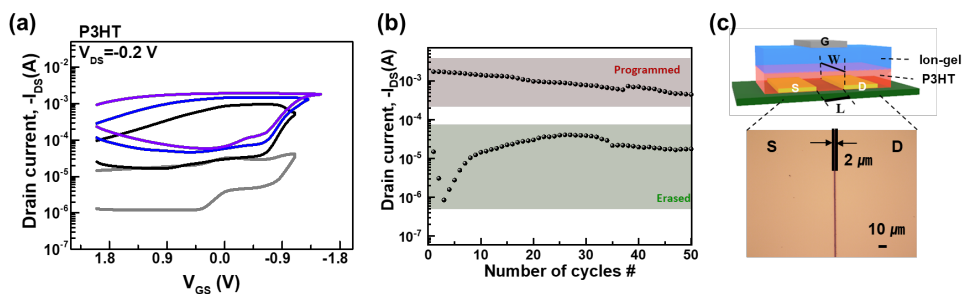


Figure 34. (a) Transfer curves at $V_{DS} = -0.2$ V and (b) 50 W-R-E-R cycles of planar P3HT-OECT using $V_{GS} = -1.5$ V, 10 s duration for programmed pulse and $V_{GS} = 1.5$ V, 5 s duration for the erased pulse. After applying each pulses, drain

current (I_{DS}) was recorded at $V_{GS} = 2$ mV with 2 s intervals. (c) Illustration of the planar OECT and optical microscope image of the channel dimension of the device.

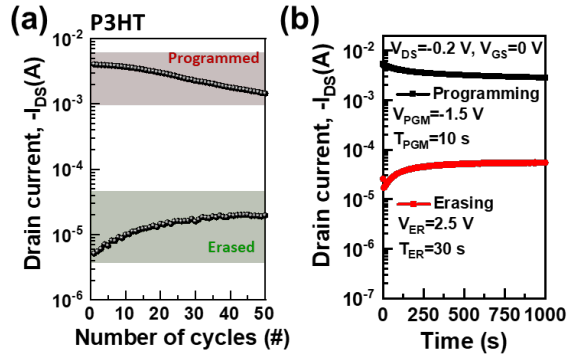


Figure 35. (a) 50 W-R-E-R cycles of P3HT-neurofiber by using $V_{GS} = -1.5$ V with 10 s duration for the programming pulse (V_{PGM} and T_{PGM}) and $V_{GS} = 1.8$ V with 5 s duration for the erasing pulse (V_{ER} and T_{ER}). After applying pulses for programming or erasing, drain current was recorded under $V_{GS} = 2$ mV with 2 s intervals. (b) Retention characteristics of the P3HT-neurofiber.

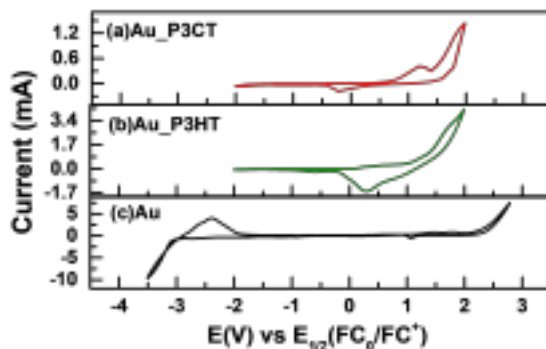


Figure 36 . Cyclic voltammetry curves of (a) P3CT and (b) P3HT in [EMIM][TFSI], as recorded with a scan rate of 50 mV/s. (c) Cyclic voltammogram to confirm the electrochemical window of [EMIM][TFSI].

In particular, the P3CT-neurofiber showed stable memory characteristics depending on gate-field during repeated cyclic operation with a progressively increasing V_{GS} . **Figure 37a** shows the I_{on} gradually increased until reaching at maximum negative V_{GS} bias, however, the output current value recovered to the initial I_{off} state at $V_{GS} = 0$ V under six repeated cycle sweeps. The P3CT-neurofiber showed a 10 times larger current ratio than that of the P3HT-neurofiber. The P3CT-neurofiber also, like the P3HT-neurofiber, showed the transition from short-term to long-term synaptic plasticity depending on gate-bias (**Figure 37b**). Compared to the cyclability of the P3HT-neurofiber, that of the P3CT-neurofiber

was improved as shown in **Figure 38a**. Even after 50 W–R–E–R repeated operations, the programmed ON- and erased OFF-state currents were retained. **Figure 38b** clearly shows the bistable conductivity of the P3CT-neurofiber device with a 10^3 current ratio much more stably compared to the P3HT-neurofiber device. In addition, **Figure 39a** and **Figure 39b** show the multilevel retention induced by different 5 programming voltages with the same duration or by varying the number of the programming pulses at the same programming voltage bias, respectively. These results obviously indicate that the P3CT functionalized with carboxylic acid groups resulted in a significant improvement in the cyclic characteristics of the neuromorphic OECT devices.

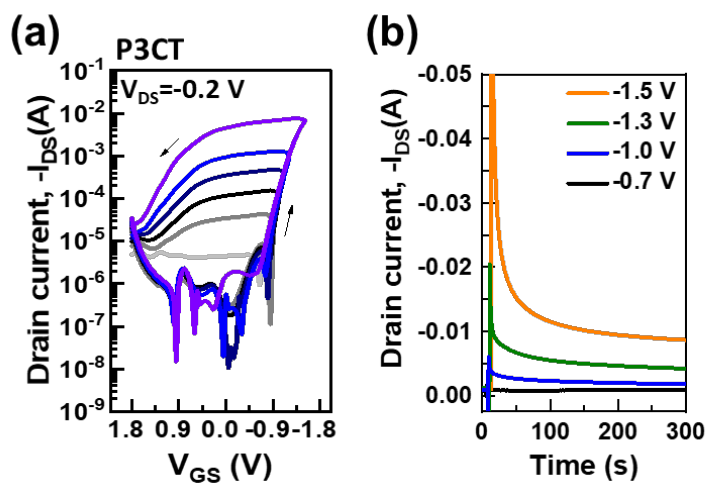


Figure 37. (a) Transfer graph of P3CT-neurofiber at $V_{DS} = -0.2$ V. (b) Drain current as postsynaptic current induced by various V_{GS} from -0.7 V to -1.5 V as a presynaptic stimulation in P3CT-neurofiber.

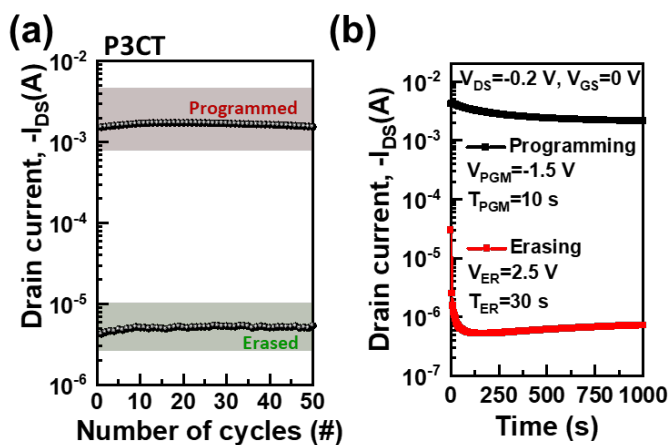


Figure 38. (a) 50 W-R-E-R cycles of P3CT-neurofiber by using $V_{GS} = -1.5$ V with 10 s duration for the programming pulse (V_{PGM} and T_{PGM}) and $V_{GS} = 1.8$ V with 5 s duration for the erasing pulse (V_{ER} and T_{ER}). After applying pulses for programming or erasing, drain current was recorded under $V_{GS} = 2$ mV with 2 s intervals. (b) Retention characteristics of the P3HT-neurofiber.

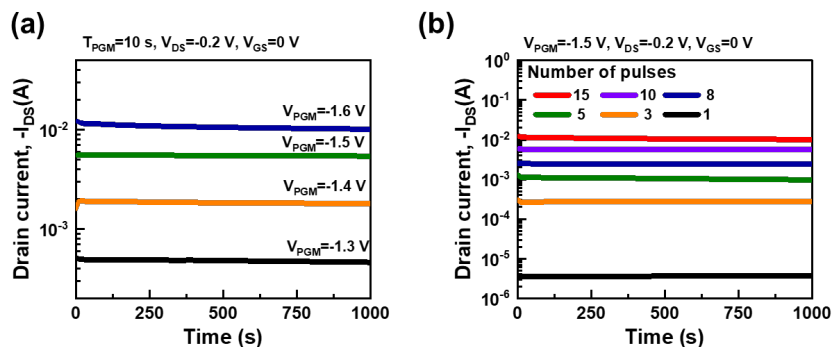


Figure 39. Retention characteristics of P3CT-neurofibers under (a) different programmed voltages with constant duration or (b) various number of pulses at the same programmed voltage. After applying each pulses, drain current was recorded at $V_{DS} = -0.2$ V and $V_{GS} = 0$ mV with 5 s intervals.

To investigate the origin of this distinct behavior under the cycling test for the P3HT- and P3CT-OECT devices, firstly, the electrochemical processes for doping and dedoping the P3HT with [EMIM][TFSI] ions under an electric field were investigated. **Figure 40** presents a cyclic voltammetry curves of the P3HT film in [EMIM][TFSI] ionic liquid under repeated condition leading to oxidation and reduction.^[27] At 0.3 and 0.6 V in the first cycle, oxidation peaks of P3HT are observed due to the formation of positive charges at the polythiophene chains by elimination of the electrons.^[28] It is noted that the oxidation peak at 0.38 V distinctively increased in the second and third scan cycles (**Figure 40**, inset). This

result indicates that, due to a left certain amount of positive charges even after the reduction process at the first cycle, more positive charges were generated in the P3HT film during the continuous second oxidation cycle.

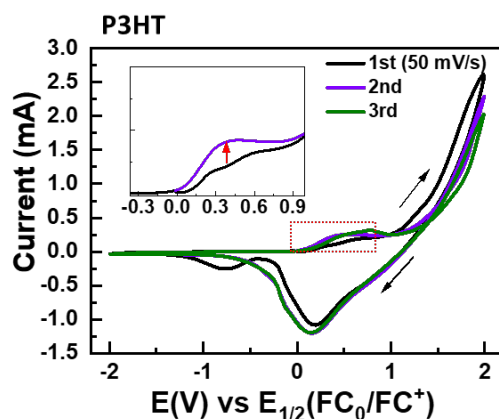


Figure 40. Cyclic voltammetry curves of P3HT in [EMIM][TFSI] ionic liquid at 50 mV/s.

With the P3HT films which electrochemical state controlled by cyclic voltammetry, molecular interactions between P3HT and [EMIM][TFSI] ions were investigated by Raman analysis and Fourier transform infrared (FT-IR). The doped and dedoped state of P3HT depending to the conditions for oxidation and reduction was observed by Raman spectroscopic analysis (**Figure 41**). Two characteristic

peak at 1446 and 1380 cm^{-1} associated with the $\text{C}_\alpha=\text{C}_\beta$ ring stretching in thiophene ring and the $\text{C}_\beta-\text{C}_\beta$ ring stretching, respectively, were observed in the spectrum of the pristine P3HT film. When the formation of polaron is generated at the P3HT backbone, it is found that the band at 1408 cm^{-1} attributed to a symmetric stretching of the C=C bond ring (Q_1) appears and also the shifted band from 728 cm^{-1} (Q_2) indicating structural change of C-S-C deformation is observed. After oxidation process, the changes of Q_1 and Q_2 polaronic bands were confirmed (red line), indicating the generation of polarons in the oxidized P3HT. In particular, the existence of polarons, which induces the Q_1 polaronic peak and low-shifted Q_2 band (722 cm^{-1}) in the spectrum, was still identified in the reduced P3HT film (green line). This result indicates that the positive polarons in the P3HT film still remain even after the reduction process.

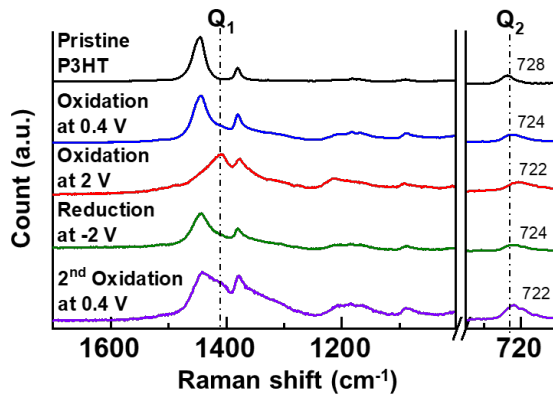


Figure 41. Raman spectra of P3HT upon condition for oxidation and reduction during cyclic voltammetric cycles.

In FT-IR spectra of P3HT, the band at 821 cm^{-1} attributed to C–H out-of-plane bending in the thiophene ring was shifted to 881 cm^{-1} after oxidation process at 2.0 V (**Figure 42c**). This result is due to the increase of C–H bonding in the thiophene ring by the deficiency of electrons, which is associated with the formation of positive polarons in the backbone of polythiophene under the oxidation potential.^[29] Additionally, the characteristic peaks of TFSI anions in the FT-IR spectrum of the oxidized P3HT film were investigated (**Figure 42b**). These peaks are clear evidence that the TFSI anions penetrated into the P3HT film during the oxidation process. The band attributed to stretching vibrations of the S–N–S and SO_2 bonds

in TFSI anions markedly shifted from 1063 and 1143 cm^{-1} to 1017 and 1115 cm^{-1} , respectively, after the oxidation process. These shifts indicate weakening bond and stabilized stretching vibration by counter charges.^[30, 31] In addition, two split peaks for SO_2 at 1112 and 1136 cm^{-1} corresponding to the transoid structure of TFSI newly observed in the spectrum of the oxidized P3HT film (**Figure 43**). This conversion of TFSI anion to transoid structure might be induced in order to efficiently interact with the counter ions with its negatively charged N atom exposed under low steric hindrance. This can be the evidence that TFSI anions are stabilized by positively charged species. Since no characteristic peaks for EMIM cations were observed in the oxidized P3HT film by the FT-IR measurement, it is found that the EMIM cations did not penetrate into the P3HT under the oxidation process (**Figure 42a**). Based on these results, it is reasonably conclude that the TFSI anions stabilize the polarons formed in the oxidized P3HT. These analyses indicate that the programmed P3HT-neurofiber with high conductivity is led by this stabilization of the generated polarons by penetrated TFSI anions in the oxidized P3HT film.

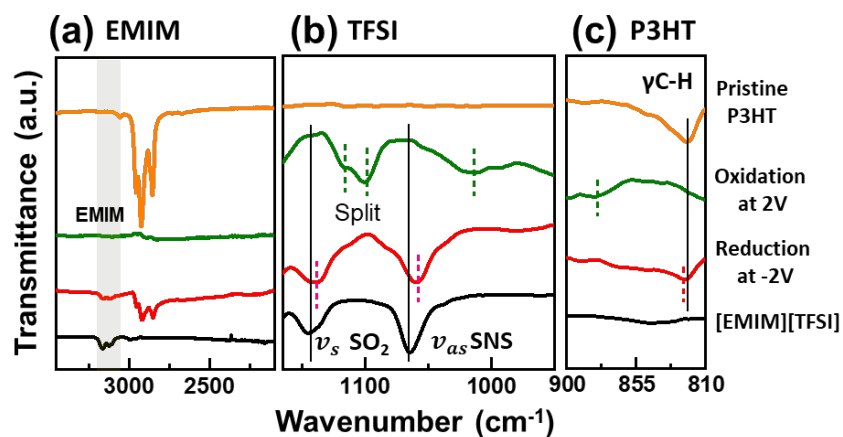


Figure 42. Changes in the FT-IR spectra of P3HT films and [EMIM][TFSI] ions under doping and dedoping process.

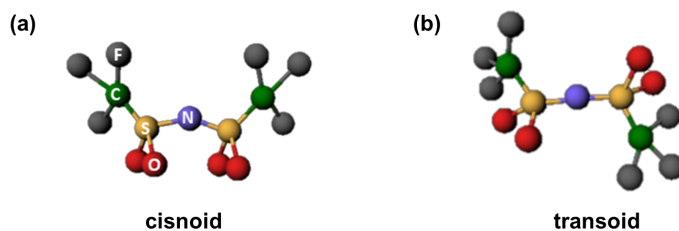


Figure 43. The structures of TFSI with (a) cisoid and (b) transoid.

To understand the dedoped P3HT after reduction process, the reduced P3HT was obtained by applying reduction potential of -2.0 V. In FT-IR spectra of the dedoped P3HT film, the bands of the P3HT and TFSI anions did not completely recover to their initial positions (**Figure 42b**). In the spectrum in **Figure 42c**, the bending vibration band of C–H in the thiophene ring of P3HT showed a slightly higher wavenumber than its original position. In addition, the stretching peaks of the S–N–S and SO₂ in the TFSI anions appeared at lower wavenumbers than their initial bands. These results clearly imply that, even after applying a strong reduction bias, a certain amount of TFSI anions, which penetrated into the P3HT film under oxidation bias, remained in the P3HT film and still interacted with the polarons generated in the P3HT backbone. In conclusion, P3HT film as an active channel can be easily doped and it induces generation of polarons, which can be stabilized by the penetrated TFSI anions under an applied oxidation potential. Since TFSI anions were left in the dedoped film even after applying reduction bias, however, the doped P3HT did not return to its initial neutral state, which eventually deteriorated the retention and cyclic endurance characteristics of the P3HT-based OECT neuromorphic devices shown in **Figure 35**. **Figure 44** shows a schematic to summarize the possible molecular interactions of the P3HT and the TFSI ions as well as the expected charge distribution in the P3HT-OECT device depending on the redox process.

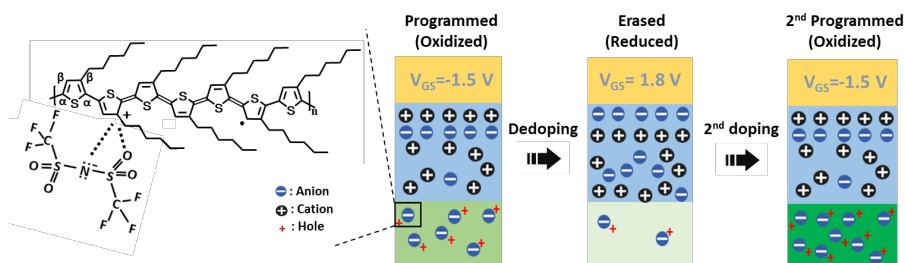


Figure 44. Illustration of the interaction between P3HT and [TFSI][EMIM] under electrochemical doping and dedoping process.

Compared to P3HT, P3CT showed different behavior of electrochemical redox reaction. Figure 45 presents the cyclic voltammograms of P3CT upon repeated oxidation and reduction cycles. In particular, 0,69 V of the oxidation peak under the first redox cycle shifted to -0.23 V at the second redox process and no further changes were observed after secondary oxidation (**Figure 45**, inset). These results imply that the lower oxidation potential of P3CT was induced by a structural change of the P3CT after the first redox cycle.

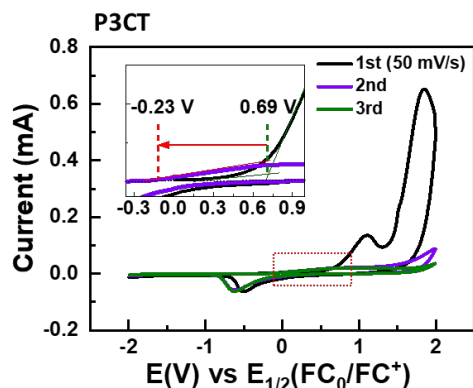


Figure 45. Cyclic voltammetry curves of P3CT in [EMIM][TFSI] ionic liquid at 50 mV/s.

As shown in **Figure 46**, the changes in the chemical structures of P3CT and [EMIM][TFSI] ions upon redox cycles were investigated by FT-IR analysis. In a general spectrum of pristine P3CT, two bands are shown at 936 and 1700 cm^{-1} , which indicate the C–O and C=O bonds in carboxylic acid groups, respectively. After first oxidation process of P3CT film, the C–O peak shifted to a higher wavenumber (954 cm^{-1}), while the C=O peak shifted to a lower wavenumber (1694 cm^{-1}) (**Figure 46a** and **Figure 46b**). These results are based on the formation of the resonance coupling between C–O single bonds and C=O double bonds, which indicates that carboxylic acid (COOH) groups were changed to carboxylate (COO^-) groups.^[32] In addition, (i) reduced absorption of broad band at the 3500–2500 cm^{-1}

attributed to hydrogen bonding of the dimer and the O–H stretching ^[33] and (ii) appearance of absorption at 1300 cm⁻¹ and 1398 cm⁻¹ corresponding to COO⁻ group in FT-IR spectra^[34] as well as (iii) X-ray photoelectron spectroscopy analysis support that the hydrogen was removed from carboxylic acid groups in the oxidized P3CT (**Figure 47** and **Figure 48**). This phenomenon is consistent with previous report, which shows that the deprotonation in carboxylic acid groups leading to a charge balance with the polarons under an oxidation condition, resulting in long-term memory state.^[35] After applying the reduction bias to this first oxidized P3CT film, the change in absorption of the C=O band (944 cm⁻¹) and the C–O band (1697 cm⁻¹) was still observed when compared with their initial absorption values in the spectrum of pristine P3CT. This implies that a certain amount of protons and carboxylate anions remained after the first redox reaction was finished completely. The functional group in P3CT was changed from electron-withdrawing carboxylic acid (COOH) group to electron-donating carboxylate (COO⁻) group might improve the stability of the oxidized polythiophene backbone of P3CT, leading to a lower oxidation potential of P3CT after the first redox cycle. Additionally, the shifted absorption band from 821 to 841 cm⁻¹ corresponding to C–H out-of-plane bending in oxidized P3CT recovered to its initial band (821 cm⁻¹) after first redox cycle, as shown in **Figure 46c**. This result shows the different behavior that observed results in FT-IR spectra of the

P3HT, as mentioned previously (**Figure 42c**). This difference indicates that the positively charged polythiophene backbone in the P3CT after oxidation process can be fully returned to its initial state after reduction process. In fact, this result was identified by Raman spectroscopic measurement of the P3CT films under repeated redox cycles (**Figure 49**). This result also indicates that oxidized P3CT film, which identified by polaronic peak bands at Q_1 and Q_2 , fully returned to its initial state after the reduction process. This result clearly implies that the process for electrochemically doping and dedoping P3CT interacting with [EMIM][TFSI] ions is reversible, unlike irreversible process of doping and dedoping P3HT. Additionally, this reversible redox reaction of P3CT induce good cyclic characteristics of the P3CT-neurofiber device.

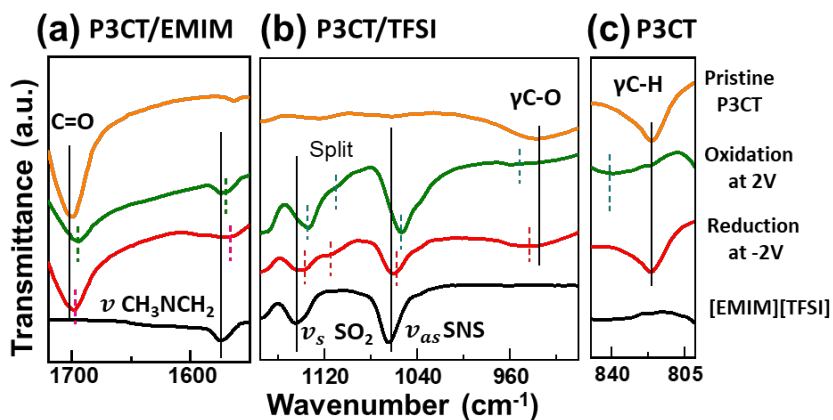


Figure 46. Changes in the FT-IR spectra of P3CT films and [EMIM][TFSI] ions under redox process.

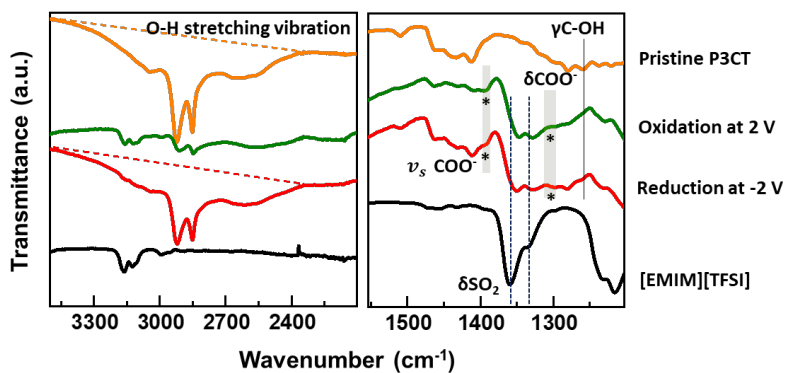


Figure 47. FT-IR spectra for analyzing to hydrogen bond in carboxylic acid of P3CT films after oxidation process.

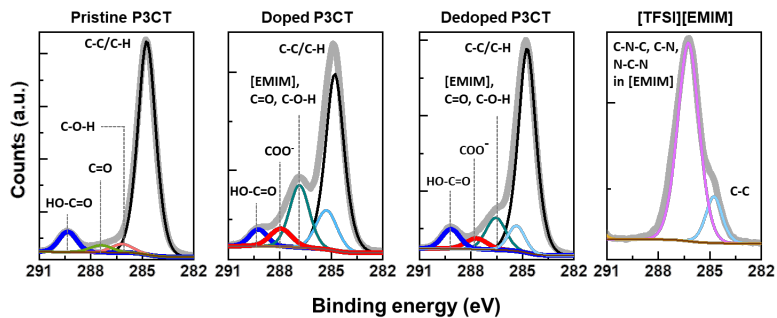


Figure 48. The C1s peaks in the X-ray photoelectron spectroscopy (XPS) spectra of the pristine P3CT, doped P3CT, dedoped P3CT films and [TFSI][EMIM].

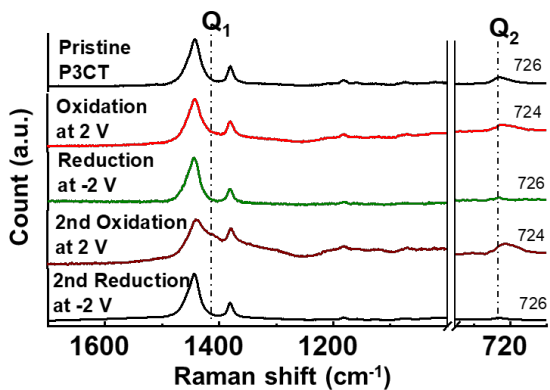


Figure 49. Raman spectra of P3CT films after doping and dedoping upon cyclic voltammetric cycles.

Interestingly, the characteristic absorption peaks of the EMIM cation along with those of the TFSI anion were confirmed in the spectra of the P3CT films upon redox reaction (**Figure 46a**). This implies that both EMIM and TFSI ions penetrated the P3CT under the oxidation process and that a certain amount of both ions were left even after the reduction process. Especially, the two split TFSI peaks in the FT-IR spectra of the reduced P3CT film (red line in **Figure 46b**) implies the existed transoid structure of TFSI anions, which is efficient for ionic interaction. Due to almost no existence of polarons in the reduced P3CT films, I supposed the new interaction between the protons dissociated from carboxylic acid and the remaining TFSI anions (**Figure 46**). Furthermore, the absorption band at 1575 cm^{-1} attributed to stretching of $\text{CH}_2\text{N}/\text{CH}_3\text{N}$ in EMIM cation shifted to 1568 cm^{-1} in the spectrum of the reduced P3CT film, indicating that the positively charged imidazole ring was stabilized by the anion.^[36] In other words, even though the TFSI and EMIM ions penetrated into the P3CT films during redox process remained in the films, the charged both ions could be screened by counter ions of carboxylate anions of the P3CT and protons. Therefore, a reversible change between doped and dedoped P3CT was achieved, which consequently induces the stable cyclic characteristics of the P3CT-neurofiber device. The chemical interactions between ions and P3CT molecules and the charge distribution in the OECT device based on P3CT depending on the redox conditions are presented in **Figure 50**.

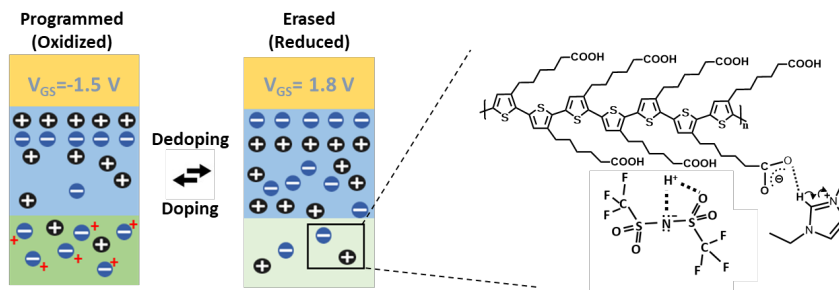


Figure 50. Illustration of the interaction between P3CT and [TFSI][EMIM] under electrochemical doping and dedoping process.

Different redox reaction of P3HT and P3CT during doping and dedoping process can influence crystalline structure and morphology of the films. Atomic force microscopy (AFM) images of P3HT films was shown in **Figure 51**. The penetration of the TFSI ions in doped P3HT film induced the swelled nanofibril structure of the pristine P3HT film. Such swelled P3HT morphology, however, did not return to the initial nanofiber structure in dedoped P3HT film. This result means that the physical penetration and ejection of TFSI anions under doping and dedoping process with electrochemical reactions leading to reorganization of the P3HT chains. The change in crystalline structure of P3HT films upon electrochemical redox reactions was investigated by two-dimensional grazing

incidence X-ray diffraction (2D-GIXD) (**Figure 52**). The out-of-plane (200) and in-plane (010) diffraction plot of P3HT films extracted from the 2D-GIXD patterns were shown in **Figure 53**. Its crystallinity significantly decreased after oxidation of the P3HT film. The distance of lamellar stacking (a-axis) in P3HT increased from 1.61 to 1.88 nm due to ions penetrated into the P3HT film; whereas the distance of π - π stacking (b-axis) decreased. These results consist with report by Guardado et al., who demonstrated that ions penetrated into P3HT leading to reduced crystallinity with increase in lamellar stacking spacing and decrease in π - π stacking induced by lattice strain.^[37] They found that the deformation and crystallinity of the molecular stacking structure were not completely returned to the initial state of the pristine P3HT film ever after the reduction process. During applying the oxidative potential to the interface between P3HT and [EMIM][TFSI], it is shown that TFSI ions penetrated into the alkyl side chains stacking and the nanofibril structure composed of interconnected crystallites changed to the nanogranule structure (**Figure 54**). This assists the results of the electrochemical study indicating that the doped state of P3HT was not returned to its initial state under continuous redox cycles due to remaining TFSI anions in the film.

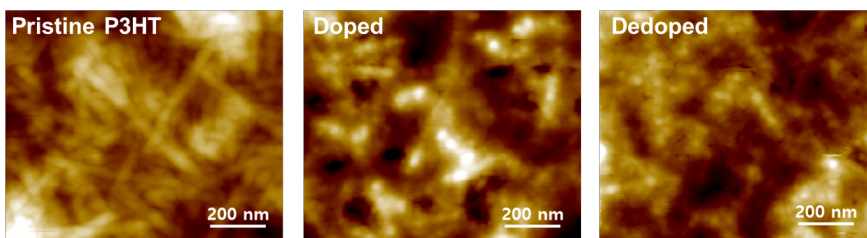


Figure 51. AFM topography images of pristine P3HT, doped P3HT and dedoped P3HT.

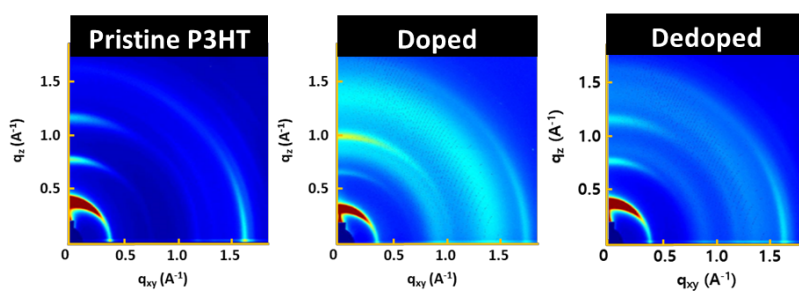


Figure 52. 2D grazing-incidence X-ray diffraction (GIXD) profiles of pristine, doped and dedoped P3HT films.

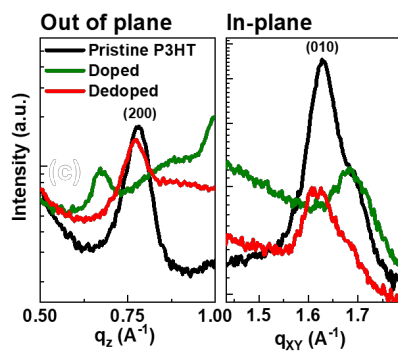


Figure 53. Out-of-plane and in-plane grazing incidence X-ray diffraction (GIXD) plots of P3HT upon electrochemical doping and dedoping process.

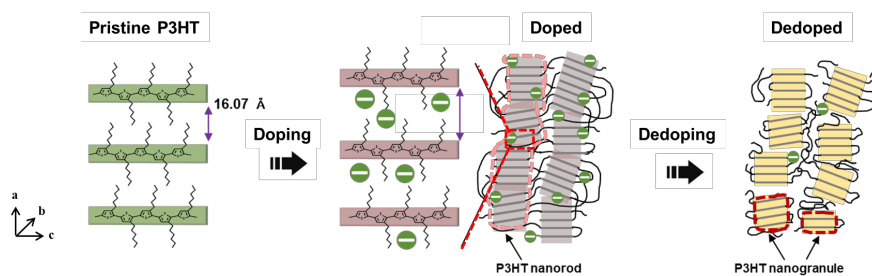


Figure 54 . Schematics presenting the change of the polymer structure under doping/dedoping process by penetration of ions in P3HT.

In contrast, a different behavior was confirmed for the morphology and crystalline structure under the redox reaction in the case of P3CT films. Under the

electrochemically doping and dedoping process of P3CT in the [EMIM][TFSI], the nanogranular structures of pristine P3CT swelled and then recovered to the initial morphology (**Figure 55**). Compared to the results of the P3HT films, it is indicated that P3CT maintains its initial structure under penetration/removal of ions. **Figure 56** shows the out-of-plane and in-plane GIXD plots for the P3CT films depending on the electrochemical redox reaction. After the oxidation reaction, the decrease of the crystallinity and the increase of amorphous halo peak in P3CT were noticeable in the out-of-plane lamellar stacking with the increased interlamellar distance (**Figure 57**).^[38] These results imply that the penetration of ions disrupted the side-chain stacking. Additionally, the transformation from carboxylic acid groups to carboxylate groups in the side chains of P3CT during doping induces conformational transitions such as the rotation of the polymer backbone due to electrostatic repulsion between negatively charged carboxylate in polymer chains (**Figure 58**).^[39] In fact, it is supported by the Raman analysis of P3CT films which showed the decreased planarity of polythiophene backbone due to tilting or rotation of the thiophene moieties (**Figure 59**).^[40, 41] In this condition, the almost collapsed π - π stacking of the P3CT with the in-plane was observed and it was not returned under the reduction process. The rotated or tilted structure of thiophene backbone might provide sufficient free volume for the ions to penetrate and retract under the redox reaction without substantial morphological changes in the P3CT. In

conclusion, it can be suggested that the reversible ionic movement in the P3CT film with the balanced charge between polymer and ions leads to the highly durable and stable characteristics during repeated redox cycles.

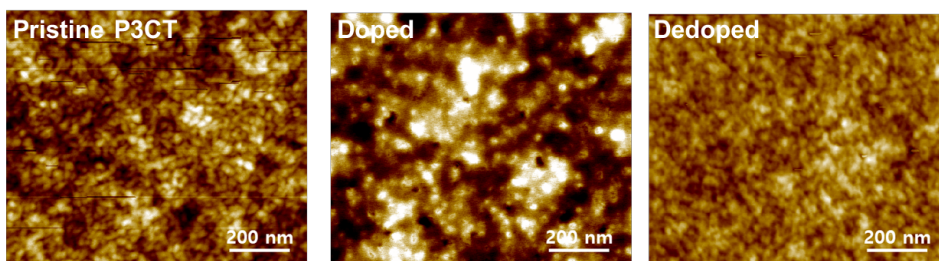


Figure 55. AFM topography images for pristine P3CT, doped P3CT, and dedoped P3CT films.

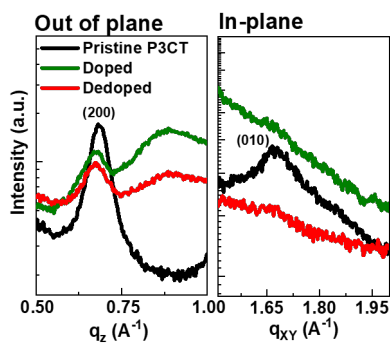


Figure 56. Out-of-plane and in-plane grazing incidence X-ray diffraction (GIXD) plots of P3CT upon electrochemical doping and dedoping process.

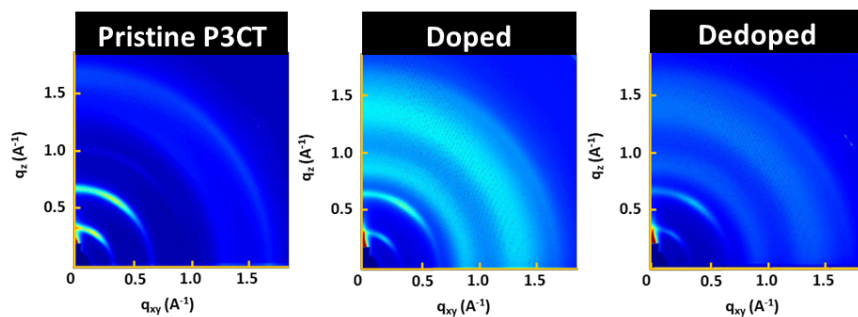


Figure 57. 2D grazing-incidence X-ray diffraction (GIXD) profiles of pristine, doped and dedoped P3CT films.

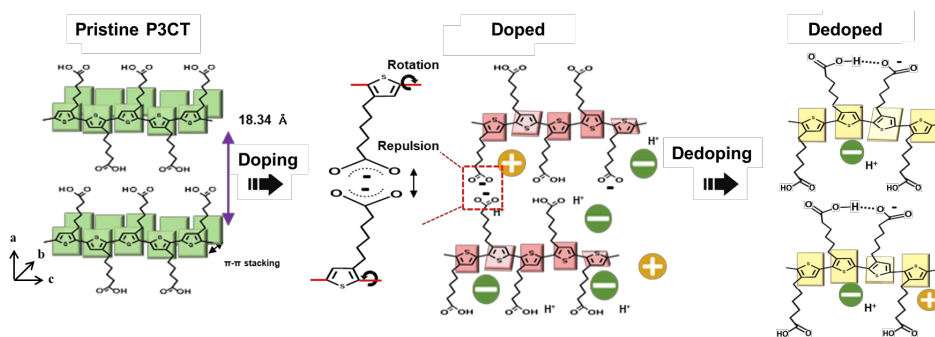


Figure 58. Schematics presenting the change of the polymer structure under doping/dedoping process by penetration of ions in P3CT.

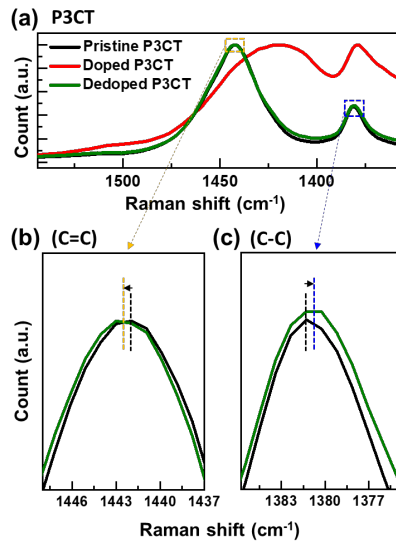


Figure 59. Raman spectra analyzed for (a) pristine P3CT (black line), doped P3CT (red line) and dedoped P3CT (green line) films. Compared to the backbone planarity of P3CT and dedoped P3CT, (b) the (C=C) peak shifted higher and (c) the (C-C) peak shifted lower after dedoping process.

Since each gate can control the reversible doping and dedoping of active channel, I examined the neuromorphic behavior of the P3CT-neurofiber device to demonstrate a unit neural network consist of multiple presynaptic neurons connected to single postsynaptic neurons through synapses. In respect of the functionality, the presynaptic spikes or pulses pass through the gates of the neurofiber as if it occurs at axon terminal of biological neural network. Each gate

discretely defines the local channel area and changes the conductance by doping and dedoping, which contributes to the source-drain current acting as an artificial synapse. The response currents to the spikes coming through each gate is integrated in a leaky way representing the signal from postsynaptic neuron (**Figure 60**). To implement as an artificial neuron device with neural response transmission in an SNN, response spikes of the drain current of P3CT-neurofiber denoting the postsynaptic neuron's membrane potential should emulate the expected neural behavior described by the leaky integrate-and-fire (LIF) model.^[43] The frequency of incoming spikes decides the magnitude of the response spikes in rate coding of neurons. The drain current as response spikes is integrated depending on the time interval (Δt) between the input pulses into the P3CT-neurofiber, representing LIF behavior, as shown in **Figure 61**. Different frequencies of the input spikes induce the distinguishable behaviors in integrating drain current to reach the threshold (blue line). The P3HT-neurofiber also exhibit the same integration behavior in response to the input spike frequency (**Figure 62**). The minimum energy consumption measured in the P3CT-neurofiber device is calculated approximately as 2 pJ/spike (**Figure 63**). This energy consumption is comparable to the previous reported energy consumption of neuromorphic devices, with an average of 2.68 pJ/spike.^[42]

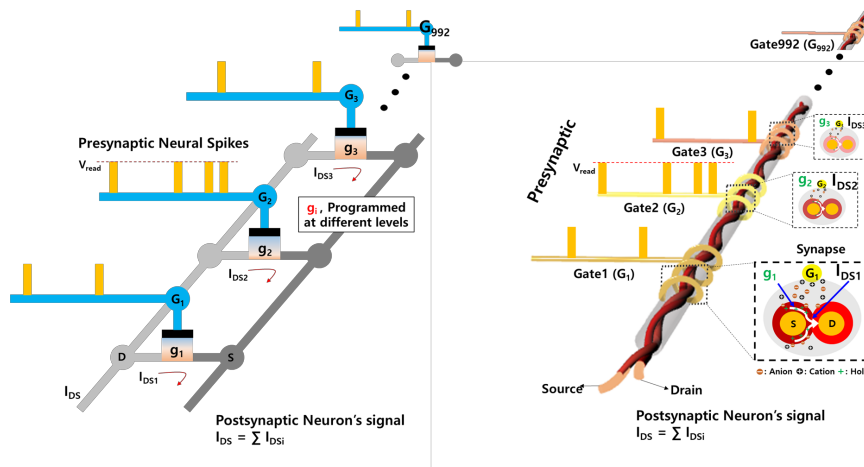


Figure 60. Illustrated diagrams of single class neural network on the basis of Tempotron learning method and operation of neurofiber. (g_i : conductance of each channel)

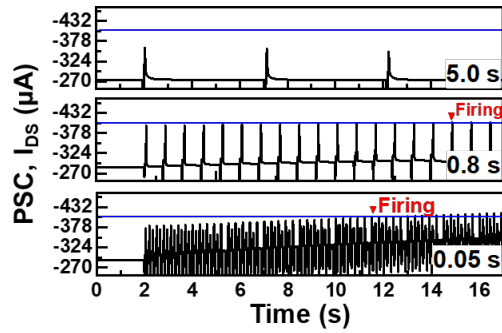


Figure 61. Postsynaptic current (PSC) of a P3CT-neurofiber according to function of the time difference (Δt) between spikes ($V_{GS} = -0.7$ V, 100 ms) as a presynaptic stimulus.

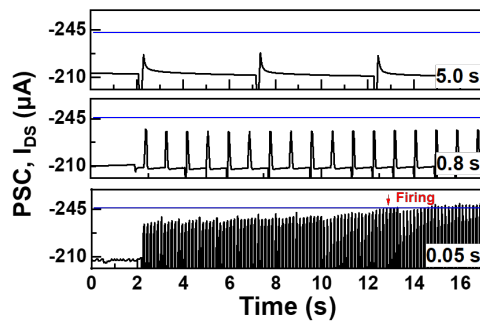


Figure 62 . Postsynaptic current (PSC) of a P3HT-neurofiber depending on function of the time difference (Δt) between spikes ($V_{GS} = -0.7$ V, 100 ms).

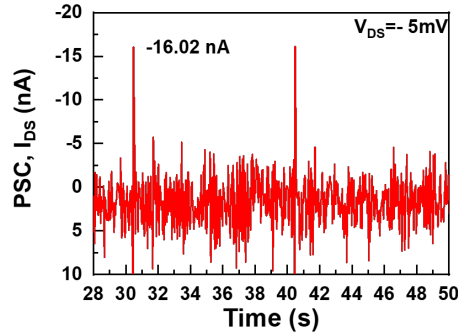


Figure 63. Postsynaptic current induced by applied voltage pulses ($V_{GS} = -5$ mV, 50 ms).

The synaptic weights need to be appropriately updated according to the potentiation and depression cases during the learning process. In the P3HT- and P3CT-neurofibers, various program states function as synaptic weights of the artificial synapses between the gate and the source–drain corresponding to presynaptic and postsynaptic neuron, respectively. **Figure 64** show the typical potentiation and depression behaviors of the neurofiber device and each drain-current level of the potentiation and the depression as the synaptic weight. Specifically, the programmed or erased states of the P3HT-neurofiber (red dots) show a relatively large deviation compared to those of the P3CT-neurofiber (black dots). Thus, the P3HT-neurofiber induces an inaccurate learning process due to the inaccurate synaptic weight responding to the spike as well as the overlap between

the synaptic weights. Compared to P3HT-neurofiber, P3CT-neurofibers clearly shows reliable program-state and maintains the state levels during 46 repeated potentiation and depression processes. In contrast, the state levels of the P3HT-neurofiber consistently increase under the cycle tests and is different from the initial program state level. This implies that the P3CT-neurofiber has remarkable reliability to implement the neuromorphic learning process by repetitively modulating the programmed or erased states as an artificial synaptic device.

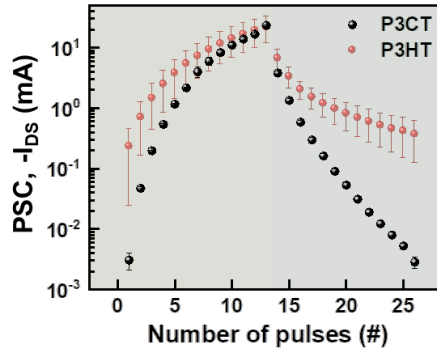


Figure 64. Long-term potentiation at $V_{DS} = -0.2$ V and $V_{PGM} = -1.5$ V with $T_{PGM} = 1$ s and long-term depression at $V_{DS} = -0.2$ V and $V_{ER} = 1.8$ V with $T_{ER} = 0.5$ s of the P3CT- and P3HT-neurofibers.

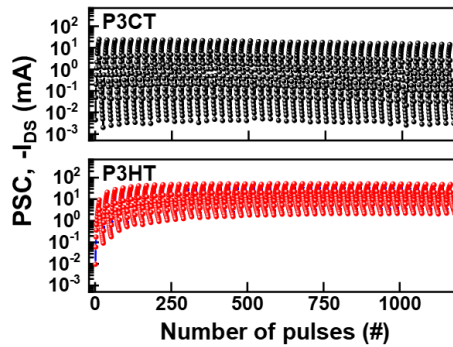


Figure 65. Cycle test of P3CT- and P3HT-neurofiber for recording long-term potentiation and long-term depression over 45 cycles.

Additionally, each synaptic weight of the unit neural network demonstrated by the multigate P3CT-neurofiber should be controlled individually by the each gate to process the incoming spatiotemporal spike patterns from the presynaptic neurons. To investigate the independent synaptic behavior of the multigate P3CT-neurofiber, I confirmed that each gate defines the reproducible and discrete channel conductance (**Figure 66**). The synaptic weight levels labeled with a number were controlled and reproduced back and forth by one designated gate at a time when the other synaptic weights were previously programmed and fixed at a specific level (gate1 - red, gate2 - green, and gate3 - blue in **Figure 66**). Based on this results, it was found that the synaptic weights of the multigate P3CT-neurofiber could be

controlled and updated independently to a specific state level like as the individual synapses connected to the presynaptic neuron with a specific condition. In detail, the structure of multigate P3CT-neurofiber is capable of realizing a dendritic neural network with the ability to implement behaviors of neuron and synapse. **Figure 67** shows how the multigate structure P3CT-neurofiber distinguishes the spatiotemporal spikes based on the synaptic weights for input signals with the same time interval. The left two subplots in **Figure 67** show that programming the initial or low-level states with gate1 makes it difficult to integrate response spikes to exceed the certain threshold (dashed line). In contrast, increasing the programmed state with gate1 and gate2 decreases the required input pulses for integrating response spikes to reach the same threshold, as shown in the right two subplots in **Figure 67**. These results indicate that integrated response spikes can be classified depending on the programmed state levels controlled by each gate and the spatiotemporal signals from the specific gates.

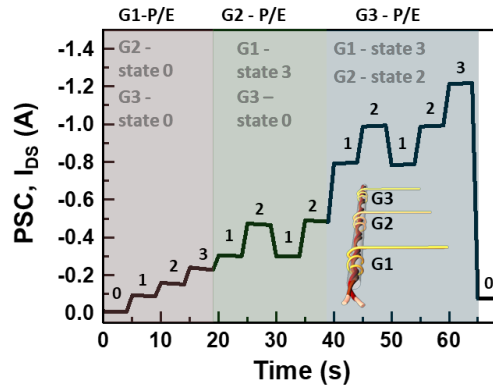


Figure 66. Reproducible and distinct channel conductance of the P3CT-neurofiber defined by each gate under programmed/erased (P/E) pulses ($V_{DS} = -0.2$ V, $V_{PGM} = -1.5$ V, $T_{PGM} = 1$ s, $V_{ER} = 1.8$ V, $T_{ER} = 0.1$ s). Red, green, and blue sections are distinguished by the channel controlled by gate1, gate2, and gate3, respectively; the number of each gate pulse and conductance of the devices are shown in the graph.

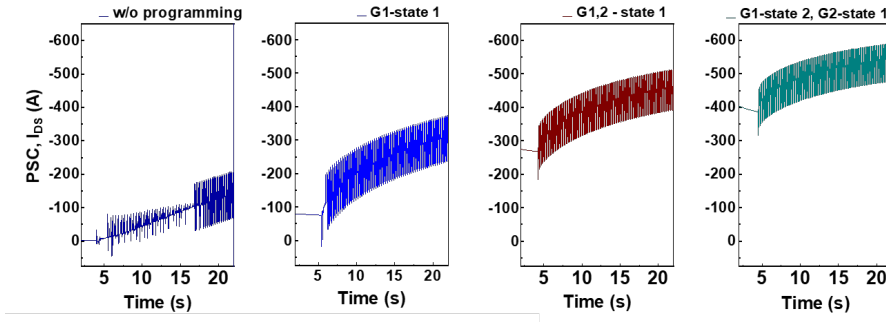


Figure 67. Integration of the pulses during operating device and value comparison for response spikes according to gates and program combinations in the P3CT-neurofiber.

In order to confirm the feasibility of P3CT-neurofiber for realizing practical artificial neural network system, an array composed of 100 distinct synapses with 10 presynaptic connections, each associated with 10 postsynaptic neurons was demonstrated, as shown in **Figure 68**. This array for artificial neural network was simply demonstrated by connecting 10 P3CT-neurofibers and 10 gate-microfibers. The electrical characteristics of the 10 synapses marked by red circle in the 10 by 10 array (**Figure 68**) exhibit uniform memory window with I_{on}/I_{off} current ratio over 10^3 under $V_{GS} = 0$ V and $V_{DS} = -0.2$ V, as shown in **Figure 69**. The performance of 100 neurons is shown in the **Figure 70**, which indicates that the

P3CT-neurofibers can be reproducibly fabricated to form a neural network operating with distinct memory states.

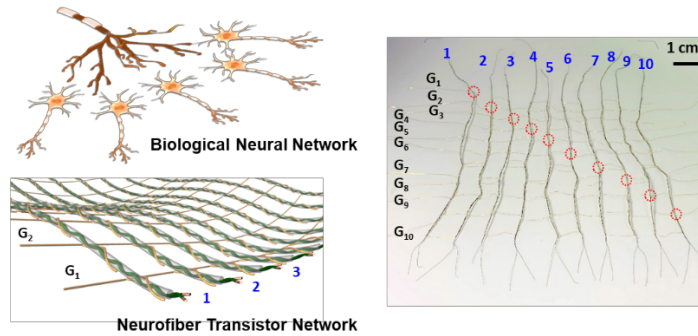


Figure 68. Illustration of biological neural network and artificial neural network demonstrated by array of neurofiber (right) and photography of a 10x10 array composed of P3CT-neurofibers.

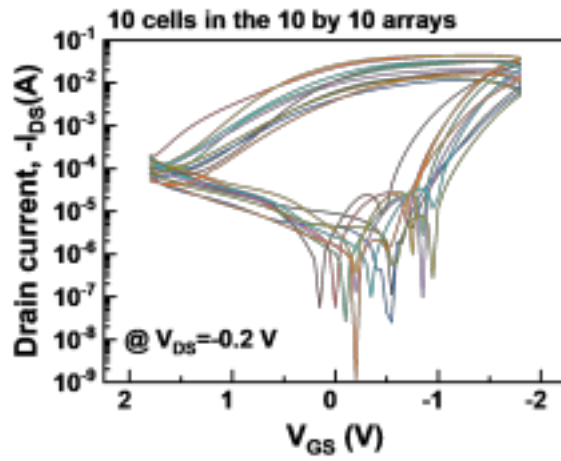


Figure 69. Plotted transfer characteristics for the devices marked with red circle in the 10x10 array.

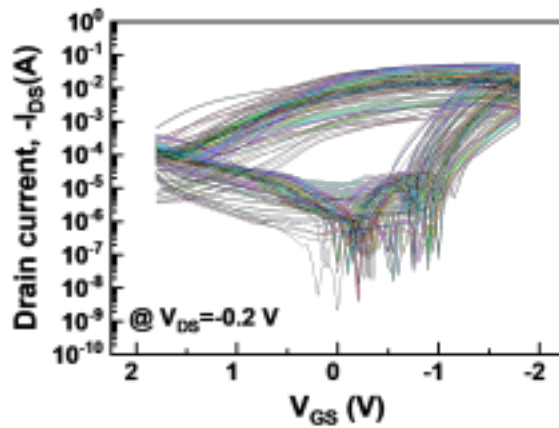


Figure 70. Plotted transfer characteristics for the all devices in the 10x10 array.

Speech recognition based on the neuronal and synaptic characteristics of the P3CT-neurofiber was demonstrated to prove the feasibility of the P3CT-neurofiber as a neuromorphic device with the spatiotemporal SNN learning. As shown in **Figure 60**, the source-drain current (I_{DS}) of the P3CT-neurofiber responds to the input stimulation through each gate and emulates the postsynaptic neuron's membrane potential. The channel area localized by each gate corresponding synapse between the presynaptic and the postsynaptic neurons is regulated by the synaptic weight. Therefore, the spatiotemporal input stimuli with the same voltage induce the different partial I_{DS} for each gate to be integrated in leaky way. Therefore, the response drain current of the P3CT-neurofiber corresponds to the membrane potential in the spatiotemporal SNN learning process. In this work, the response I_{DS} of the P3CT-neurofiber, which are represented as an integration of the product depending on the synaptic weights and the LIF neuron signals, especially simulate the potential of the membrane in the spatiotemporal SNN learning method called as tempotron.^[23, 43] This model straightforwardly emulates the spatiotemporal signal process in biological neural network and its sensitive of synaptic weight to the gate bias stimulation is suitable to implement the SNN learning method. The speech recognition process based on the tempotron model using the neuronal properties of the P3CT-neurofiber is explained in **Figure 71a**. The input data, extracted from the TI-46 database,^[22] comprises isolated audio waveforms of

spoken digits such as zero to nine, pronounced by different females. The waveform data are transformed into spatiotemporal patterns. The converted data with a series of spikes are applied to the gates then passed through the corresponding synaptic weights to 10 P3CT-neurofibers specified in each spoken digit as the output. The response input spike from the gate (presynaptic neuron) is designed with the synaptic weight and the time constants for leaky behavior. During the learning process, the channel regions designated by the gates and acting as the synaptic weights are updated to classify one digit among ten digits depending on the tempotron learning rule. Since then, I_{DS} of P3CT-neurofiber differentiates the input spoken digits by firing or maintaining silent with following the LIF behavior during test process. As a binary classifier, firing in unit neurofiber is comprehended as “target” and remaining silent in the device is interpreted “null” for prediction. For example, in the case of the given digit “nine”, the prediction is correct when the device specified as the nine classifier fires and the other devices attributed to other digits maintain silent. Through the training and testing operation, the results of classification accuracy for ten devices trained for each digit are described as a 2D map in **Figure 71b**; the overall average accuracy after leaning was 88.9%. In **Figure 71c**, the P3CT-neurofiber successfully implements as a neuromorphic device with the saturated accuracy depending on the iterative learning process. Compared to P3CT-neurofiber, however, when the speech recognition in the same

way using neuronal characteristics of the P3HT-neurofiber was performed, classification accuracy cannot be advanced during the iterative training process because the weight value cannot be regulated to the correct value as a result of the programmed/erased state's degradation identified in **Figure 64** and **Figure 65**. In this unstable conductance of neuromorphic device for iterative learning operation, some conductance cannot be stated as the synaptic weights because its conductance is out of the sufficient conductance range determined by the g_{\max} and g_{\min} values. This final results indicate the absence of the available synaptic weight in P3HT-neurofiber for the learning process.

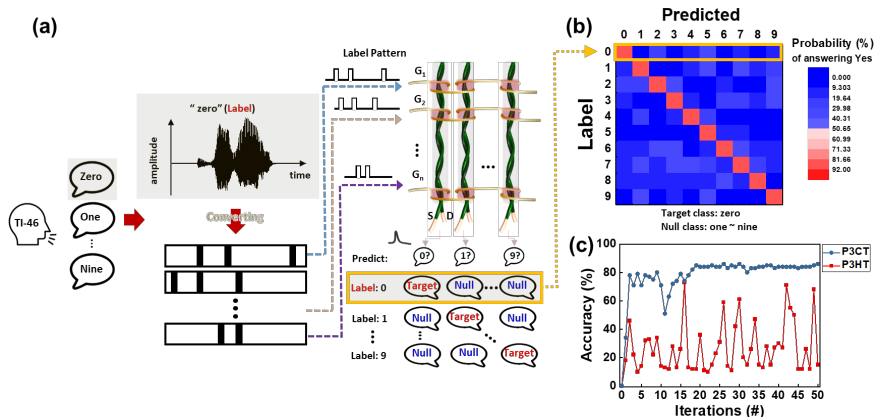


Figure 71. (a) Process of speech recognition by the tempotron using the P3CT-neurofiber. (b) 2D map of the classification test for accuracy of 10 digits. (c)

Comparison of the accuracy in iterative learning for speech recognition between P3HT- and P3CT-neurofibers.

3.4 Summary

In this work, dendritic network implementable fiber-shaped neuromorphic OECTs with improved memory cyclic endurance were demonstrated using the architecture of twisted electrode microfibers coated by carboxylic acid-functionalized polythiophene (P3CT) and an iongel gate insulator. The suggested P3CT-neurofiber OECTs exhibited gate-field-dependent multilevel memory characteristics with good stable cyclic endurance and long-term stability, as well as synaptic plasticity, which can be controlled by the presynaptic gate bias. These characteristics are significantly enhanced compared to those of neuromorphic OECTs with conventional P3HT, which showed a short retention time and unstable cyclability under repeated cycling processes. In this work, fundamental studies on the electrochemical interactions and reactions of the polythiophenes and ions under cyclic operation indicated that the anions penetrated into the P3HT active channel under doping bias and leading to long-term plasticity were not completely removed from the P3HT active layer even after strong dedoping process. This irreversible redox behavior of P3HT caused a continuous increase of the OFF- current and

unstable cyclability. In contrast, the carboxylate anions and protons from the carboxylic acid groups in P3CT existed after the de-doping process, which efficiently stabilized the residual anions and cations that penetrated into the P3CT film under the doping process. This balanced charge facilitates the reversible redox interactions and reactions in the P3CT channel, leading to stable cyclic characteristics of the device. P3CT-neurofiber transistor showed LIF behavior which is suitable for an SNN and maintained stable levels during repeating potentiation and depression processes. The synaptic weight of multigate P3CT-neurofiber with a dendritic network was independently modulated to a specific state level by using simple synapse connection with the multigate as presynaptic neurons. At the end, for iterative learning simulation with P3CT-neurofiber transistors as a neuromorphic device, the high classification accuracy in speech recognition was successfully demonstrated. This work shows that the cyclic endurance of the neuromorphic devices is important for application to iterative learning and that reversible electrochemical reactions or interaction between the organic semiconductor and ionic species are a critical factor for enhancing the cyclic characteristics of the device.

3.5 References

- [1] Y. van De Burgt, A. Melianas, S. T. Keene, G. Malliaras, A. Salleo, *Nat. Electron.* 2018, 1, 386.
- [2] L. Abbott, W. G. Regehr, *Nature* 2004, 431, 796.
- [3] V. M. Ho, J.-A. Lee, K. C. Martin, *Science* 2011, 334, 623.
- [4] W. Xu, S.-Y. Min, H. Hwang, T.-W. Lee, *Sci. Adv.* 2016, 2, e1501326.
- [5] F. Yu, L. Q. Zhu, *pss (RRL)* 2019, 13.
- [6] Y. van de Burgt, E. Lubberman, E. J. Fuller, S. T. Keene, G. C. Faria, S. Agarwal, M. J. Marinella, A. A. Talin, A. Salleo, *Nat. Mater.* 2017, 16, 414.
- [7] J. Rivnay, S. Inal, A. Salleo, R. M. Owens, M. Berggren, G. G. Malliaras, *Nat. Rev. Mater.* 2018, 3, 1.
- [8] C. Qian, J. Sun, L.-a. Kong, G. Gou, J. Yang, J. He, Y. Gao, Q. Wan, *ACS Appl. Mater. Interfaces* 2016, 8, 26169.
- [9] Y. Fu, L.-a. Kong, Y. Chen, J. Wang, C. Qian, Y. Yuan, J. Sun, Y. Gao, Q. Wan, *ACS Appl. Mater. Interfaces* 2018, 10, 26443.
- [10] H. Han, Z. Xu, K. Guo, Y. Ni, M. Ma, H. Yu, H. Wei, J. Gong, S. Zhang, W. Xu, *Adv. Intell. Syst.* 2020, 2, 1900176.
- [11] D. Liu, Q. Shi, S. Dai, J. Huang, *Small* 2020, 16, 1907472.
- [12] D.-G. Seo, Y. Lee, G.-T. Go, M. Pei, S. Jung, Y. H. Jeong, W. Lee, H.-L. Park, S.-W. Kim, H. Yang, *Nano Energy* 2019, 65, 104035.
- [13] T. Berzina, A. Smerieri, M. Bernabò, A. Pucci, G. Ruggeri, V. Erokhin, M. Fontana, *Int. J. Appl. Phys.* 2009, 105, 124515.
- [14] P. Gkoupidenis, N. Schaefer, X. Strakosas, J. A. Fairfield, G. G. Malliaras, *Appl. Phys. Lett.* 2015, 107, 263302.
- [15] P. Gkoupidenis, N. Schaefer, B. Garlan, G. G. Malliaras, *Adv. Mater.* 2015, 27, 7176.

- [16] Y. Choi, S. Oh, C. Qian, J.-H. Park, J. H. Cho, *Nat. Commun* 2020, 11, 1.
- [17] B. Ruf, M. Schmitt, "Hebbian learning in networks of spiking neurons using temporal coding", presented at IWANN, 1997.
- [18] W. Zeng, L. Shu, Q. Li, S. Chen, F. Wang, X. M. Tao, *Adv. Mater.* 2014, 26, 5310.
- [19] S. Kwon, Y. H. Hwang, M. Nam, H. Chae, H. S. Lee, Y. Jeon, S. Lee, C. Y. Kim, S. Choi, E. G. Jeong, *Adv. Mater.* 2020, 32, 1903488.
- [20] V. Sanchez, C. J. Walsh, R. J. Wood, *Adv. Funct. Mater.* 2021, 31, 2008278.
- [21] S. Ham, M. Kang, S. Jang, J. Jang, S. Choi, T.-W. Kim, G. Wang, *Sci. Adv.* 2020, 6, eaba1178.
- [22] M. Liberman, R. Amsler, K. Church, E. Fox, C. Hafner, J. Klavans, M. Marcus, B. Mercer, J. Pedersen, P. Roossin, D. Walker, S. Warwick, A. Zampolli, Linguistic Data Consortium, Philadelphia 1991.
- [23] R. Gütig, H. Sompolinsky, *PLoS Biol* 2009, 7, e1000141.
- [24] S. J. Kim, H. Kim, J. Ahn, D. K. Hwang, H. Ju, M. C. Park, H. Yang, S. H. Kim, H. W. Jang, J. A. Lim, *Adv. Mater.* 2019, 31, 1900564.
- [25] Y. Na, F. S. Kim, *Mater. Chem. Phys.* 2019, 31, 4759.
- [26] P. Bonhote, A.-P. Dias, N. Papageorgiou, K. Kalyanasundaram, M. Grätzel, *Inorg. Chem.* 1996, 35, 1168.
- [27] G. Snook, A. Best, A. Pandolfo, A. Hollenkamp, *Electrochem. commun.* 2006, 8, 1405.
- [28] X. Chen, O. Inganäs, *J. Phys. Chem.* 1996, 100, 15202.
- [29] W. Wang, C. Chen, C. Tollan, F. Yang, Y. Qin, M. Knez, *J. Mater. Chem. C* 2017, 5, 2686.
- [30] K. T. Munson, J. Vergara, L. Yu, T. D. Vaden, *J. Phys. Chem. B* 2015, 119, 6304.
- [31] T. Liu, Y. Danten, J. Grondin, R. Vilar, *J. Raman Spectrosc.* 2016, 47, 449.

- [32] J. K. Denton, P. J. Kelleher, M. A. Johnson, M. D. Baer, S. M. Kathmann, C. J. Mundy, B. A. W. Rudd, H. C. Allen, T. H. Choi, K. D. Jordan, *PNAS* 2019, 116, 14874.
- [33] B. C. Smith, 2018.
- [34] X. Zhang, L. Chen, L. Yuan, R. Liu, D. Li, X. Liu, G. Ge, *Langmuir* 2018, 35, 5770.
- [35] Y. Li, Y. Song, X. Zhang, X. Wu, F. Wang, Z. Wang, *Macromol. Chem. Phys.* 2015, 216, 113.
- [36] A. M. Moschovi, V. Dracopoulos, *J. Mol. Liq.* 2015, 210, 189.
- [37] J. O. Guardado, A. Salleo, *Adv. Funct. Mater.* 2017, 27, 1701791.
- [38] L. Q. Flagg, C. G. Bischak, J. W. Onorato, R. B. Rashid, C. K. Luscombe, D. S. Ginger, *J. Am. Chem. Soc.* 2019, 141, 4345.
- [39] B. Kim, L. Chen, J. Gong, Y. Osada, *Macromolecules* 1999, 32, 3964.
- [40] B. Sainbileg, Y.-B. Lan, J.-K. Wang, M. Hayashi, *J. Phys. Chem. C* 2018, 122, 4224.
- [41] A. Savva, C. Cendra, A. Giugni, B. Torre, J. Surgailis, D. Ohayon, A. Giovannitti, I. McCulloch, E. Di Fabrizio, A. Salleo, *Mater. Chem. Phys.* 2019, 31, 927.
- [42] G. Indiveri, Y. Sandamirskaya, *IEEE Signal Process. Mag.* 2019, 36, 16.
- [43] R. Gütig, H. Sompolinsky, *Nat. Neurosci.* 2006, 9, 420.
- [44] S. J. Kim, J.-S. Jeong, H. W. Jang, H. Yi, H. Yang, H. Ju, J. A. Lim, *Adv. Mater.* 2021, <https://doi.org/10.1002/adma.202100475>.

Chapter 4

Fibrous TVS Diode for Antistatic E-textile

4.1 Introduction

In general, textiles have been developed to protect and warm human's body from external condition. With the development of wearable electronic device and portable computational systems, textiles as a promising platform to wear daily have been recently emerged into electronic device (i.e. electronic textile (e-textile)) with typical characteristics of fabrics such as flexibility, deformation and light weight. [1] According to requirement of e-textiles, fibrous electronic devices including energy storage^[2-4], sensors^[5,6], light-emitting diode^[7,8] and transistors^[9-12] have been demonstrated with advantages of easily integrating various devices into textile by weaving or knitting methods, stretchability and deformability by curvature of human's body. In order to realize practical and commercial e-textile, several critical challenges such as wash-resistance, passivation layer, low electrical performance and connection or integration of fibrous devices in textiles have been gradually resolved. From a view point of facilitating e-textile, the protection from static electricity, which induces serious damage to electronics and is bound to generated in textiles, should be considered due to low operating voltage of e-textiles (< 2 V). [12, 13] However, there is no attempt to prevent e-textile from static electricity with high voltage (from 10 V to 10 kV).

In order to protect electronic devices from permanent device damages by static electricity, transient voltage suppressor diode (TVS diode), which is able to limit and clamp voltage spike, has been used with capabilities to control operating current and voltage of TVS diode. [14] When the voltage is applied to TVS diode with over the threshold voltage (V_{th}) of the TVS diode, the device becomes conductive and current ground. The electrical properties of TVS diode are defined by doping concentration, resistivity of substrate, thickness of semiconductor and junction area. However, due to rigid property of inorganic materials and limited application to high-voltage operational device, conventional TVS diodes were limited to be utilized into fibrous diode to be integrated in e-textile.

Compared to inorganic TVS diodes, organic diodes have attractive advantages with flexibility and rectifying current under low voltage (~ 5 V). In previous research, for the unidirectional current (i.e rectification) in the organic diodes, Olivier J. Cayre, et al. suggested "electrolyte diode", which is composed of connected positively and negatively charged polyelectrolytes with each containing counter ions.[15] At forward voltage, the unidirectional current was induced by movement of counter ions crossing the interface to oppositely charged electrodes. In contrast, in the backward voltage, the reverse behavior of counter ions form depletion region, which limits conducting current[ref]. The device showed the property of rectification under low voltage (~ 5 V), however, the threshold voltage

of diode cannot be controlled. In addition, it exhibited around value of 15 in rectification ratio due to a low ionic conductivity in polyelectrolytes under AC voltage. Thus, the limitation and sophisticated fabrication of the electrolyte diode are not suitable to be used for protecting e-textiles that require a various critical voltage and fast response. P. Denisevich, et al, proved a new principle for unidirectional current flow with the bilayer of redox polymer in electrolyte solution, which have redox-site in polymers.^[16] However, they only found rectifying characteristics with changing combination of redox substance without considering characteristics of polymeric semiconductor even though enabled redox reaction have been confirmed between polymeric semiconductor and mobile ionic species. In our knowledge, electrochemical reaction based on oxidation/reduction is usually used to organic transistor, electrochromic, sensors and neuromorphic device and still needed to be studied on the behavior of polymer and ion species.

In this work, I proposed fibrous TVS diode with electrochemical rectification and controllable threshold voltage with redox potential of conjugate polymer as a semiconductor for an alternative to realize high rectification and fast response under AC bias. In addition, solid fibrous diode based on metal-ion-gel-semiconductor was operated in electrostatic discharge (ESD) circuit on e-textile incorporating fibrous TVS diode and transistors with low-operational voltage (~2V). I also investigated the redox reaction between polymers and ions that

determines the threshold voltage of diodes, as well as the penetration of ions leading to break voltage.

4.2 Experimental Method

Materials: Gold microfibers with 0.1 mm diameter (purity: 99.95%) were purchased from Alfa Aesar. Poly(vinylidene fluoride-co-hexafluoropropylene) (P(VDF-HFP), $M_n=130 \text{ kgmol}^{-1}$ and $M_w=400 \text{ kgmol}^{-1}$), 1-ethyl-3-methylimidazolium bis(trifluoromethylsulfonyl)amide ([EMIM][TFSA]), dopamine hydrochloride, chlorobenzene, dimethylformamide and methanesulfonic acid were purchased from Sigma-Aldrich. Poly(3-hexylthiophen-2,5-diyl) (P3HT) (91–94% regioregularity, M_w 50–70 kgmol^{-1} , 4002-EE), Poly[3-(6-carboxyhexylthiophene-2,5-diyl) (P3CT) (regioregular, M_w 50–70 kgmol^{-1} , 4033) and Poly(benzimidazobenzophenanthroline) (BBL) were purchased from Rieke Metals.

Device fabrication: P3HT, P3CT and BBL solution were prepared by dissolving P3HT in chlorobenzene, P3CT in dimethylformamide and BBL in methanesulfonic acid with a concentration of 80 mg/ml and this solution was called P3HT, P3CT and BBL solution, respectively. Before coating of the P3HT, P3CT and BBL solution, Au microfibers were immersed in an aqueous tris-HCl buffer solution (pH=8.5) mixed with dopamine (2 mg of dopamine per ml of 10 mM tris-HCl) for

1 h and then rinsed with deionized water. The treated Au microfiber was coated with the P3HT or P3CT or BBL solution using a home-built die-coating system equipped with a T-shaped glass tube as a reservoir and two moving stages. The T-shaped glass tube with a diameter of 3 mm was filled with the P3HT and that of 0.7 mm was filled with semiconductor solution solution by continuously feeding with a syringe. The microfiber was inserted into the tube and drawn at a constant speed in the horizontal direction by the moving stages. The P3HT-, P3CT-, BBL-coated samples were dried in a vacuum oven at 70 °C overnight to remove the residual solvent. In addition, BBL-coated microfiber was washed by methanol. To fabricate a stranded assembly of the P3HT-, P3CT-, BBL-coated electrode microfibers, each end of the microfiber was fixed to slide glass placed parallel. To prepare the ion-gel, P(VDF-HFP) and [EMIM][TFSI] were dissolved in acetone with the polymer, ionic liquid, and solvent mixed in the ratio of 1:4:8 by weight. The prepared mixture was dropped along the semiconductor coated microfibers, which was vertically fixed to the ground. After coating with the ion-gel, the Au microfiber (100 μm) was wound round the ion-gel to form an electrode.

Characterization: Cyclic voltammetry was performed with the P3HT, P3CT and BBL films spin-coated with a thickness of 1 μm with 10 wt% solution on Au substrates. The electrical properties of the fibrous TVS diode was measured using an Agilent 4155B semiconductor device analyzer under ambient conditions. The

ECG was recorded by connecting the ground to the chest and the gate to the wrist. The baseline of the resulting current trace according to time was subtracted to obtain the signal clearly.

4.3 Result and Discussion

Figure 72 shows an illustrates the device structure of the fibrous TVS diode based on electrochemical metal-iongel-semiconductor layer which has the formation of redox layer between iongel and semiconductor by applying redox potential. The current-voltage curve shows that the device composed of metal-iongel-P3HT-metal only shows directional response current (i.e. rectification) based on redox reactions between iongel and P3HT so called rectifying junction (**Figure 73**). Otherwise unidirectional response current results from metal-iongel-metal or metal-P3HT-PVDF-metal. As shown in **Figure 74**, anions in iongel which stabilize oxidized P3HT penetrate into a pristine P3HT initially under the forward voltage. When the bias reaches at oxidative potential, the P3HT is oxidized with transport of electron to metal and the forward current is generated in EMIS diode. On the other hand, there is no charge injection by redox reaction in P3HT under backward direction.

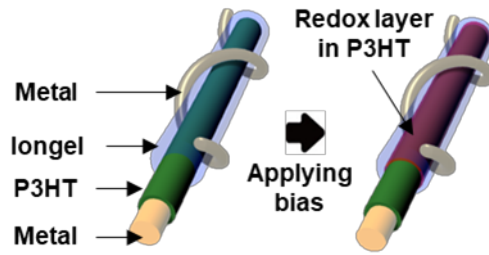


Figure 72. Schematic of fibrous TVS diode based on electrical rectification and composed of metal-iongel-semiconductor.

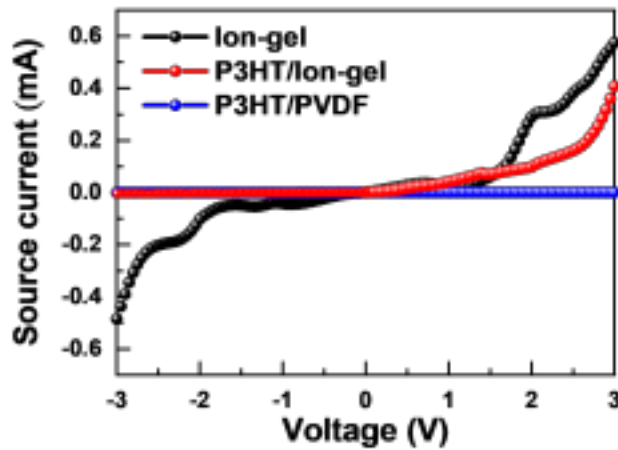


Figure 73. The I-V curves of various components sandwiched between gold electrodes.

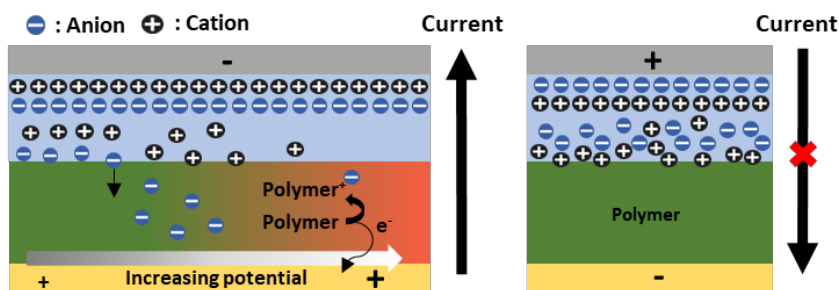


Figure 74. Illustration of the ion migration and redox reaction under forward and backward electric field.

The threshold voltage of fibrous TVS diodes based on P3HT, P3CT and BBL at 0.74 V, 1.59 V and -0.59 V, respectively, are presented in **Figure 75**. To investigate the switching behavior of the devices, the cyclic voltammetry is performed, then I found that the oxidation current of P3HT, P3CT and reduction current of BBL start to continuously increase from 0.88 V, 1.76 V and -0.61, respectively, in cyclic voltammograms (**Figure 76**). Even though the different potential between electronic diode and cyclic voltammetry was observed due to the difference resistance from distance of electrodes (~ 200 μm in diode and 2 cm in cyclic voltammetry measurement) and ionic conductivity of iongel and ionic liquid, it is indicated that the determination of threshold voltage in fibrous TVS diode is based on redox potential. The oxidized states of P3HT and P3CT are characterized by

Raman spectroscopy. The spectrum of the pristine P3HT and P3CT film show two bands at 1446 and 1380 cm^{-1} are attributed to stretching of $\text{C}_\alpha=\text{C}_\beta$ in the thiophene ring and the ring stretching of $\text{C}_\beta-\text{C}_\beta$, respectively. When the P3HT backbone is oxidized with the generation of polaron, the band at 1408 cm^{-1} due to a symmetric stretching of the $\text{C}=\text{C}$ bond ring (Q_1) appears, and the band at 728 cm^{-1} (Q_2) assigned to $\text{C}-\text{S}-\text{C}$ ring deformation shifts lower by structural change. under 1 V bias which is the oxidation conditions of P3HT, increase in the Q_1 and lower shift Q_2 (722 cm^{-1}) polaronic bands were observed, while there was no existence of positive polarons in the P3CT because of insufficient oxidative potential. This result clearly indicates that the electrochemical redox reaction enables switching conductance of the device during applying forward or backward voltage.

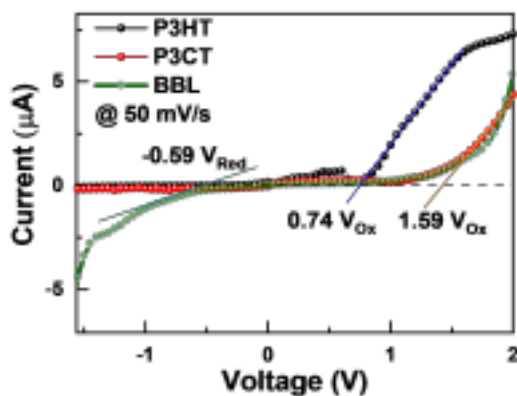


Figure 75. The I-V curves of fibrous TVS diode based on P3HT, P3CT and BBL.

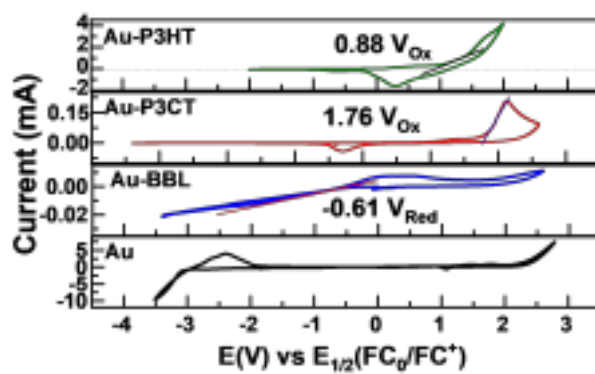


Figure 76. Cyclic voltammograms of P3HT, P3CT and BBL in [TFSI][EMIM] and only [EMIM][TFSI] with Au electrode.

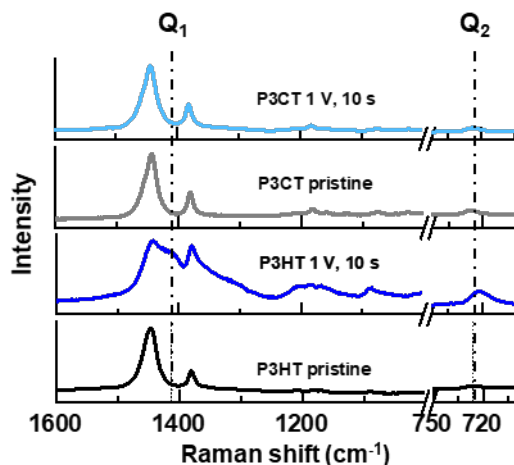


Figure 77. Raman spectra of pristine P3HT and P3CT and after each applying 1V bias for 10 s.

In order to confirm impact of penetrated ions into polymer, which is accompanied with redox reaction under electric field, the penetrated depth of ions was measured by TOF-SIMS (**Figure 78**). In the forward direction, as shown in **Figure 74**, under oxidation potential (-0.3 V), TFSI anion already penetrates into P3HT without generating current. Over oxidation potential (-0.4), the penetration of TFSI shows the similar configuration with anion not contacting the electrode. However, the forward current flows even though the penetrated anion not get to oppositely charged electrode. It was found that the forward current relies on redox reaction not penetration of anion toward the electrode. I also confirmed that the thickness of the semiconductor is related to not conducting current but backward

current over the breakdown voltage (**Figure 79**). As shown in **Figure 80**, the cation is able to penetrate into and the P3HT film over breakdown voltage in I-V curves. The contact of cation crossing the P3HT film from iongel to electrode results backward current, while P3HT with thickness value of 2 μm decrease the current in the backward direction due to the cation is restricted to reach electrode. This result indicates that the thickness of polymer semiconductor acts a key factor to control breakdown voltage.

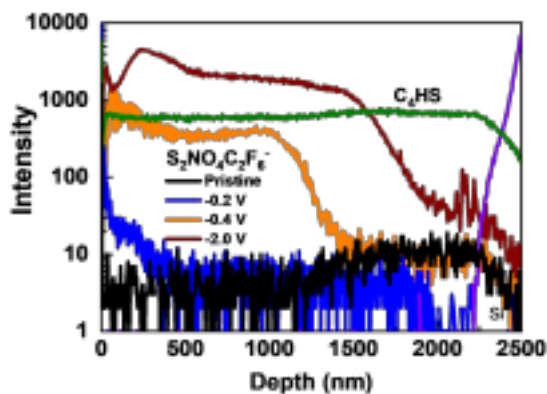


Figure 78. TOF-SIMS depth profile of a pristine P3HT and P3HT films after applying different bias (P3HT/Au/Si).

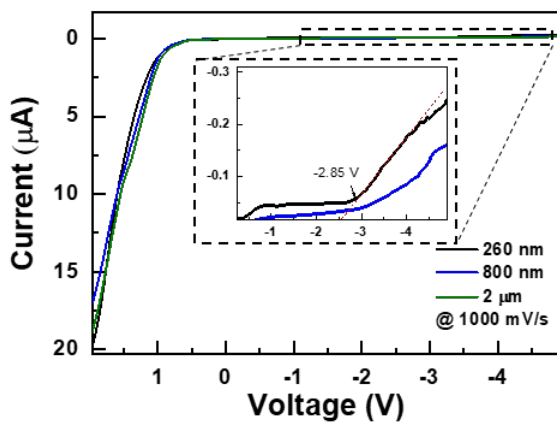


Figure 79. The I-V curves of fibrous TVS diode according to thickness of P3HT.

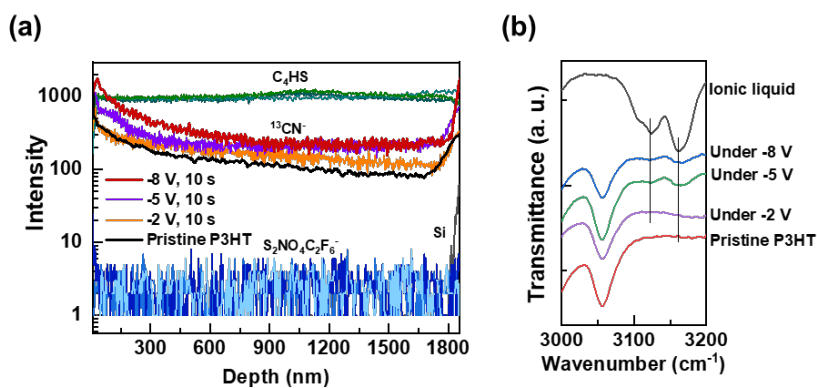


Figure 80. (a) TOF-SIMS depth profile and (b) FT-IR spectra of a P3HT films after applying different voltages (P3HT/Au/Si).

As the concentration of the ionic liquid in iongel was increased from 0.1 to 4.0, the rectification ratio of the device enhances from 0.99 to 231 at ± 1 V and from 1.01 to 1232 at ± 2 V (**Figure 81**). This value is the higher rectification ratio under low-voltage that previous reports[ref]. However, the amount ionic liquid over 4 weight ratio to polymer results increase in backward current with cation penetrating into P3HT and decrease rectification ratio (**Figure 81a, inset**). The EMIS diode were fabricated with different thickness of iongel, however, the device under forward bias shows a similar value of current. (**Figure 82**)

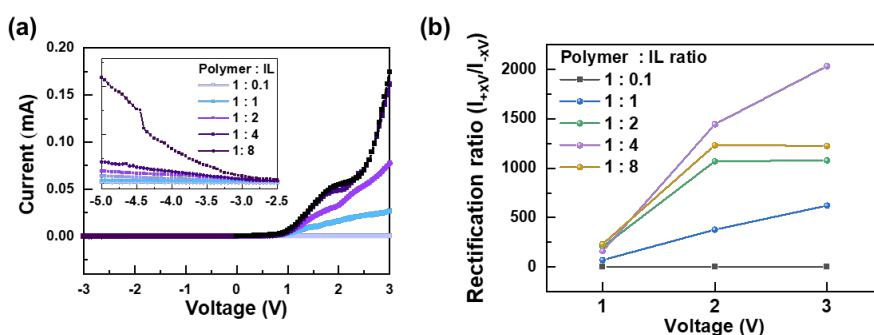


Figure 81. (a) I-V curves of fibrous TVS diode and (b) current rectification ratio with iongel prepared from different ionic liquid ratio at 50 mV/s.

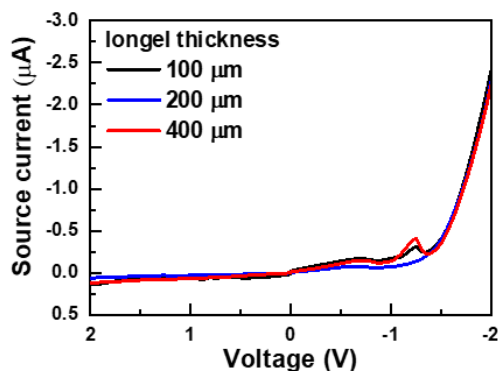


Figure 82. (a) I-V curves of fibrous TVS diode with various thickness of iongel at 50 mV/s.

To investigate the effects of scan rate, cyclic voltammograms of the P3HT with ionic liquid were measured with various sweep rate from 0.05 V/s to 1 V/s as presented in **Figure 83**. The linear dependence on the square root of oxidation potential to scan rate is observed while oxidation potential of P3HT shifted to higher voltage. This is because the mass transport of ions is slower than rate of charge transfer. The slower mass transport of ions limited formation of electrical double layer (EDL) on electrode and penetration of TFSI anion into P3HT, which stabilizes oxidized the polymer leading forward current. As shown in **Figure 84**, due to the limitation of mass transport, in the long-term stability of the EMIS diode,

the time dependence of on-current and off-current increase and decrease by slow penetration of anion and formation of EDL, respectively. Thus the rectification ratio showed increasing from 100. Also the corresponding transient current response of fibrous TVS diode to input pulse for 1s was monitored and showed a decrease rectification value of 34 (**Figure 85**). This phenomenon is also attributed to the mass transport of the ion which induces low rectification ratio.

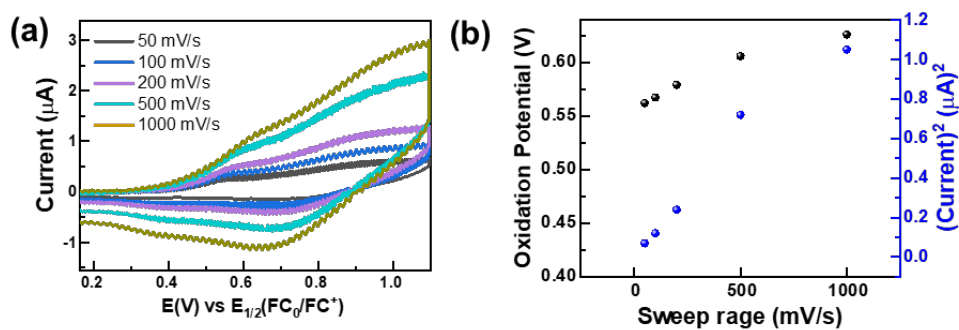


Figure 83. (a) Cyclic voltammograms of P3HT in [TFSI][EMIM] according to different scan rate from 50 mV/s to 1000 mV/s. (b) Plotted curve of oxidation potential and current under cyclic voltammetry.

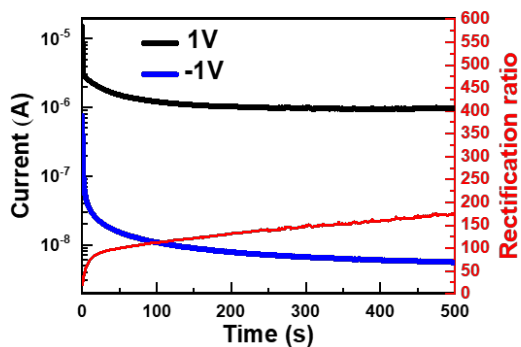


Figure 84. Time dependence plot of current and rectification ratio of fibrous TVS diode under constant voltage bias.

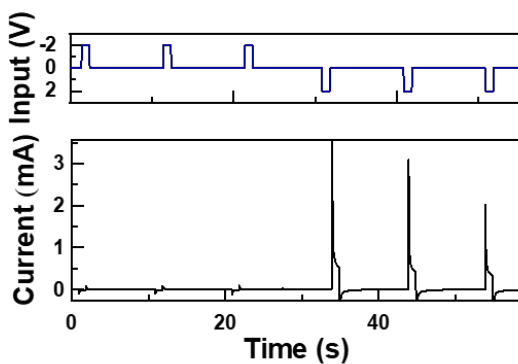


Figure 85. Current response of a fibrous TVS diode under 2 V field for 1 s.

As mentioned in introduction, daily use application of e-textile, the antistatic fibrous electric device is an important issue. The DSA-fiber TFT was tested under

applying ± 10 V pulses, as shown in **Figure 86**, then the device showed a serious degradation and did not exhibit the on/off current ratio. Interestingly, the drain current of DSA-fiber TFT showed decreased 50 % and 67 % under applying $-2 V_{GS}$ and $-5 V_{GS}$, respectively, after integrating fibrous TVS diode. This result indicates that the fibrous TVS diode successfully operates in electrostatic discharge (ESD) circuit in e-textile incorporating fibrous TVS diode and transistors. Real-time monitoring of human body signals is one of the most promising applications of e-textile devices. In addition, to demonstrate the feasibility of antistatic DSA-fiber TFTs to human-body health monitoring, the electrocardiogram (ECG) recording was tested with and without fibrous TVS diode. The ECG signals was clearly monitored with DSA-fiber TFT without fibrous TVS diode. However, after applying ± 10 V pulses, as shown in **Figure 88**, drain current of DSA-fiber did not show characteristic spikes of the heartbeat. This indicated that the DSA-fiber TFT without setting ESD circuit is not practical to adjust e-textile due to the poor antistatic characteristic. To demonstrate more stable operation under high voltage, the DSA-fiber TFTs utilized with fibrous TVS diode was tested after applying ± 10 V pulses and the device showed spikes of the heart beat similar with the device without pulses. This result clearly implies that the antistatic DSA-fiber TFT with fibrous TVS diode has sufficient to apply textile-based wearable healthcare monitoring systems.

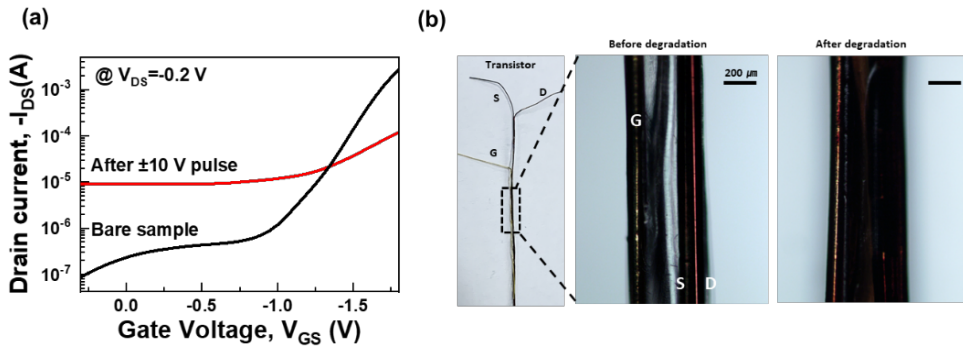


Figure 86. (a) Transfer characteristic of DSA-fiber TFT before (black line) and after (red line) applying ± 10 V pulses. (b) Photography of DSA-fiber TFT before and after degradation.

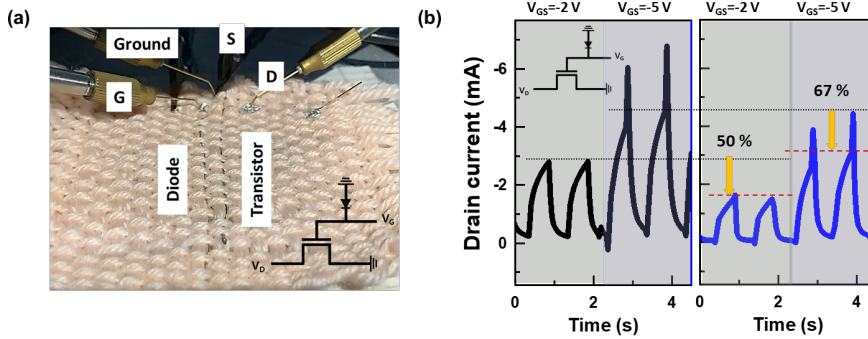


Figure 87. (a) Photography of integrated circuit with fibrous TVS diode and DSA-fiber TFT in the textile. (b) Current response of a DSA fiber TFT without (right) and with (left) TVS diode under -2 V and -5 V field for 0.5 s.

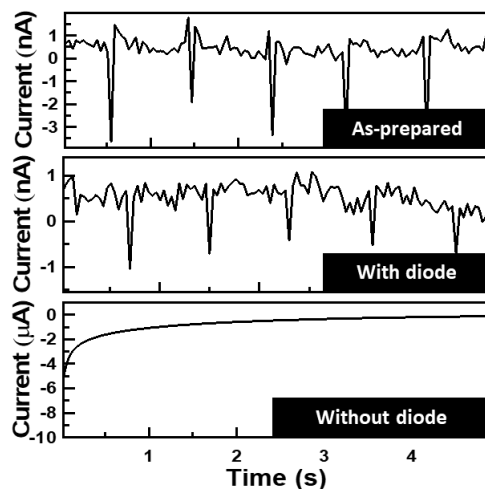


Figure 88. Plot of drain current of DSA-fiber TFT during the measurement of ECG.

4.4 Summary

In this work, fibrous TVS diode was demonstrated to improve durability of previous reported DSA-fiber TFT against electrostatic. The key factor of the designed fibrous TVS diode is controlling threshold voltage of device by adjusting redox potential and thickness of the semiconductor on electrode microfibers. This operation based on redox reaction between polymer and iongel facilitates rectifying current and the flexible fibrous structure with low threshold voltage to depress high

voltage applied to DSA-fiber TFT. In addition, the polymer and ions behaviors under forward and backward bias were successfully introduced. At the forward bias, the redox reaction induces the forward current. In contrast, at the backward bias, the penetration of the counter ion to opposite charged electrode generate the breakdown current. Also it was found that the mass transport of ions limited the rectification ratio under AC pulses because the penetrated ions into polymer induce redox reaction. Finally, as a proof of concept, the DSA-fiber integrated with fibrous TVS diode showed antistatic properties and stable operation even after applying ± 10 V pulses.

4.5 References

- [1] A. K. Yetisen, H. Qu, A. Manbachi, H. Butt, M. R. Dokmeci, J. P. Hinstroza, M. Skorobogatiy, A. Khademhosseini, S. H. Yun, ACS Nano 2016, 10, 3042.
- [2] Y. Huang, H. Hu, Y. Huang, M. Zhu, W. Meng, C. Liu, Z. Pei, C. Hao, Z. Wang, C. Zhi, ACS Nano 2015, 9, 4766.
- [3] S. H. Ha, S. J. Kim, H. Kim, C. W. Lee, K. H. Shin, H. W. Park, S. Kim, Y. Lim, H. Yi, J. A. J. J. o. M. C. A. Lim, J.Mater. Chem. A 2018, 6, 6633.

- [4] Y. Zhang, Y. Zhao, J. Ren, W. Weng, H. Peng, *Adv. Mater.* 2016, 28, 4524.
- [5] K. Cherenack, C. Zysset, T. Kinkeldei, N. Münzenrieder, G. Tröster, *Adv. Mater.* 2010, 22, 5178.
- [6] T. Q. Trung, H. S. Le, T. M. L. Dang, S. Ju, S. Y. Park, N. E. Lee, *Adv. Healthcare mater.* 2018, 1800074.
- [7] Z. Zhang, K. Guo, Y. Li, X. Li, G. Guan, H. Li, Y. Luo, F. Zhao, Q. Zhang, B. Wei, *Nat. Photonics* 2015, 9, 233.
- [8] S. Kwon, H. Kim, S. Choi, E. G. Jeong, D. Kim, S. Lee, H. S. Lee, Y. C. Seo, K. C. Choi, *Nano lett.* 2017, 18, 347.
- [9] H. M. Kim, H. W. Kang, D. K. Hwang, H. S. Lim, B. K. Ju, J. A. Lim, *Adv. Funct. Mater.* 2016, 26, 2706.
- [10] J. S. Heo, T. Kim, S. G. Ban, D. Kim, J. H. Lee, J. S. Jur, M. G. Kim, Y. H. Kim, Y. Hong, S. K. Park, *Adv. Mater.* 2017, 29, 1701822.
- [11] J. B. Lee, V. Subramanian, presented at Electron Devices Meeting, 2003. IEDM'03 Technical Digest. IEEE International 2003.

[12] S. J. Kim, H. Kim, J. Ahn, D. K. Hwang, H. Ju, M. C. Park, H. Yang, S. H. Kim, H. W. Jang, J. A. Lim, *Adv. Mater.* 2019, 31, 1900564.

[13] S. Kwon, Y. H. Hwang, M. Nam, H. Chae, H. S. Lee, Y. Jeon, S. Lee, C. Y. Kim, S. Choi, E. G. Jeong, K. C. Choi, *Adv. Mater.* 2019, 32, 1903488.

[14] D. Bouangeune, Y.-H. Kil, S.-S. Choi, D.-H. Choi, K.-H. Shim, C.-J. Choi, *Mater. Trans.*, 2013, 54, 2125.

[15] O.J. Cayre, S.T. Chang, O.D. Velev, *J. Am. Chem.*, 2007, 35, 10801

[16] P. Denisevich, K. W. Willman, R. W. Murray, *J. Am. Chem.*, 1981, 103, 4727.

Abstract (in Korean)

스마트 전자기기 응용을 위한 섬유 가닥 조립을 기반으로 한 섬유 형태의 유기 전기화학 소자 개발

전자 섬유(E-textiles)는 웨어러블 디바이스를 구현하기 위한 유망한 플랫폼으로서, 휴대성, 세척성, 변형성 그리고 통풍이 가능한 특성의 장점을 이용하기 위해 많은 관심을 받고있다. 그동안 섬유형 전자기기는 유연성, 경량화, 소형화 그리고 다양한 기기와 쉽게 연결 할 수 있다는 점을 앞세워 발전하였다. 1 차원의 원통 구조는 큰 활성 표면을 제공하며 섬유의 조립을 통하여 2D 혹은 3D 의 구조를 만들 수 있다. 지난 10 년간 트랜지스터, 액츄에이터, 에너지 저장장치, 발광소자, 센서 등 다양한 섬유 형태의 장치 개발이 보고되었다. 특히 트랜지스터는 디스플레이, 센서, 메모리, 뉴로모픽 소자에서 전자시스템을 통합할 수 있는 핵심 부품이다. 다만 섬유의 원통 구조는 소스와 드레인 사이에

반도체의 정렬이 필수적인 다층 구조를 가지는 트랜지스터의 실용화와 전기 성능의 향상을 어렵게 한다. 또한 출력 전류에 비례하는 길이 대 너비 비율은 전극의 증착공정으로 인하여 섬유 전극의 반쪽에 제한된다.

이 논문에서는 기존 섬유형 트랜지스터의 한계를 극복하기 위해 전극 마이크로파이버의 이중가닥 조립을 적용한 섬유형 유기박막 트랜지스터 (DSA-fiber TFT)의 새로운 구조를 제안한다. 또한 DSA-fiber TFT의 내구성 및 안정적인 소자 작동을 위하여, 트랜지스터를 작동하는 폴리머와 이온 사이의 산화-환원 반응에 대하여 자세히 분석하였다. 마지막으로 산화-환원 반응을 이용하여 TVS 다이오드에 응용하여 정전기에 대한 내구성을 향상시키는 연구를 진행하였다.

제 1 장에서는 유기 박막 트랜지스터의 기초에 대하여 설명하였다.

제 2 장에서는 섬유형 트랜지스터의 전기 성능을 향상을 통하여 전자 섬유에 실용적으로 사용될 수 있도록 새로운 구조의 DSA-fiber TFT를 설계했습니다. DSA-fiber TFT의 기본 특징은 채널을 형성하기 위해 소스와 드레인으로 (S/D) 사용되는 반도체가 코팅된 전도성 마이크로파이버를 비틀어 조립하는 것이다. 이러한 소자의 구조는 S/D 마이크로파이버의 길이와 반도체 두께를 각각 채널 폭과 길이로 구현 할

수 있어 DSA-섬유 트랜지스터의 채널 치수를 간단하게 제어할 수 있게 한다. 시연된 DSA-fiber TFT 는 $-1.5V$ 의 낮은 전압에서 $-5mA$ 를 이상의 높은 출력 전류와 약 10^5 의 ON/OFF 전류 비율의 뛰어난 전기적 특성을 보였다. 1000 번의 굽힘 사이클과 강한 세제를 섞은 물에 씻은 후에도 기기의 성능이 유지되었다. DSA-fiber TFT 를 이용하여 LED 소자의 밝기와 on/off 를 제어하고, 인체에서 심전도 신호를 증폭함으로써 실용적인 소자로 응용이 가능성이 입증됐다.

제 3 장에서, 향상된 소자의 내구성을 가지고 시공간 반복 학습에 응용될 수 있는 DSA-fiber TFT 를 기반으로 다중 시냅스를 모사가 가능한 유기 뉴로모픽 트랜지스터 (organic-neurofiber)를 제안했다. Organic-neurofiber 의 구조는 생물학적 뉴런의 덴드라이트 네트워크와 다중 시냅스 접합을 구현하기 위해 DSA-fiber TFT 에 여러 게이트를 감아 구현했다. 특히 불규칙한 사이클과 장기 안정성이 떨어지는 기존 고분자 기반 장치에 비해, 탈양성자를 유도할 수 있는 기능성 고분자 기반의 neurofiber 는 규칙적이고 신뢰할 수 있는 사이클과 장기안정성을 보인다. 사이클링 테스트하에서 기능성 폴리머의 채널에서 균형 잡힌 전하가 가역적인 도핑과 디도핑을 반응을 폴리머 채널에서 구현 할 수 있어

안정적이고 신뢰할 수 있는 사이클 내구성을 제공하는 것으로 밝혀졌다. 시냅스 중량을 조절하는 메모리 상태는 안정된 상태를 유지했으며, 기능화 된 폴리머 기반의 소자는 게이트 필드에 의해 각 다중 게이트 아래에서 독립적으로 작동되었다. 마지막으로, 시공간 반복 학습 시뮬레이션으로서의 음성 인식 학습을 neurofiber 를 이용하여 성공하였으며, 약 90%의 상당한 인식 정확도를 보여주었다.

제 4 장에서는 정전기에 대해 전자 섬유를 보호하기 위해 섬유 모양의 전기화학반응을 기반으로 하는 섬유형 TVS 다이오드를 제안했습니다. 섬유형 TVS 다이오드는 전압을 인가하여 이온겔과 반도체 사이의 정류 접합이라고 불리는 산화-환원 층을 형성한다. 전류의 방향은 산화-환원 반응에 기초하므로 섬유형 TVS 다이오드의 임계 전압은 유기 반도체의 낮은 산화 전위(<math><3V</math>)에 의해 조절된다. 다이오드의 낮은 임계값 전압은 저전압에서 작동하는 전자섬유를 정전기로부터 보호하기 위하여 사용될 수 있다. 결과적으로, DSA-fiber TFT 와 섬유형 TVS 다이오드를 섬유에 직조하여 연결한 회로는 다이오드가 없는 것에 대비해 정전기에서 대해 강화된 내구성을 보여준다.

키워드: 섬유형 전자소자, 유기 전기화학 트랜지스터, 전자섬유, 뉴로모픽소자, 폴리티오피린, 산화-환원 메커니즘

학번: 2017-38767

김수진